

THESIS REPORT

Master's Degree

Parameter Identification of Large Spacecraft Systems, Based on the Frequency Characteristics of the Hankel Operator

by D.R. Augenstein
Advisor: J.S. Baras

M.S. 92-3



*Sponsored by
the National Science Foundation
Engineering Research Center Program,
the University of Maryland,
Harvard University,
and Industry*

Report Documentation Page				Form Approved OMB No. 0704-0188	
Public reporting burden for the collection of information is estimated to average 1 hour per response, including the time for reviewing instructions, searching existing data sources, gathering and maintaining the data needed, and completing and reviewing the collection of information. Send comments regarding this burden estimate or any other aspect of this collection of information, including suggestions for reducing this burden, to Washington Headquarters Services, Directorate for Information Operations and Reports, 1215 Jefferson Davis Highway, Suite 1204, Arlington VA 22202-4302. Respondents should be aware that notwithstanding any other provision of law, no person shall be subject to a penalty for failing to comply with a collection of information if it does not display a currently valid OMB control number.					
1. REPORT DATE 1991		2. REPORT TYPE		3. DATES COVERED 00-00-1991 to 00-00-1991	
4. TITLE AND SUBTITLE Parameter identifcaiton of Large Spacecraft Systems, based on the Frequency Characteristics of the Hankel Operator				5a. CONTRACT NUMBER	
				5b. GRANT NUMBER	
				5c. PROGRAM ELEMENT NUMBER	
6. AUTHOR(S)				5d. PROJECT NUMBER	
				5e. TASK NUMBER	
				5f. WORK UNIT NUMBER	
7. PERFORMING ORGANIZATION NAME(S) AND ADDRESS(ES) University of Maryland,The Graduate School,2123 Lee Building,College Park,MD,20742				8. PERFORMING ORGANIZATION REPORT NUMBER	
9. SPONSORING/MONITORING AGENCY NAME(S) AND ADDRESS(ES)				10. SPONSOR/MONITOR'S ACRONYM(S)	
				11. SPONSOR/MONITOR'S REPORT NUMBER(S)	
12. DISTRIBUTION/AVAILABILITY STATEMENT Approved for public release; distribution unlimited					
13. SUPPLEMENTARY NOTES					
14. ABSTRACT see report					
15. SUBJECT TERMS					
16. SECURITY CLASSIFICATION OF:			17. LIMITATION OF ABSTRACT	18. NUMBER OF PAGES 121	19a. NAME OF RESPONSIBLE PERSON
a. REPORT unclassified	b. ABSTRACT unclassified	c. THIS PAGE unclassified			

Abstract

Title of Thesis: Parameter Identification of Large Spacecraft
 Systems, based on the Frequency Characteristics
 of the Hankel Operator

Name of candidate: Donald R. Augenstein

Degree and Year: Master of Science, 1991

Thesis directed by: Dr. John Baras,
 Professor,
 Department of Electrical Engineering

The identification of the structural modes and damping factors of a spacecraft in orbit is accomplished. A systems approach was used to analyze the experiment and present identification techniques utilizing the frequency characteristics of the Hankel operator. Frequency domain error bounds and time domain error bounds are considered.

The experiment was performed on a satellite in conjunction with the Naval Research Laboratory. The experiment utilized ground based laser illumination with doppler shifted returns and identified three of the lowest vibration modes.

Parameter Identification of
Large Spacecraft Systems, based on the
Frequency Characteristics of the Hankel Operator

by

Donald R. Augenstein

Thesis submitted to the Faculty of The Graduate School
of The University of Maryland in partial fulfillment
of the requirements for the degree of
Master of Science
1991

Advisory Committee:

Professor John Baras, Advisor

Professor Odd Asbjornsen, Advisor/Systems Engineering Dept.

Professor Inderjit Chopra

Acknowledgments

I would like to sincerely thank Dr. Shalom M. Fisher and the Naval Research Laboratory for the opportunity to work on this experiment.

I wish to thank all of the students, faculty and staff of the University of Maryland Systems Research Center for their continued support and encouragement. I also am grateful for the financial support provided through the Naval Research Laboratory Resident Graduate Fellowship program at the Systems Research Center.

Table of Contents

List of Tables	vi
List of Figures	vii
1 Introduction and Systems Approach	1
1.1 Technological Forces on Spacecraft Size	3
1.2 The Need for Structural Identification	6
1.3 Thesis Overview	7
2 Spacecraft Configuration and Experiment Description	8
2.1 Experiment Description	13
2.1.1 Doppler Shifted Laser Return	14
3 Modeling the Spacecraft Structural Properties	19
3.1 Euler Beam Model	20
3.2 Model Analysis Results	24
4 Structural Identification using Free-Decay Observations	29
4.1 Identification Introduction	29
4.2 The Hankel Operator and Error Bounds of Model Reduction schemes.	31
4.2.1 The Hankel Operator	32

4.2.2	Hankel Operator Properties	36
4.2.3	Balanced Realizations and Error Bounds	39
4.2.4	Optimal Hankel Norm Model Reductions	42
4.3	Modeling Infinite Dimensional Systems with Finite Dimensions .	43
4.3.1	Measuring the distance between truncated systems and infinite systems	45
4.3.2	Bounds and Convergence of Truncated Systems	47
4.3.3	LACE nuclearity assumptions and measurement noise . .	48
4.3.4	Convergence Criteria	49
4.4	Eigensystem Realization compared to Balanced Order Reduction	50
4.4.1	Eigensystem Realization Algorithm Construction compared to Schur method Order Reduction	52
4.5	Improvements to Eigensystem Realization using Minimum Model Error Estimation	54
4.5.1	Minimization of the Objective function	55
4.5.2	Optimization Problem formulation	58
4.5.3	Solving the Two-point boundary value problem by Multi- ple Shooting	60
4.6	Model Identification using Least-Squares model fitting	62
4.6.1	Autoregressive Models	63
4.6.2	Autoregressive model performance	65
4.7	Sampling Rate consideration	67

4.8	Example of Identification Technique performance using LACE	
	PDE model response	69
5	Analysis of Experiment with LACE spacecraft	75
5.1	Dynamic Body compensation	77
5.2	Identification Analysis	78
5.2.1	Identification Results	79
5.2.2	The Linearity Assumption	88
5.3	Convergence of the Hankel operator	89
5.4	Conclusions	104
6	BIBLIOGRAPHY	106

List of Tables

2.1	Boom Structural Properties	9
2.2	LACE Bus Inertial Properties	10
2.3	LACE Boom tip masses	10
3.1	LACE Boom Configuration Analyzed	25
3.2	LACE System Pitch vibration modes below 1 Hertz	25
4.1	Modal Identification of noisy PDE impulse response	70
4.2	L_∞ bound on model truncation	71
5.1	Length of Data samples for Observation window	81
5.2	Day91008 Identification Results: Modal Frequencies	84
5.3	Day91008 Identification Results: Damping Factors	84
5.4	Day91010 Identification Results: Modal Frequencies	85
5.5	Day91010 Identification Results: Damping Factors	85
5.6	Peak System Vibration Displacements: Day91008	88
5.7	Peak System Vibration Displacements: Day91010	89

List of Figures

1.1	Top-Down Flow of Technological Forces affecting System Analysis	2
1.2	Modern Satellite Power Sources	3
1.3	Modern satellite high power solar panels	5
1.4	Modern space structures	6
2.1	Spacecraft Configuration	11
2.2	Deployable boom construction	12
2.3	Laser sampling for LACE experiment	16
2.4	Doppler motion detection analysis	17
2.5	Power spectrum of reflected return signal	17
2.6	Observed Rigid Body motion Day 258	18
3.1	LACE boom boundary configuration	23
3.2	Pitch Plane modal shape: .01908 Hz	26
3.3	Pitch Plane modal shape: .1298 Hz	26
3.4	Pitch Plane modal shape: .2581 Hz	27
3.5	Pitch Plane modal shape: .3238 Hz	27

3.6	Pitch Plane modal shape: .7567 Hz	28
3.7	Pitch Plane modal shape: .8217 Hz	28
4.1	Modelling White Noise with Poles inside the Unit Disc	45
4.2	Convergence of modes on unit disc due to oversampling	69
4.3	Spectrum Sampled Data overlaid with Noise-free Spectrum	72
4.4	Singular values: ERA	72
4.5	Singular values: MME	73
4.6	Frequency Response: ERA	73
4.7	Frequency Response: ERA/MME	74
4.8	Frequency Response: AR	74
5.1	Measured Relative velocity Day91008	82
5.2	Measured Relative velocity Day91010	83
5.3	Effect of changing aspect angle on observed motion magnitude	84
5.4	Detected Modal Frequencies for days 91008 and 91010	86
5.5	Detected Modal Damping Factors for days 91008 and 91010	87
5.6	Nuclear Norm Truncated Hankel Operator Day91008	92
5.7	Cauchy Sequence of Nuclear Norms for Truncated Hankel Operator Day91008	92
5.8	Frobenius Norm Truncated Hankel Operator Day91008	93
5.9	Upper Bound of Cauchy Sequence for Frobenius Norm of Truncated Hankel Operator Day91008	93

5.10	Hankel Norm Truncated Hankel Operator Day91008	94
5.11	Upper Bound of Cauchy Sequence for Hankel Norm of Truncated Hankel Operator Day91008	94
5.12	Nuclear Norm Truncated Hankel Operator Day91010	95
5.13	Cauchy Sequence of Nuclear Norms for Truncated Hankel Oper- ator Day91010	95
5.14	Frobenius Norm Truncated Hankel Operator Day91010	96
5.15	Upper Bound of Cauchy Sequence for Frobenius Norm of Trun- cated Hankel Operator Day91010	96
5.16	Hankel Norm Truncated Hankel Operator Day91010	97
5.17	Upper Bound of Cauchy Sequence for Hankel Norm of Truncated Hankel Operator Day91010	97
5.18	Nuclear Norm Truncated MME Hankel Operator Day91008 . . .	98
5.19	Cauchy Sequence of Nuclear Norms for Truncated MME Hankel Operator Day91008	98
5.20	Frobenius Norm Truncated MME Hankel Operator Day91008 .	99
5.21	Upper Bound of Cauchy Sequence for Frobenius Norm of Trun- cated MME Hankel Operator Day91008	99
5.22	Hankel Norm Truncated MME Hankel Operator Day91008 . . .	100
5.23	Upper Bound of Cauchy Sequence for Hankel Norm of Truncated MME Hankel Operator Day91008	100
5.24	Nuclear Norm Truncated MME Hankel Operator Day91010 . . .	101

5.25	Cauchy Sequence of Nuclear Norms for Truncated MME Hankel	
	Operator Day91010	101
5.26	Frobenius Norm Truncated MME Hankel Operator Day91010 .	102
5.27	Upper Bound of Cauchy Sequence for Frobenius Norm of Trun-	
	cated MME Hankel Operator Day91010	102
5.28	Hankel Norm Truncated MME Hankel Operator Day91010 . . .	103
5.29	Upper Bound of Cauchy Sequence for Hankel Norm of Truncated	
	MME Hankel Operator Day91010	103

Introduction and Systems Approach

In recent years, the size of satellites' structures that are being developed has increased dramatically. Operational power requirement growth has outpaced the ability of standard solar panels. Correspondingly, new design problems have arisen. In order to handle these technological difficulties, a systematic analysis of the space structures is required. This study incorporates a cross-disciplinary approach that is required in order to analyze a technological requirement, namely on-orbit structural identification.

In the following sections, the basis of the need for larger satellites and solar panels is explained. The power requirement solution may follow different technical paths. A very simple trade-off analysis leaves the designer with solar panels as the preferred power source. The power requirement thus drives the requirement for larger sized panels. These larger panels cause structural problems which require monitoring and analysis. The identification and monitoring requirement leads to the topic of this thesis, which is ground based laser measurement of satellite motion and the parameter identification of the structural

modes.

A top-down diagram of the technological flow that drives this experiment is shown in Figure 1.1. This figure diagrams how disparate top-level factors of requirements lead to the need for large space systems. These systems generate technological concerns, one of which is structural analysis. The solutions of this concern fan out to a variety of choices. The choice of remote sensing is the topic of this thesis. The following sections will explain in more detail the technological factors that contribute to the system.

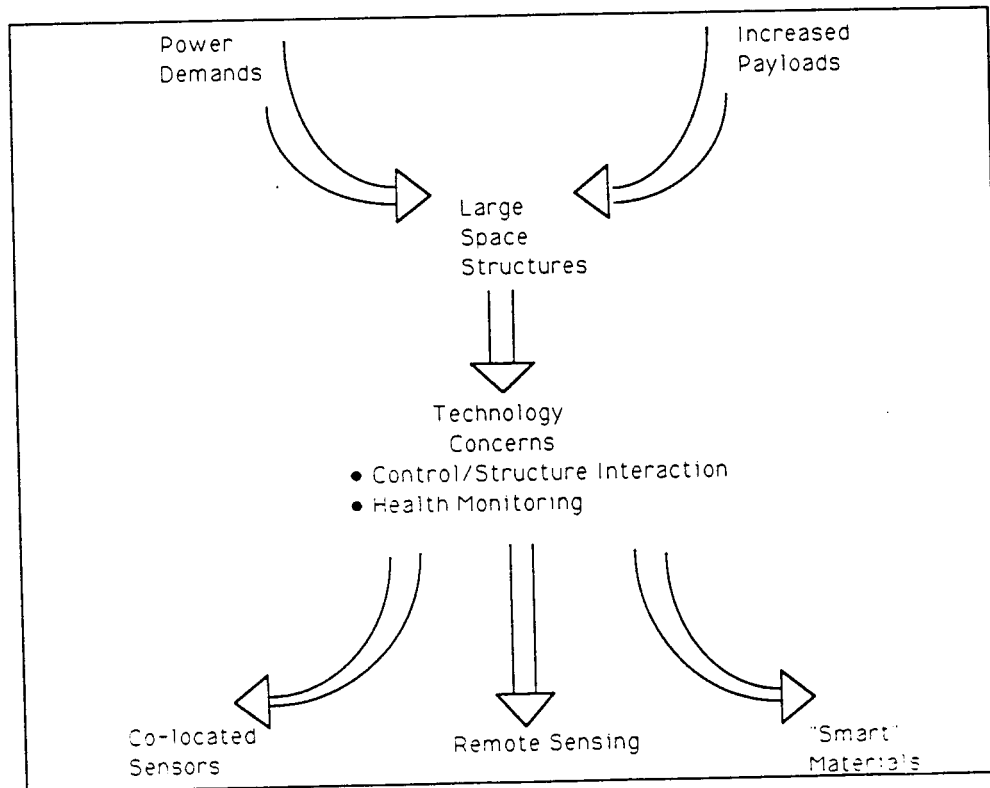


Figure 1.1: Top-Down Flow of Technological Forces affecting System Analysis

1.1 Technological Forces on Spacecraft Size

There are two technological forces driving the increasing size of space structures. The first is the increased on-board power demands for communication, scientific, and military payloads. Typical communication satellites require between 1 and 1.5 kilowatts of power during their lifetimes. The new SDI space-borne weapon systems may require 20 times this amount. These power requirements have surpassed the capacity of solar panels directly mounted to the rigid body. To satisfy these requirements either solar panels or nuclear reactors can be used (see Figure 1.2). The latter source is typically an unacceptable solution because of safety and political reasons. Still, the current technology for solar panels can

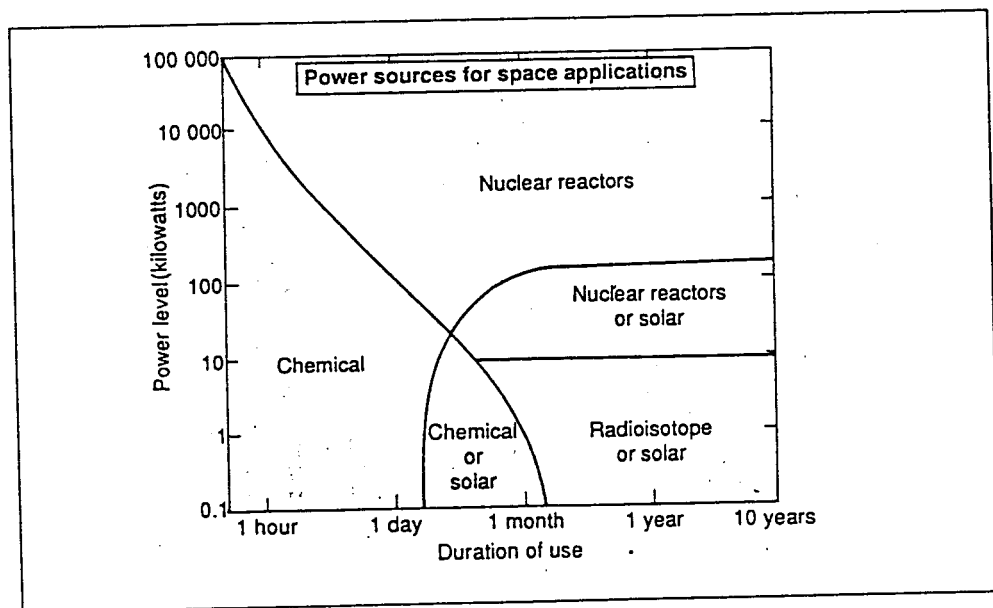


Figure 1.2: Modern Satellite Power Sources

only keep up with such demands by increasing the size of solar panels. Simply increasing the size of the spacecraft, however, will not provide enough surface

area exposed to solar radiation to meet the required power demands.

The solution has been to use large deployable solar panels or wings. These large wings are light weight and constructed with graphite composite material but are susceptible to large flexible motion. This motion may be driven by solar wind, atmospheric drag, or interaction with the spacecraft's main body. Rigid body dynamics, system vibratory motion, and solar tracking actuators characterize this latter motion which is transferred to the solar wings at the wing/bus interface thus exciting the wings' vibration (See Figure 1.3).

The second technological force is the development of complex scientific experiments and payloads. These payload require large structures such as the space station or complex antenna booms. Construction of such structure will require extended light weight booms and elements. These elements typically will be built from hinged graphite elements and deployable truss booms (See Figure 1.4). The spacecraft that is the subject of this study will fall into this second category of large space structures.

These new space structures utilize light weight materials which will have low damping factors. Stiffness requirements for structural rigidity contribute to the low internal damping. The combination of large elements and low damping creates new design challenges as the spacecraft lowest vibration frequencies begin to extend into the lower frequencies. Because of light damping, all control signals or input forces are required not to generate signal with frequency components near these vibrational modes. Any dynamic motion that generates forces near

these modes may excite large vibrational motion. This resonant motion may present an operational nuisance, but in some cases, it could become disastrous. Unfortunately, as the scale of deployed structures get larger, the lower modal frequencies may begin to seriously limit the actuator operating range. Additionally, many actuators provide incremental pulses (such as stepper motors and thrusters) and the spectrum of such pulses are broad and will excite the structural modes.

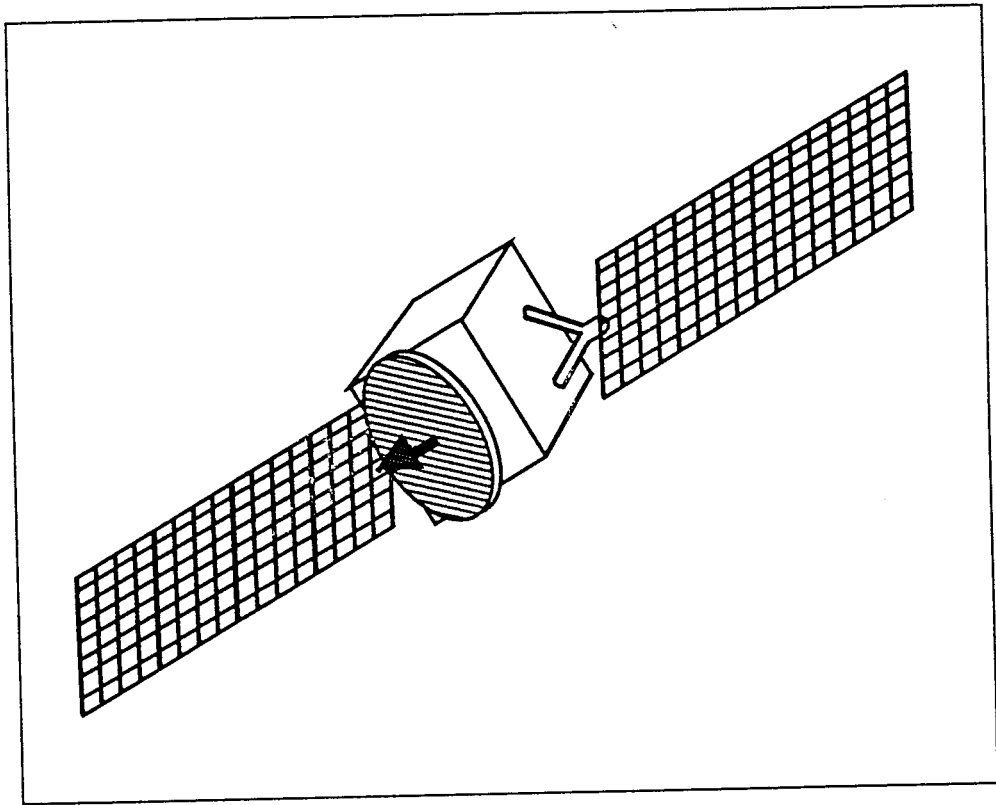


Figure 1.3: Modern satellite high power solar panels

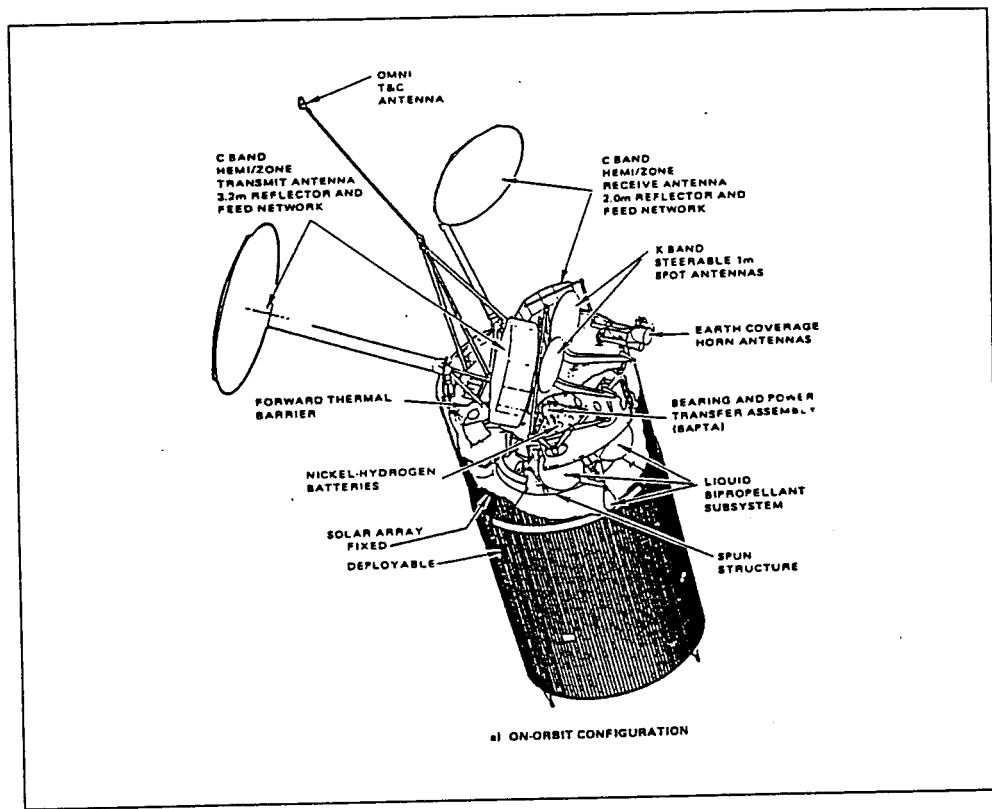


Figure 1.4: Modern space structures

1.2 The Need for Structural Identification

While structural analysis can predict modal frequencies with some degree of confidence, the structure configuration over a space structures life-cycle will not be constant. Normal reconfiguration requirements, mechanism decay and failure, and changes in structural properties will create complex structural configurations that may be increasingly hard to model, especially as unknown elements creep into the model formulation. Therefore, there exists a need to independently verify and identify structural behavior. A structural identification of the spacecraft in its “true” environment will provide confidence in analytical models

and hopefully point to areas where more research is needed. Identification can be used to monitor the spacecraft over its life and analyze trends in performance. Finally, in-flight modeling is a major step toward the goal of real-time adaptive attitude control and stabilization.

Interest in structural identification has recently expanded. Tests have been done by the US Air Force that tested structural modes on a boom while in a zero-gravity environment. This was done in the hold of an airplane while in a parabolic dive. Currently, there are plans to perform a similar experiment in the hold of the space shuttle. The experiment of this thesis has the advantage of testing flight hardware using simple low cost hardware and accomplishing similar goals.

1.3 Thesis Overview

This thesis accomplishes parameter identification on an in-orbit satellite. In Chapter 2, the satellite on which the structural identification will be performed is described. In Chapter 3, the structural modeling techniques used to model the spacecraft are presented. In Chapter 4, various algorithmic approaches are described that handle identification when dealing with noise corrupted data. In Chapter 5 the actual experiment is described and the results are presented. These results are fascinating in that using only small observation windows, the first three of four structural modes were detected.

CHAPTER TWO

Spacecraft Configuration and Experiment Description

The experiment was designed for the Low Atmospheric Control Experiment or LACE spacecraft. It is a low earth orbit satellite that was launched into a circular orbit with an altitude of approximately 550 kilometers and an inclination of 43 degrees. The LACE spacecraft structure is composed of a central rigid body or bus with three deployable booms (See Figure 2.1). The bus carries mission sensors and experiments, all supporting telemetry/command modules, attitude and control subsystem, and the solar panels.

Each of the deployable booms has a different mission function. The first boom is the gravity gradient boom and is oriented directly away from the earth. It has an electro-magnetic energy dissipating unit located at the tip. The energy dissipation unit is part of a passive attitude stabilization system that dumps destabilizing dynamic energy using the earth's magnetic fields.

The second boom is the retro-reflector boom and is deployed in the direction of the spacecraft velocity vector. The retro-reflector boom tip has a laser reflector unit mounted on it. These reflectors are part of the primary spacecraft

mission. Amongst these reflectors is a germanium reflector (approximately 1 inch diameter) that is dedicated to this structural dynamics experiment.

The third boom is the balance boom and is oriented 180 degrees from the retro-reflector boom. The balance boom has a strictly passive role of counter-acting the rigid body dynamics due to the retro-reflector boom. The rigid body and the balance boom also have germanium reflectors mounted upon them.

The spacecraft booms are both deployable and retractable. The deployed length varies from 0 feet up to 150 feet. The booms are constructed of light weight composite material with continuous longerons and stiff cross elements (See Figure 2.2). Since the boom lengths are variable, the system vibration modes are variable as well and are a function of the deployed length. The undeployed portion of the booms remains elastically coiled in the deploying canister mounted to the main spacecraft body. Additionally, the deploying canister has an elastic compliance. This compliance is incorporated in the vibration analysis, see Table 2.1 (also see Chapter 3).

density unit length kg/m	bending stiffness (EI) N-m ²	torsional stiffness (GJ) N-m ²	Rotating Inertia I_o unit/length kg-m	boom canister compliance N/radian
0.291	$\approx 1.55 \times 10^4$	631	1.33×10^{-7}	1.695×10^4

Table 2.1: Boom Structural Properties

The rigid central body has a mass of 1177 kilograms with moments and products of inertia listed in Table 2.2. These properties were experimentally

measured. The tip masses on each boom are listed in Table 2.3.

Inertia	$kg - m^2$
I_{xx}	1448.7
I_{yy}	1426.4
I_{zz}	1026.2
I_{xy}	3.61
I_{xz}	19.98
I_{yz}	14.86

Table 2.2: LACE Bus Inertial Properties

boom	kg
Gravity	90.7
Retro-reflector	15.9
Balance	15.9

Table 2.3: LACE Boom tip masses

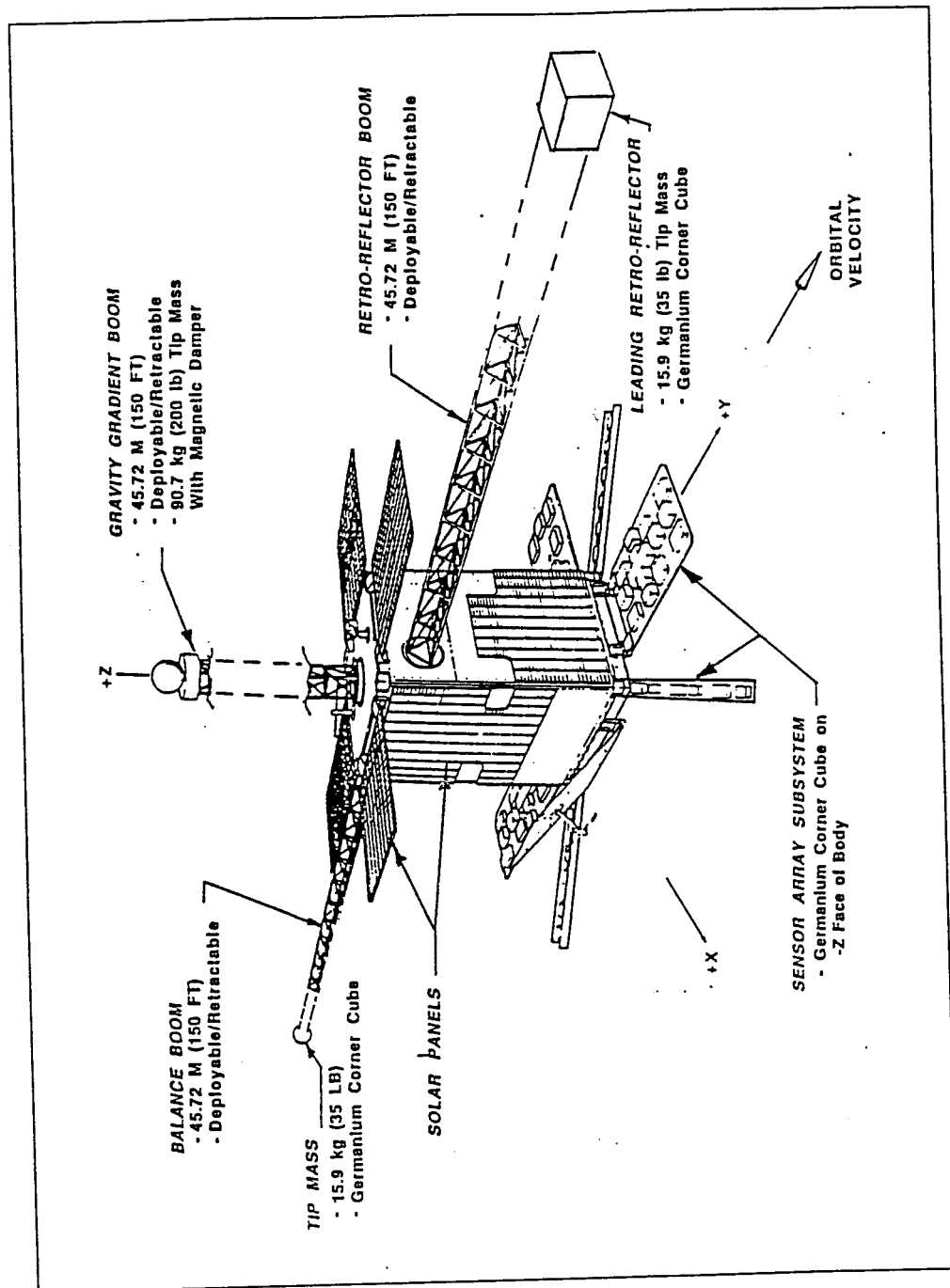


Figure 2.1: Spacecraft Configuration

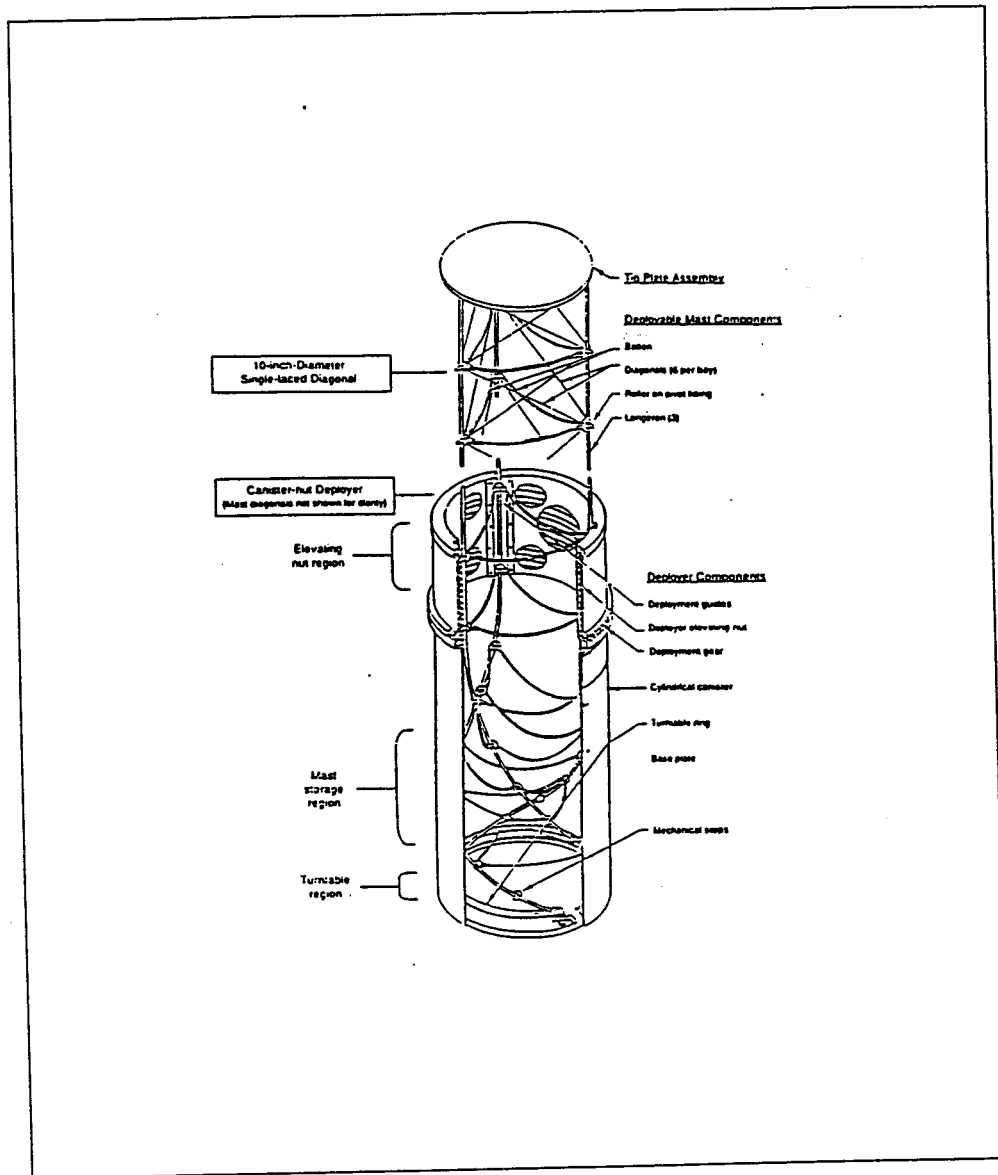


Figure 2.2: Deployable boom construction

2.1 Experiment Description

The experiment is to measure linear vibration of the complete structure and calculate the system modal frequencies and damping factors. The vibrations will be excited by the deployment and retraction of the lead boom. This type of excitation is due to the nonlinear coupling of the elastic strains of the booms in the canister. Additionally, the lead tip mass is offset from the axis of the boom. This offset provides a moment at the boom tip which will excite vibration. While the excitation forces involve nonlinear factors, the resulting vibration will end up being within the linear range (See chapter 3 on beam modeling).

Sampling the vibrations will be done remotely. Since the LACE spacecraft does not have telemetered data that directly indicates vibratory motion (such as strain gauges, gyros), the measurements must be taken indirectly or using off-board devices. Originally, the experiment had been designed to use two techniques to acquire vibration data.

1. The first technique uses a ground based laser to illuminate the germanium mirrors on the satellite (See section 1.1). The reflected laser signal will have a Doppler shift due to the relative motion of the satellite with respect to the laser source. The detected Doppler shift from each of the illuminated mirrors is then used to calculate this relative motion. (See Figure 2.3)
2. The second technique uses a spacecraft mounted optical sensor to detect vibration motion. The spacecraft sensor used to track stars or ground

based lasers. This sensor can track within precise tolerances (\approx milliradians). Using this sensor, the vibrations that influence the central body can be detected. Thus by calculating several coordinate transformations, the motion detected by the sensor can be projected onto the expected vibration axis.

Although considerable effort was put into the second approach, it was eliminated eventually from the experimental technique due to operational considerations. Specifically, there exists an operational constraint against optical tracking while the spacecraft was being illuminated by an 800 watt infrared laser. Considering that the reflected laser return provides greater resolution, the sensor tracking approach had to be eliminated.

2.1.1 Doppler Shifted Laser Return

The laser source and detection facility used is located at Lincoln Laboratories in Massachusetts. This facility was contracted to perform the actual laser measurements. The collected data was then sent to the Naval Research Laboratory where all the analysis was performed.

The data collection is done by pulsing the spacecraft with an infrared laser source and measuring the Doppler shifted return. The laser pulsing used a duty cycle of 62 Hz. This pulsing rate is higher than the modes targeted for detection (Ref. Chapter 3), but the oversampling provides a more reliable data set from which noise is more easily eliminated. Each pulse is sampled 4080 times in-phase

and in-quadrature (1.25 Mhz sample rate). The frequency components of the Fourier transform of the complex data set is analyzed to detect Doppler shifts in the return spectrum (See Figure 2.4). The Doppler shifts of each return source is calculated from the sampled power spectrum. The relative Doppler shift of each boom compared to the central bus is used to determine vibratory motion (See Figure 2.5).

In addition to the vibration motion, the Doppler shift will include the rigid body motion of the satellite's orbital motion. This rigid body motion becomes significant on the line of sight vector from an earth base observation reference. (See Figure 2.6). Considering that observation windows are time limited, elimination of this rigid body component will improve the potential resolution of the lowest vibration frequency modes [15] (Reference Chapter 3 for modal frequency analysis).

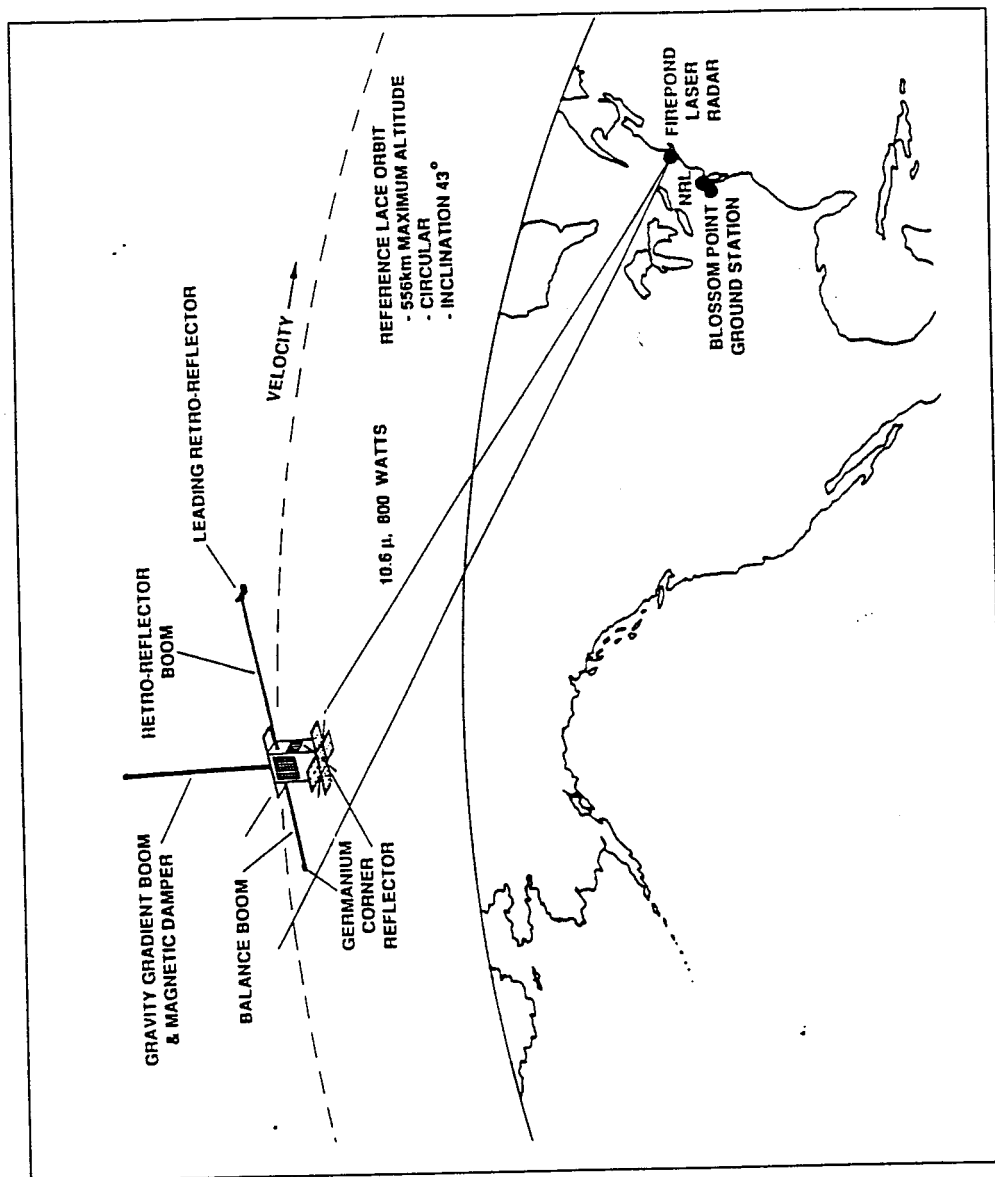


Figure 2.3: Laser sampling for LACE experiment

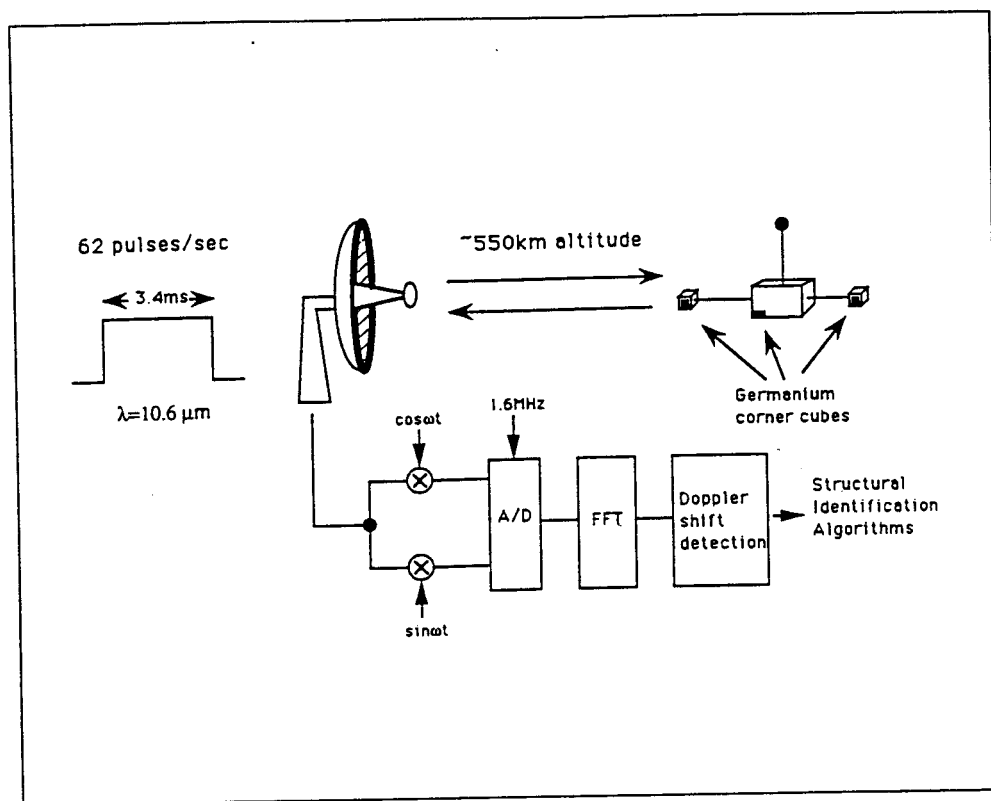


Figure 2.4: Doppler motion detection analysis

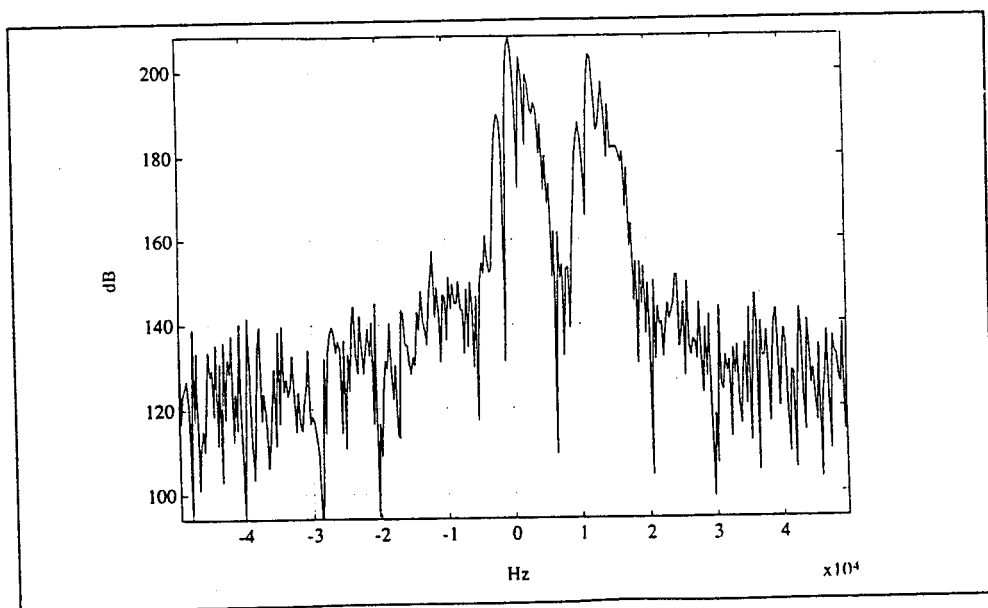


Figure 2.5: Power spectrum of reflected return signal

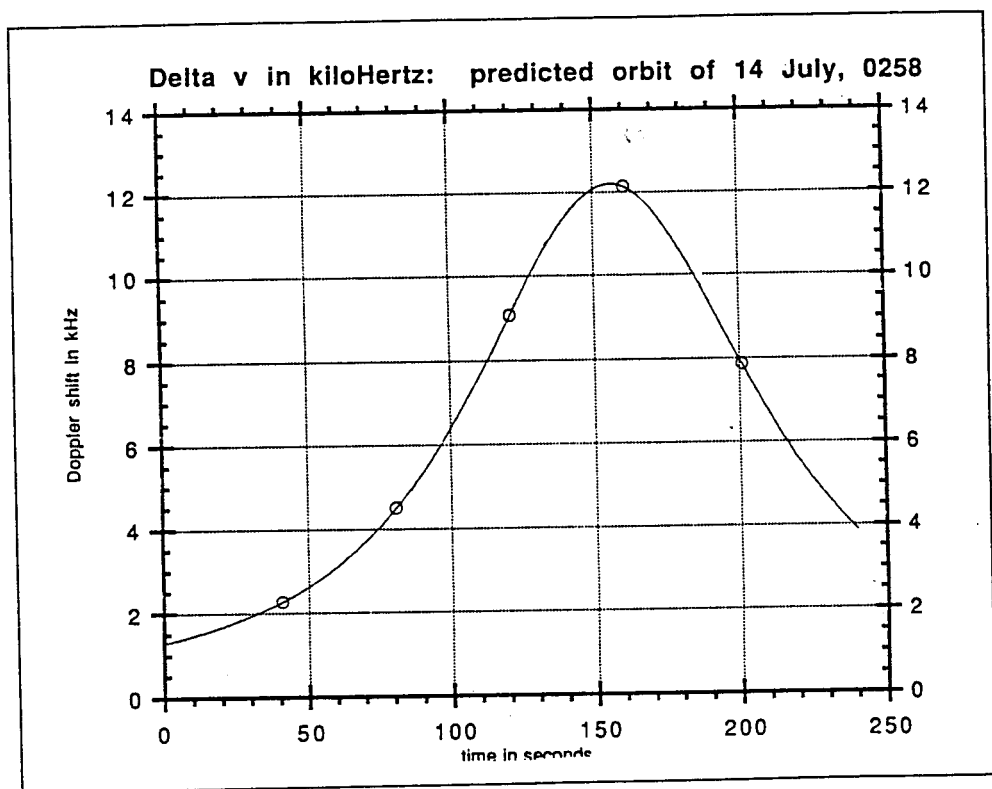


Figure 2.6: Observed Rigid Body motion Day 258

CHAPTER THREE

Modeling the Spacecraft Structural Properties

The modal analysis can be performed in two ways. The first approach is finite element modeling (FEM), and the second technique is a continuum approach through a partial differential equation model (PDE). The LACE geometry modeling lends itself to straightforward PDE solution. Once formulated, the solution of the PDE provides a quick and accurate solution. FEM also provides convenient three dimensional modeling, but its results will converge to PDE solutions only as the number of nodes becomes large. The advantage of FEM analysis is that software packages are readily available and easy to use. For this work, PDE solutions were used and FEM solutions were used as a comparison.

The PDE model provides some distinct advantages to the FEM approach. One, the number of parameters used in the model is greatly reduced. For the LACE experiment, the number of unknown structural properties are the boom stiffness and torsional stiffness, boom canister compliance, and boom internal damping factors (assuming all booms are identical). Additionally, any structural irregularities are lost within the homogenized model. The benefit of this

homogenization process was theoretically explained by Blankenship [10]. Finally, continuous models can be used directly in control analysis. The large order FEM models must be approximated using model truncation techniques before control system analysis can be performed ([18], [14]).

3.1 Euler Beam Model

The basic structural model used was the Euler beam. The Euler beam is the traditional choice because it is a linear model. More complicated models may provide more “accuracy”, however, they introduce nonlinear components. These nonlinear components obscure the definition of modal frequency and damping. Additionally, the degree of deflection expected in the experiment are within the engineering bounds of linearity.

The Euler beam basic assumptions are :

1. The cross-sectional dimensions are \ll than the length of the beam. This is the slender beam condition. For the booms of the LACE spacecraft, this condition is easily satisfied.
2. A plane cross-section drawn normal to the beam axis remains planar and normal to the beam axis after bending.
3. Shear displacement is very small compared to bending displacement.
4. The amount of rotation of any particular cross-section of the beam is \ll than the amount of deflection of the cross-section.

While these assumptions may be severe, they are essentially obeyed with the small excitation due to boom deployments. The booms are assumed to be cylindrical beams. This assumption was used in the FEM analysis also. Thus, the PDE model describing the flexible motion of the beam through any axis is described by:

$$\rho \frac{\partial^2 w(z, t)}{\partial t^2} + EI \frac{\partial^4 w(z, t)}{\partial z^4} = 0 \quad (3.1.1)$$

This equation assumes the material stiffness EI and mass per unit length ρ are uniform along the beam. The values for EI and ρ used in this equation are the same as those in Table 2.1. The solution is calculated by using the Laplace transform on the variable time in the equation. The equation (3.1.1) becomes:

$$\frac{\partial^4 \hat{w}(z, s)}{\partial z^4} + \frac{s^2 \rho}{EI} \hat{w}(z, s) = 0 \quad (3.1.2)$$

The solution to (3.1.2) is:

$$\hat{w}(z, s) = A_1 \cos \lambda z + A_2 \sin \lambda z + A_3 \cosh \lambda z + A_4 \sinh \lambda z \quad (3.1.3)$$

$$\lambda = \left(\frac{s^2 \rho}{EI} \right)^{\frac{1}{4}} \quad (3.1.4)$$

Given (3.1.4) and boundary conditions at each end of the beam, the coefficients A_i $i = 1, \dots, 4$ are solved. The boundary conditions considered for this experiment are tip masses and the boom canisters represented as spring elements at the bus (See Figure 3.1).

Likewise, the torsional partial differential equation is described by:

$$I_o \frac{\partial^2 \theta(z, t)}{\partial t^2} + GJ \frac{\partial^2 \theta(z, t)}{\partial z^2} = 0 \quad (3.1.5)$$

This equation assumes the torsional stiffness GJ and rotating mass inertia per unit length I_o are uniform along the beam. The values for GJ and I_o used in this equation are the same as those in Table 2.1. The solution is calculated by using the Laplace transform on the variable time in the equation. The equation (3.1.5) becomes:

$$\frac{\partial^2 \hat{\theta}(z, s)}{\partial z^2} + \frac{s^2 I_o}{GJ} \hat{\theta}(z, s) = 0 \quad (3.1.6)$$

The solution to (3.1.6) is shown to be

$$\hat{\theta}(z, s) = A_1 \cos \beta z + A_2 \sin \beta z \quad (3.1.7)$$

$$\beta = \left(\frac{s^2 I_o}{GJ} \right)^{\frac{1}{2}} \quad (3.1.8)$$

Using equation (3.1.8) and the boom's boundary conditions, the coefficients A_i are solved.

The complete PDE solution is calculated by solving the matrix of boundary conditions for all flexible motion equations. The individual booms connected at the spacecraft bus satisfy the dynamic and boundary conditions of the bus. The modal frequencies are then calculated from the boundary condition matrix.

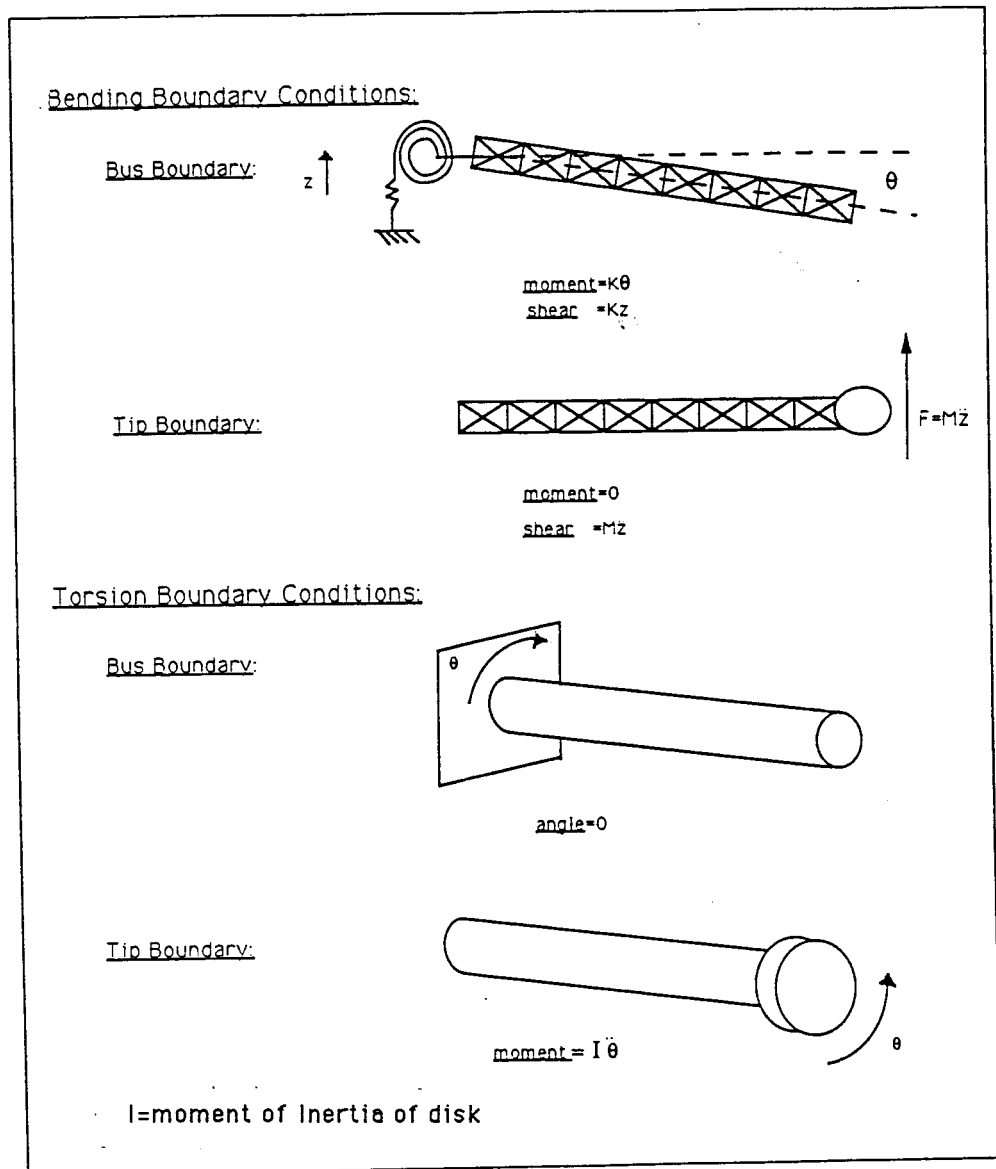


Figure 3.1: LACE boom boundary configuration

3.2 Model Analysis Results

Using the model of the previous section, the modal properties of the LACE spacecraft were determined. The spacecraft boom length configuration analyzed is listed in Table 3.1. This was the configuration of the spacecraft at the time of the identification experiment.

The pitch modes are the most likely detectable modes. For simplification the pitch modes were isolated from the yaw and roll modes. This speeds up analysis considerably. The isolation is accomplished by assuming the cross products of inertia are zero and that the booms are mounted exactly in line with the bus center of mass. This assumption is reasonable given the values for the product of inertia as shown in Table 2.2 are small. A study of the lowest pitch modes showed that the pitch modal frequencies were not sensitive to this assumption. Of course, for a more exact model all the vibration planes must be considered. The actual bus dimensions do marginally affect calculated pitch modes. The yaw and roll modes were calculated separately. In Table 3.2 the pitch modes are listed. Additionally, Table 3.2 lists the relative magnitude of displacement experienced at the lead tip for each mode. Relative displacement is the ratio of tip deflection to peak mode deflection. This ratio gives some insight to which modes are most likely to be detected with the ground based laser. Displacement ratios which exhibit large motions at the modal frequency are more likely to be detected (See Figure 3.2 through 3.7). However, it should be noted that there

is no guarantee any particular mode will be excited. This is due to the lack of control of the excitation mechanism. It should be noted that the vibration mode at .7567 Hz is primarily due to the modeled spring compliance of the boom canister. Changing the boundary condition at the spacecraft to a fixed clamp drastically changes this mode. As the modal frequencies get higher, the displacement ratios get larger. This suggests that if the system higher modes could be excited, then they could be easily detected. Unfortunately, the low energy excitation force used in this experiment is not expected to generate the higher modes.

Boom	length (ft)
Gravity Gradient	150
Retro-Reflector	15
Balance	150

Table 3.1: LACE Boom Configuration Analyzed

PDE hz	FEM hz	Displacement Ratio
.01908	.01906	0.0242
.1298	.12981	0.0063
.2581	.25782	0.0284
.3238	.32333	0.0565
.7567	.74952	0.4669
.8217	.81880	0.1068

Table 3.2: LACE System Pitch vibration modes below 1 Hertz

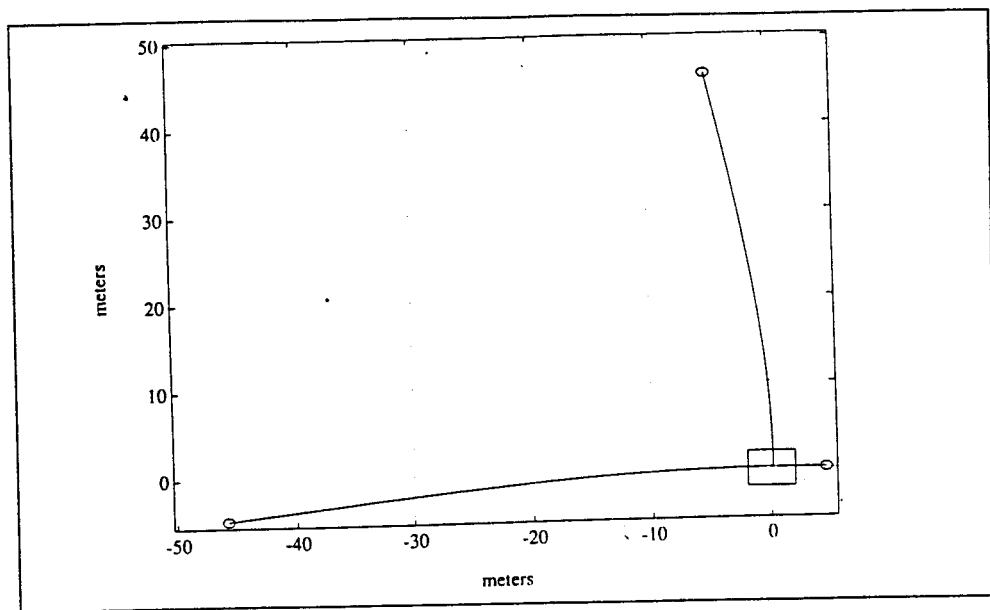


Figure 3.2: Pitch Plane modal shape: .01908 Hz

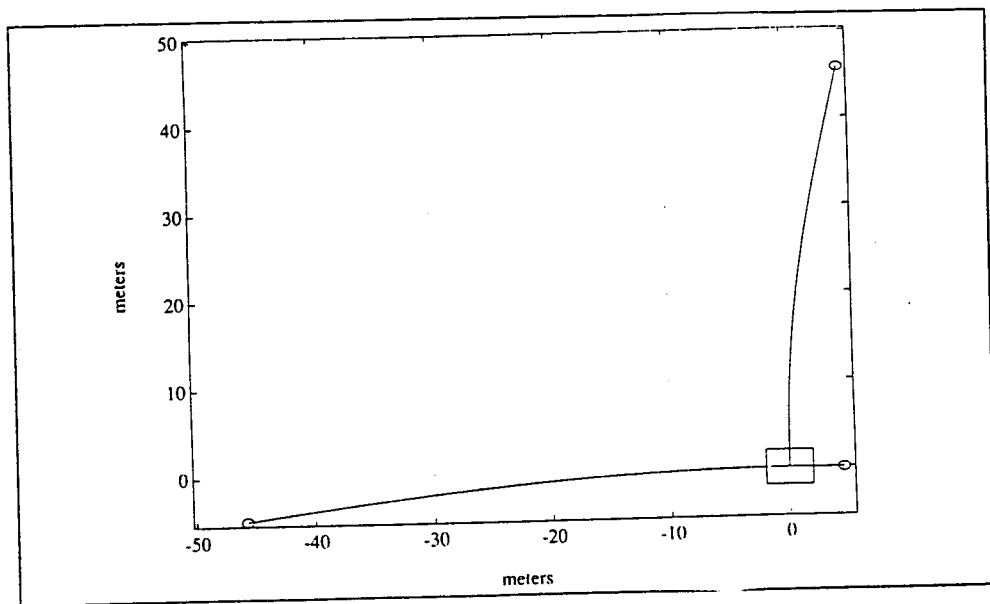


Figure 3.3: Pitch Plane modal shape: .1298 Hz

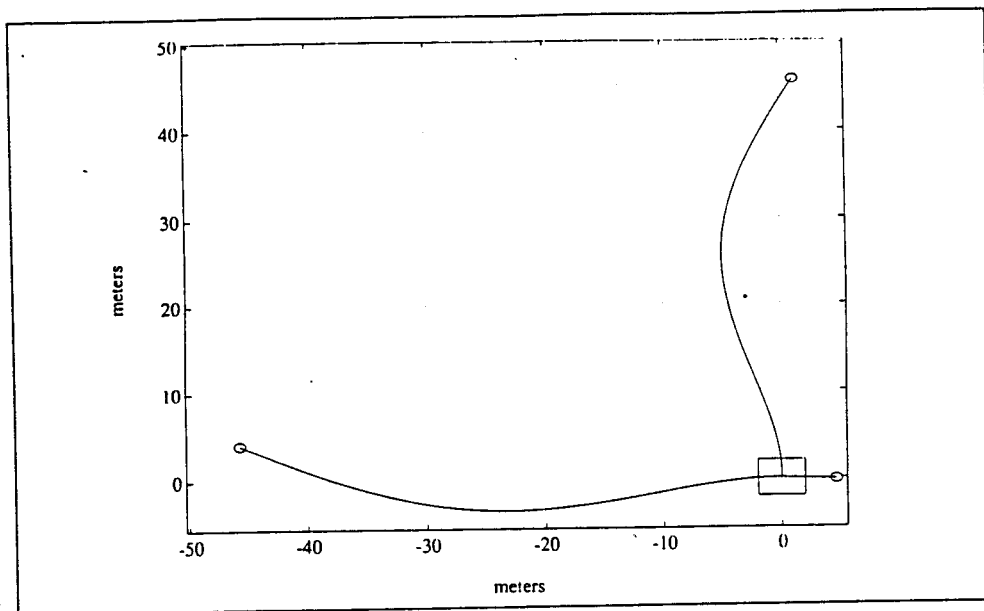


Figure 3.4: Pitch Plane modal shape: .2581 Hz

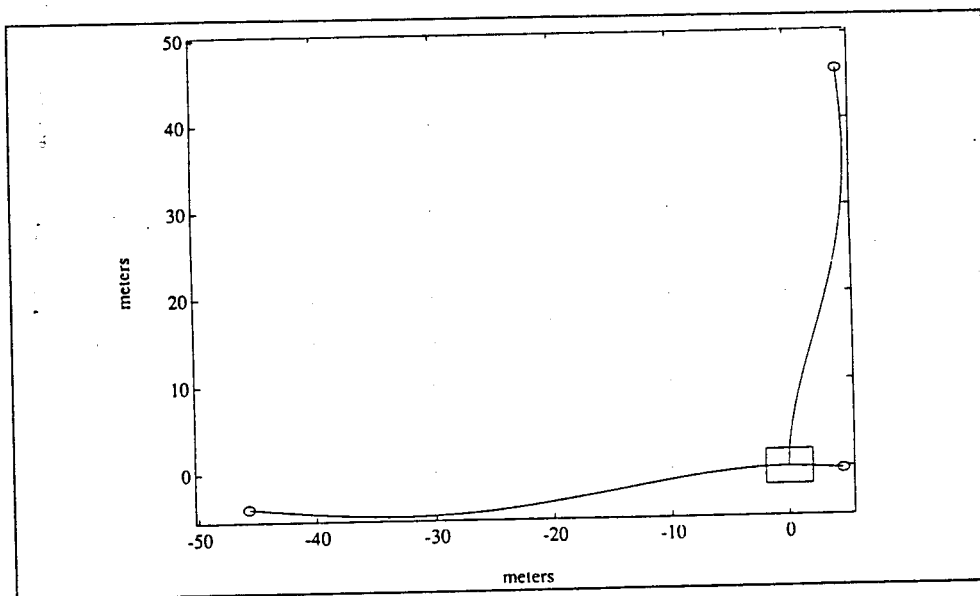


Figure 3.5: Pitch Plane modal shape: .3238 Hz

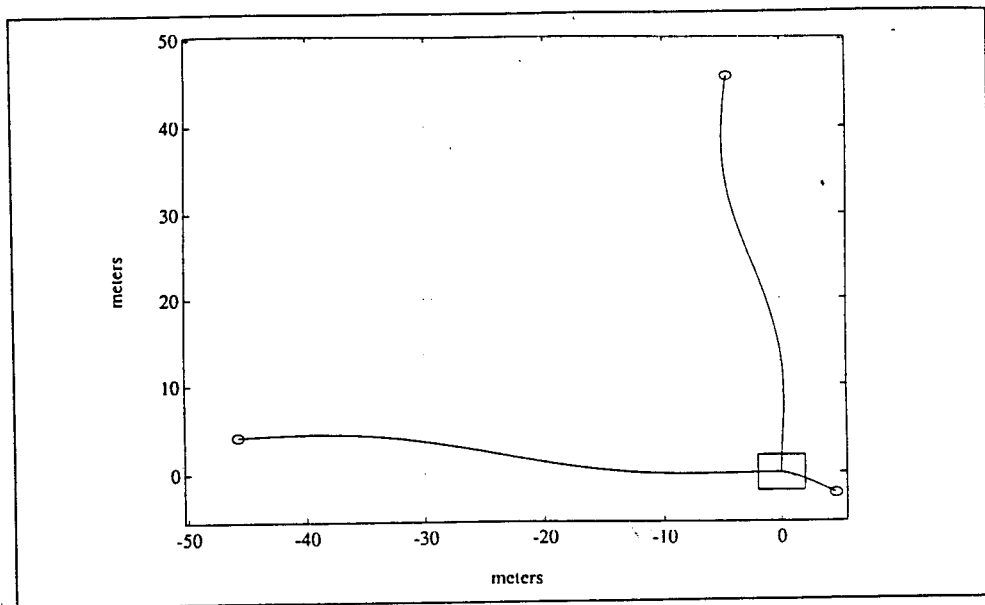


Figure 3.6: Pitch Plane modal shape: .7567 Hz

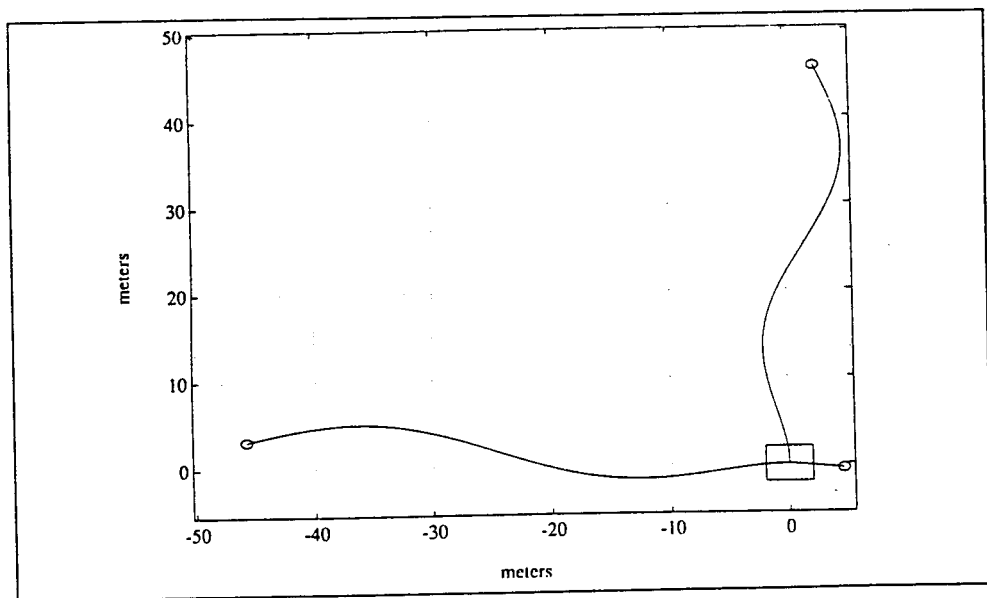


Figure 3.7: Pitch Plane modal shape: .8217 Hz

CHAPTER FOUR

Structural Identification using Free-Decay Observations

The LACE structural identification problem presents unique challenges. As described in chapter 3, the form of the excitation or driving function cannot be accurately modeled. Thus, the analysis will be limited to only the post-excitation free-decay measurements. Additionally, the observable measurement windows available for laser reflections are extremely limited in time. Given these two major limitations, the identification analysis must be robust in the presence of significant noise and must converge to a model given only a small window of measurements.

4.1 Identification Introduction

The project's goal is the accurate identification of the LACE spacecraft's system modal frequencies and, if possible, damping factors. Such experiments are vital compliments to a structural analysis computed by either finite element models or continuous partial differential equation models. A successful structural identification of the spacecraft in its "true" environment will provide confidence in

analytical models and hopefully point to areas where more research is needed. Additionally, in-flight modeling is a primary component toward the goal of real-time adaptive attitude control and stabilization.

As mentioned, the experiment will rely completely on free decay measurements. Thus limited, the system modeling will attempt to duplicate the structural internal dynamics with an impulse response model. The identification will utilize linear system theory which provides error bounds on the model's performance. The performance criteria that will be considered are the functional norms L_2 , $L_2[0, \infty)$, L_∞ , Frobenius ($\|\cdot\|_F$), Nuclear ($\|\cdot\|_N$) and the Hankel ($\|\cdot\|_H$). The system identification's performance is measured by the comparison of the true structural free-decay and the linear model's impulse response. Performance in both the time domain and the frequency domain will be addressed.

Historically, the identification of large structures by using an impulse response is relatively recent. The most striking improvement to structural identification was the Eigensystem Realization Algorithm (ERA) suggested by Juang *et al* [13]. This algorithm is theoretically inspired by the Kalman-Ho algorithm [2] but differs by utilizing the more numerically robust approach of singular value decomposition. Even more recently, Mook *et al* [4] presented the Minimum Model error approach. This approach, coupled with ERA, provides improved performance over that of ERA alone [5].

While these two approaches were effective in parametric identification, they did not provide the theoretical background to explain the accuracy of the al-

gorithms or to calculate any error bounds associated with the identification. In this chapter the error bounds associated with ERA and ERA/MME will be shown.

In section 4.2 the background of the Hankel operator is presented and the error bounds of truncating models are shown for balanced truncation and of optimal Hankel norm reductions. In section 4.3 the modeling of infinite dimensional systems will be addressed. In section 4.4 the ERA algorithm is derived considering the balanced realization approach. In section 4.5 the Minimum Model Error approach is explained using Pontryagin's approach, and the solution to the two-point boundary value problem is solved using linear algebra as proposed by Mook [6]. In section 4.6 a novel approach of least-squares modeling with balanced order reduction will be proposed. In section 4.7 explanation of optimal sampling is discussed. Finally, section 4.8 an example will be explored using data generated from the impulse response of a spacecraft model.

4.2 The Hankel Operator and Error Bounds of Model Reduction schemes.

The Hankel operator and the properties of its singular values are central to all model order reduction schemes. In this section the relation of the Hankel operator and the controllability and observability grammians is shown. Using these properties, a linear model can be constructed that will model the true response within a given bound. In the background development, the Hankel operator is

considered for both discrete and continuous systems. The motivation for this is that although the spacecraft structural system is a distributed continuous infinite dimensional system, all the experimental data is confined to the sampled discrete domain. It was shown that the singular values of a continuous system Hankel operator are identical to its discretized counterpart [11].

4.2.1 The Hankel Operator

All realizations constructed utilizing the properties of the Hankel operator will be modeled using the standard state space notation [16]. For finite order continuous systems this representation is:

$$\dot{x}(t) = Ax(t) + Bu(t) \quad (4.2.1)$$

$$y(t) = Cx(t) + Du(t) \quad (4.2.2)$$

For discrete systems this representation is:

$$x(n+1) = Ax(n) + Bu(n)$$

$$y(n) = Cx(n) + Du(n)$$

Given this format, the controllability and observability operators are then defined.

Definition 4.1 *For a given a state space representation (A, B, C) , the controllability operator maps future inputs to the internal states $\Psi_c : L_2[0, \infty) \rightarrow C^n$.*

For continuous systems this is defined as:

$$\Psi_c u \equiv - \int_0^\infty \exp(-A\tau) B u(\tau) d\tau$$

For discrete systems $\hat{\Psi}_c : l_2[0, \infty) \rightarrow C^n$ is defined as:

$$\hat{\Psi}_c u \equiv \sum_{k=0}^{\infty} A^k B u(k)$$

Definition 4.2 For a given state space representation (A, B, C) and internal state $x \in C^n$, the observability operator maps the internal state to past outputs $\Psi_o : C^n \rightarrow L_2(-\infty, 0]$. For continuous systems this is defined as:

$$(\Psi_o x)(t) \equiv C \exp(At) x$$

For discrete systems $\hat{\Psi}_o : C^n \rightarrow l_2(-\infty, 0]$ is defined as:

$$(\hat{\Psi}_o x)(k) \equiv C A^k x$$

Note: That if (A, B) is controllable then Ψ_c is surjective and if (A, C) is observable then Ψ_o is injective. Since these operators are Hilbert space isomorphisms (ie. they map from one Hilbert space to another), the adjoint operators exist.

Definition 4.3 For a given a state space representation (A, B, C) , the adjoint controllability operator maps internal states to future inputs $\Psi_c^* : C^n \rightarrow L_2[0, \infty)$. For continuous systems this is defined as:

$$(\Psi_c^* x)(t) \equiv -B^T \exp(-A^T t) x$$

For discrete systems $\hat{\Psi}_c^* : C^n \rightarrow l_2[0, \infty)$ is defined as:

$$(\hat{\Psi}_c^* x)(t) \equiv B^T (A^T)^k$$

Definition 4.4 For a given a state space representation (A, B, C) , the adjoint observability operator maps past outputs to internal states $\Psi_o^* : C^n \rightarrow L_2(-\infty, 0]$. For continuous systems this is defined as:

$$\Psi_o^* y \equiv \int_{-\infty}^0 \exp(A^T \tau) C^T y(\tau) d\tau$$

For discrete systems $\hat{\Psi}_o^* : C^n \rightarrow l_2(-\infty, 0]$ is defined as:

$$(\hat{\Psi}_o^* x)(t) \equiv \sum_{-\infty}^0 (A^T)^k C^T y(\tau)$$

The importance of these definitions, aside from proving reachability and detectability, is in the construction of the controllability and observability grammians and the Hankel operator.

Definition 4.5 Given a stable system (A, B, C, D) (i.e. the eigenvalues of A of a continuous system are all contained in the left hand side of the complex plane, for discrete systems all the eigenvalues are contained within the interior of the unit disc), the continuous controllability grammian is defined as:

$$P \equiv \int_0^\infty \exp(At) B B^T \exp(A^T t) dt = \Psi_c \Psi_c^* \quad (4.2.3)$$

and the discrete controllability grammian is defined as:

$$P \equiv \sum_{k=0}^\infty A^k B B^T (A^T)^k = \hat{\Psi}_c \hat{\Psi}_c^* \quad (4.2.4)$$

Likewise, the observability grammian for continuous systems is defined as:

$$Q \equiv \int_0^\infty \exp(A^T t) C^T C \exp(A t) dt = \Psi_o^* \Psi_o. \quad (4.2.5)$$

and the discrete controllability grammian is defined as:

$$Q \equiv \sum_{k=0}^{\infty} (A^T)^k C^T C A^k = \hat{\Psi}_o^* \hat{\Psi}_o \quad (4.2.6)$$

For a stable continuous system these grammians, P and Q, will solve the following equations [16].

$$AP + PA^T + BB^T = 0 \quad (4.2.7)$$

$$A^T Q + QA + C^T C = 0 \quad (4.2.8)$$

and for stable discrete systems, these grammians will solve.

$$P - APA^T - BB^T = 0 \quad (4.2.9)$$

$$Q - A^T QA - C^T C = 0 \quad (4.2.10)$$

Definition 4.6 For a given system with impulse response $h(t)$ ($h(k)$ for discrete systems), the Hankel operator is defined as the operator that maps past inputs to future outputs, $\Gamma : L_2(-\infty, 0] \rightarrow L_2[0, \infty)$. This operator for continuous systems is expressed as:

$$(\Gamma u)(t) = \int_0^\infty h(t+s)u(s)ds$$

and for discrete systems $\Gamma : l_2(-\infty, 0] \rightarrow l_2[0, \infty)$ is expressed as:

$$(\Gamma u)(n) = \sum_0^\infty h(k+n)u(k)$$

For linear systems, the Hankel operator is easily constructed using the controllability and observability operators.

$$(\Gamma u)(t) = \Psi_o \Psi_c \quad (4.2.11)$$

4.2.2 Hankel Operator Properties

The fundamental relation between the Hankel operator and the controllability and observability grammians is shown in the following theorem.

Theorem 4.1 *The spectral decomposition of the Hankel operator is related to the eigenvalue decomposition of PQ , as follows:*

$$\{\sigma_\Gamma\} = \{\lambda_i^{1/2}(PQ)\}$$

where σ_Γ represent the singular values of the Hankel operator (ref: Francis [9] (ch 5)).

Proof: let λ be a nonzero eigenvalue of $\Gamma^*\Gamma$ with respective eigenvector v then

$$\Gamma^*\Gamma v = \Psi_c^* \Psi_o^* \Psi_o \Psi_c v = \lambda v \quad (4.2.12)$$

Premultiplying (4.2.12) by Ψ_c and using equations (4.2.3) and (4.2.5) and letting $x = \Psi_c u$ gives:

$$PQx = \lambda x \quad (4.2.13)$$

Likewise, premultiplying equation (4.2.13) by $\Psi_c^* Q$ and defining $u = \Psi_c^* Qx$ gives equation (4.2.12) back again.

In the following section, the performance bounds of balanced truncations are shown. These performance bounds are directly related to the singular values of the Hankel operator.

All identification algorithms for this structural identification experiment are performed within the discrete domain. The desire is to put the Markov param-

eters into a format that allows for easy model construction and takes advantage of the truncation properties of the Hankel singular values. This is demonstrated by defining the controllability and observability operators in a matrix form.

Definition 4.7 *Given a discrete system (A, B, C) and input $u \in l_2(-\infty, 0]$ expressed as:*

$$u = [u(0)^T, u(-1)^T, \dots, u(-n)^T, \dots]^T$$

The infinite controllability matrix operator is expressed as:

$$\hat{\Psi}_c = [\begin{array}{ccccccc} B & AB & A^2B & \dots & A^{n-2}B & A^{n-1}B & \dots \end{array}] \quad (4.2.14)$$

Likewise, the infinite observability matrix operator can be expressed as:

$$\hat{\Psi}_o = [\begin{array}{ccccccc} C^T & A^T C^T & (A^T)^2 C^T & \dots & (A^T)^{n-2} C^T & (A^T)^{n-1} C^T & \dots \end{array}]^T \quad (4.2.15)$$

Thus, the Hankel operator defined by equation (4.2.11) is in fact an infinite dimensional matrix that maps $l_2(-\infty, 0] \rightarrow l_2[0, \infty)$ with the same singular values as shown in Theorem 4.1.

The advantage of the discrete Hankel operator is that it can be constructed directly from the Markov parameters or impulse response. The realization (A, B, C) has an impulse response defined by:

$$h(k) = CA^{k-1}B$$

The infinite dimension matrix Γ , therefore, can easily be constructed as follows:

$$\Gamma = \begin{bmatrix} h(1) & h(k+1) & \dots & h(k+n) & \dots \\ h(k+1) & h(k+2) & \dots & h(k+n+1) & \dots \\ \vdots & \vdots & & \vdots & \ddots \end{bmatrix} \quad (4.2.16)$$

$$= \begin{bmatrix} CB & CAB & \dots & CA^{k-1}B & \dots \\ CAB & CA^2B & \dots & CA^k & \dots \\ \vdots & \vdots & & \vdots & \ddots \end{bmatrix} \quad (4.2.17)$$

Equation (4.2.17) is identical to equation (4.2.11).

Though constructing the Hankel matrix is simple, several factors must be considered.

1. The Markov parameters $h(k)$ will be corrupted by noise. For the experiment of this report, the signal to noise ratio will most likely be low.
2. Computationally, working with an infinite dimensional matrix is impossible. Therefore, the Hankel matrix must be truncated to a finite order of n . The effect of truncating this matrix must be quantified.
3. The experiment's goal is parameter identification, thus the effects of noise corruption must be quantified.

The next section presents an error bound on model truncation and provides an explanation of the noise effects on the parameter identification. Following the next section, the effects of truncating of the infinite matrix are investigated.

4.2.3 Balanced Realizations and Error Bounds

The most important property of the Hankel operator is the relation between the hankel singular values and the frequency response. This relation will be exhibited with the error bound of a balanced order reduction.

While the realization (A, B, C) is invariant to transformations, the grammians P and Q are not. Moore [25] was the first to appreciate this and showed that there exists a transformation such that the grammians will become diagonal. That is:

$$TPT^T = \text{diag}(\Sigma_1, \Sigma_2, 0, 0)$$

$$(T^T)^{-1}QT^{-1} = \text{diag}(\Sigma_1, 0, \Sigma_3, 0)$$

where the matrices Σ_i are diagonal matrices with elements $\{\sigma_1, \sigma_2, \dots, \sigma_{n_i}\}$ arranged in descending order $\sigma_1 \geq \sigma_2 \geq \dots \geq \sigma_{n_i} \geq 0$. The transformed representation $(\tilde{A}, \tilde{B}, \tilde{C}) = (TAT^{-1}, TB, CT^{-1})$ will become:

$$\tilde{A} = \begin{bmatrix} \tilde{A}_{c,o} & 0 & * & 0 \\ * & \tilde{A}_{c,no} & * & * \\ 0 & 0 & \tilde{A}_{nc,o} & * \\ 0 & 0 & 0 & \tilde{A}_{nc,no} \end{bmatrix}$$

$$\tilde{B} = \begin{bmatrix} \tilde{B}_{c,o} \\ * \\ 0 \\ 0 \end{bmatrix}$$

$$\tilde{C} = \begin{bmatrix} \tilde{C}_{c,o} & 0 & * & 0 \end{bmatrix}$$

where the subscripts denote controllable, uncontrollable, observable, and unobservable subspaces.

Given this transformation, the controllable and observable portion of the representation will satisfy the following Lyapunov equations (for continuous systems).

$$\tilde{A}_{c,o}\Sigma_1 + \Sigma_1\tilde{A}_{c,o}^T + \tilde{B}_{c,o}\tilde{B}_{c,o}^T = 0$$

$$\tilde{A}_{c,o}^T\Sigma_1 + \Sigma_1\tilde{A}_{c,o} + \tilde{C}_{c,o}^T\tilde{C}_{c,o} = 0$$

Considering only the minimal portion of a representation, balanced model truncations are performed.

Definition 4.8 *Given an n^{th} order minimal balanced representation $(\tilde{A}, \tilde{B}, \tilde{C}, \tilde{D})$, with $P = Q = \text{diag}(\Sigma_1, \Sigma_2)$, where $\Sigma_1 = \text{diag}(\sigma_1, \dots, \sigma_k)$ and $\Sigma_2 = \text{diag}(\sigma_{k+1}, \dots, \sigma_n)$ arranged in descending order $\sigma_1 \geq \sigma_2 \geq \dots \geq \sigma_n \geq 0$, and the realization (A, B, C) conformally partitioned as:*

$$\tilde{A} = \begin{bmatrix} \tilde{A}_{11} & \tilde{A}_{12} \\ \tilde{A}_{21} & \tilde{A}_{22} \end{bmatrix}$$

$$\tilde{B} = \begin{bmatrix} \tilde{B}_1 \\ \tilde{B}_2 \end{bmatrix}$$

$$\tilde{C} = \begin{bmatrix} \tilde{C}_1 & \tilde{C}_2 \end{bmatrix}$$

Then a k^{th} order balanced reduced representation is (A_{11}, B_1, C_1, D) . (Reference [24] p.398)

Using the definition of the transfer function of $G(s) = D + C(sI - A)^{-1}B$, it was proven independently by Glover(1984) and Enns [8] using optimal Hankel norm approximations that L_∞ norm of the difference between the n^{th} order true system $G_n(s)$ and the internally balanced truncated k^{th} order model $\hat{G}_k(s)$ has the following bound.

$$\|G(s)_n - \hat{G}_k(s)\|_\infty = \sup_{w \in (-\infty, \infty)} |G_n(jw) - \hat{G}_k(jw)| \leq 2 \sum_{i=k+1}^n \sigma_i \quad (4.2.18)$$

The following engineering results may be deduced from the balanced order model reductions.

1. The spirit of balanced order truncations is that the least observable and controllable modes are the ones being truncated. The closer to zero the truncation singular values, the less observable or controllable. In this sense the truncation makes intuitive sense, since these modes are of least concern to a controller designer.
2. The L_∞ bound is significant if $\sigma_k \gg \sigma_{k+1}$ and σ_{k+1} is small. This implies that the sum of the tail of singular values is small and thus the L_∞ bound is tight.
3. The truncations can perform well, even when σ_{k+1} is close to σ_k . Glover

(1984) showed this could be true, since as $\sigma_{k+1} \rightarrow \sigma_k$ the poles of the truncation can approach the imaginary axis. In fact, as a pole tends to the imaginary axis, it tends to become either uncontrollable or unobservable. Thus, the truncated modes will have less affect on the model's performance. (Theorem 4.2 [11]).

4. If the realization (A, B, C) was constructed from noisy Markov parameters (ie. ERA realization), and if an estimate of the noise variance exists, then a comparison of the L_∞ bound and the noise power spectrum is useful. Given a noise power spectrum:

$$\Phi_{noise}(w) = \sum_{-\infty}^{\infty} R_{noise}(\tau) e^{-i\tau w}$$

if the L_∞ bound satisfies:

$$2 \sum_{i=k+1}^n \sigma_i \approx \sup_w |\Phi_{noise}(w)|$$

then the effects of the truncation is limited to the removal of modes that model the noise contributions.

4.2.4 Optimal Hankel Norm Model Reductions

An alternative model reduction scheme exists that provide the same L_∞ bounds. This approach is the optimal Hankel norm model reduction and was first presented by Glover (1984) using balanced realizations. The advantage of this approach is that in addition to the L_∞ bound the Hankel-norm bound is minimized. Begin first with the definition of the Hankel norm.

Definition 4.9 *The Hankel-norm of a system $G(s)$ with realization (A, B, C) is the largest singular value of its Hankel operator and is defined as:*

$$\|G(s)\|_H \equiv \bar{\sigma}(\Gamma_G) = \lambda_{\max}^{1/2}(PQ) \quad (4.2.19)$$

Glover showed that the Hankel the norm gives the L^2 gain for all past outputs to all future outputs.

$$\|G(s)\|_H = \sup_{u \in L^2(-\infty, 0)} \frac{\|y\|_{L^2(0, \infty)}}{\|u\|_{L^2(-\infty, 0)}} \quad (4.2.20)$$

The advantage of the optimal Hankel norm model reduction is that the Hankel norm of the difference between the true model and the reduced k^{th} order estimate is minimized and has the following Hankel norm.

$$\|G(s) - \hat{G}(s)\|_H = \sigma_{k+1}$$

Computationally, the calculation of the optimal Hankel norm model reduction is performed without a balancing transformation [22]. Nevertheless, for our experiment the balanced order reduction approach is usually chosen since it can be accomplished during construction of the realization (See section on ERA).

4.3 Modeling Infinite Dimensional Systems with Finite Dimensions

Equation (4.2.17) shows that the discrete time Hankel operator can be constructed exactly from the Markov parameters (i.e. the impulse response samples). Once constructed, the Hankel operator may be used to construct a realization (A, B, C) that will exactly duplicate the system's impulse response.

Properties of this linear realization are:

1. An n^{th} order realization will exactly match the first $2n$ Markov parameters.

The model's Markov parameters later than $2n$ will differ from the true systems impulse response due to noise, nonlinear components, and higher order modes.

2. It requires an infinite dimensional system to exactly represent the true system's impulse response with added noise.

The second constraint can be visualized by looking at the frequency characteristic of white noise (See Figure 4.1). In order to exactly represent that frequency response, the model would require an infinite number of poles inside the unit disc.

Unfortunately, it is computationally impractical to consider handling infinite dimensional matrices. Additionally, the experimental conditions preclude anything but a finite test window. However, error bounds resulting from truncating infinite systems to finite systems have been investigated by Curtain *et al* [14]. The error bounds determined by Curtain will now be presented.

In order to consider infinite dimension space the following definition is required [3].

Definition 4.10 *An infinite dimensional discrete-time realization of a system (A, B, C) operating on a real separable Hilbert space H is as follows:*

$$x_{n+1} = Ax_n + Bu_n$$

$$y_n = Cx_n + Du_n$$

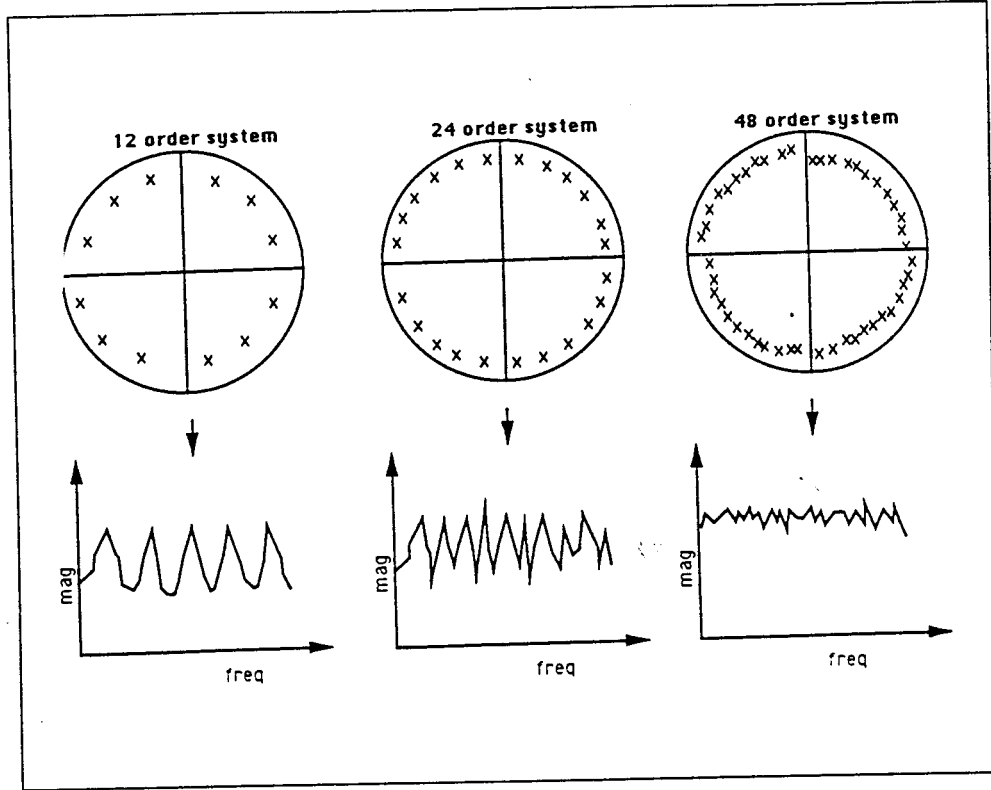


Figure 4.1: Modelling White Noise with Poles inside the Unit Disc

and A, B, C, D are linear operators such that:

$$A : H \rightarrow H \quad B : \mathbb{R}^m \rightarrow H \quad C : H \rightarrow \mathbb{R}^p \quad D : \mathbb{R}^m \rightarrow \mathbb{R}^p$$

The transfer function described by this infinite dimensions model $G(s)$ is defined by :

$$G(z) = C(zI - A)^{-1}B + D$$

4.3.1 Measuring the distance between truncated systems and infinite systems

In order to measure the effects of truncating an infinite Hankel operator the following norms will be used:

Definition 4.11 *A system is power-stable if there exists $M > 0$ and $r \in [0, 1)$ such that $\|A^k x\| \leq Mr^k$ for all $x \in H$ and $k \in \{0, 1, 2, \dots\}$ (Ref [3]). The Hankel operator Γ associated with a power-stable system is nuclear and satisfies the following:*

$$\sum_{k=1}^{\infty} \sigma_k < \infty \quad (4.3.1)$$

The summation in equation (4.3.1) is referred to as the nuclear norm, $\|\cdot\|_N$. All bounded finite systems are nuclear, however, this is not strictly true with infinite systems. Note that this norm is the trace of the singular values, thus it is also called the trace norm [26].

Definition 4.12 *A power bounded or l_2 -stable system will satisfy the following constraint:*

$$\left(\sum_{k=1}^N \sigma_k^2\right)^{1/2} < \infty \quad (4.3.2)$$

The summation in equation (4.3.2) is referred to as the Frobenius norm, $\|\cdot\|_F$.

The nuclear, Frobenius, and Hankel norms all satisfy the basic norm properties of:

1. $\|\alpha A\| = |\alpha| \|A\|$
2. $\|A\| \geq 0$ with equality if and only if $A = 0$
3. $\|A + B\| \leq \|A\| + \|B\|$ The triangle inequality

Additionally, these norms are unitarily invariant. That is for any matrix U that satisfies $UU^T = I$ the norm of Γ is unaffected by multiplication with U .

$$\|U\Gamma\| = \|\Gamma U\| = \|\Gamma\|$$

4.3.2 Bounds and Convergence of Truncated Systems

Systems with the property of nuclearity have an important bound on the l_1 norm of the impulse response. This bound was shown by Curtain (1988)[Theorem 2.1] and the bound for discrete systems is stated without proof.

$$\sum_{i=0}^{\infty} |h(i)| = \|h\|_1 \leq 2\|\Gamma\|_N \quad (4.3.3)$$

What must be quantified are the effects of truncating the infinite Hankel operator matrix in equation 4.2.11 to a finite order matrix. Let Γ_n represent the n^{th} order approximate to the complete Hankel operator Γ . Of interest is the size of appropriate norms on the difference between the truncated and infinite operators $\|\Gamma - \Gamma_n\|$.

Curtain *et al* showed that if the system impulse response $h(t) \in L_1 \cap L_2$ and the Hankel operator was nuclear, then the truncation of the Hankel operator will converge to the true Hankel operator as the order n gets large. That is:

$$\|\Gamma_n - \Gamma\|_N \rightarrow 0 \quad (4.3.4)$$

$$\|h_n - h\|_1 \rightarrow 0 \quad (4.3.5)$$

$$\|h_n - h\|_2 \rightarrow 0 \quad (4.3.6)$$

These intuitive conclusions for a stable system also come with error bounds on performance. This error bound is similar to the one for balanced order truncations. The bound is as follows:

$$\|G - G_n\|_\infty \leq 2 \sum_{i>n} \sigma_i$$

Where G and G_n are the transfer functions associated with the respective Hankel operators. Additionally, there exist performance bounds on the L_1 and L_2 norms on the difference between the truncated and infinite impulse responses.

4.3.3 LACE nuclearity assumptions and measurement noise

A necessary assumption of Curtain *et al* (1988), is that the system is nuclear and an element of $L_1 \cap L_2$ functions. Nuclearity is dependent on the system under study. It was shown by de Vries [7] that a system constructed via the Laplace transform of a partial differential equation model of a deployed spacecraft essentially equivalent to the LACE spacecraft is in fact nuclear. A necessary assumption is that the booms have viscous damping (See chapter 2). This assumption is quite reasonable since the structural damping factor tested on ground was greater than 1 percent. Additionally, any damped structural system is definitely an element of L_1 . Thus, the assumption of nuclearity is reasonable.

Unfortunately, noisy experimental data will not be nuclear. Since the all measurements are corrupted by noise, the assumption that the measured system is an element of l_1 will not be valid. Referring to equation (4.3.3), it is clear that the assumption of nuclearity of measured data will be violated.

Thus, any model that includes the effects of measured noise will nullify possible bounds on the truncation of the Hankel operator. While this might seem disappointing, it certainly is a logical outcome. However, modeling that is done in a stochastic sense will not be confined to attempting to model noise. The convergence of equations (4.3.4) through (4.3.6) may indeed occur. This difference between deterministic modeling with truncation and stochastic modeling with truncation is the primary advantage of the approaches MME and least-squares modeling.

4.3.4 Convergence Criteria

In order to calculate the Nuclear, Frobenius and Hankel norms, the finite operator Γ_n will be augmented with zeros such that its dimensions match that of the complete operator.

$$\hat{\Gamma}_n = \begin{bmatrix} \Gamma_n & 0 & \dots \\ 0 & 0 & \dots \\ \vdots & \vdots & \ddots \end{bmatrix}$$

The trace norm has the property that for balanced hankel operators, the norm of $\|\Gamma - \Gamma_n\|_N$ will equal the difference of the independent trace norms.

$$\|\Gamma - \Gamma_n\|_N = \|\Gamma\|_N - \|\Gamma_n\|_N$$

The Hankel and Frobenius norms do not have this property, therefore, the triangle inequality must be used to bound the performance of these two norms.

How a truncated Hankel operator characteristics converges to the characteristics of the infinite Hankel operator will be measured using a Cauchy sequence of operators Γ_i where $i : 1 \rightarrow \infty$. The quality of convergence will be determined how close Γ_i is to Γ_{i+1} that is:

$$\|\Gamma_{i+1} - \Gamma_i\| < \epsilon$$

if ϵ is sufficiently small and is converging toward zero, then the confidence in Γ_n with $n > i$ will be high. The trace and Hankel norms will be of particular interest. Note: The Hankel norm represents the gain of the system (H_2 gain).

4.4 Eigensystem Realization compared to Balanced Order Reduction

The most remarkable improvement in identification schemes was the Eigensystem Realization Algorithm (ERA) proposed by Juang and Pappa (1985). The idea behind the algorithm is the realization algorithm of Kalman-Ho [2], but it utilizes the numerically robust approach of singular value decomposition. In this section it will be shown that ERA with its model reduction based on singular values is functionally equivalent to the Schur method of balanced order reduction presented in 1989 by Safonov *et al* [21].

The Schur method is based on the large singular values of the Hankel operator and its singular value decomposition. Singular value decomposition is defined

as follows (See Maciejowski [24]):

$$H = U\Sigma V^T \quad (4.4.1)$$

U = is the matrix of the left eigenvectors of HH^T . That is

$$HH^T = U\Sigma^2 U^T.$$

V^T = is the matrix of the right eigenvectors of $H^T H$. That is

$$H^T H = V\Sigma^2 V^T.$$

$\Sigma = \text{diag}[\sigma_1, \sigma_2, \dots, \sigma_k]$ where k equals the rank of H .

$$\sigma_i = \lambda^{1/2}(HH^T)$$

Safonov *et al* (1989) used singular value decomposition to develop an algorithm to perform order reduction without requiring balancing the system first. (Note: balancing transformations such as proposed by Moore (1981) can be extremely numerically unstable). The approach performed an eigenvalue decomposition of the matrix PQ . The matrices $V_{L,BIG}$ and $V_{R,BIG}$ composed of the right and left eigenvectors associated with the “big” eigenvalues are used to perform model reduction.

4.4.1 Eigensystem Realization Algorithm Construction compared to Schur method Order Reduction

The ERA approach assumes that the system response sampled is produced by a linear system's impulse response. First assume a single input multi-output (SIMO) system (A, B, C) . Working with this realization, the discrete system impulse response is described by:

$$Y(k) = CA^{k-1}B$$

If the response is considered a free-decay from an initial condition $x(0)$ the response will be as follows:

$$Y(k) = CA^{k-1}x(0)$$

From here forward, the free-decay case initial condition $x(0)$ will be equated with input matrix B .

Now consider $H(k)$ to be the Hankel operator time shifted by k time units.

$$H(k) = \begin{bmatrix} Y(k) & Y(k+1) & \dots & Y(k+n) & \dots \\ Y(k+1) & Y(k+2) & \dots & Y(k+n+1) & \dots \\ \vdots & \vdots & & \vdots & \dots \end{bmatrix}$$

It is easy to show that this matrix can be constructed by using the controllability and observability operators, Ψ_c and Ψ_o , (see equations (4.2.11) and (4.2.17)).

$$H(k) = \Psi_o A^k \Psi_c$$

It can be shown that the zero delayed Hankel operator $H(0)$ has a left-pseudo inverse:

$$H(0)^\# = (H(0)^T H(0))^{-1} H(0) \quad (4.4.2)$$

which satisfies the following condition:

$$\Psi_c H(0)^\# \Psi_o = I$$

I is the identity matrix of appropriate size. Now using the same notation as equation (4.4.1), the zero delayed Hankel operator has a singular value decomposition of:

$$H(0) = U \Sigma V^T \quad (4.4.3)$$

$$H(0)^\# = V \Sigma^{-1} U^T \quad (4.4.4)$$

Using equation (4.4.2), the realization (A, B, C) is constructed from the Hankel operator as follows (See Ref [13]).

$$Y(k+1) = E_p^T C A^k B E_m \quad (4.4.5)$$

$$= E_p^T H(k) E_m = E_p^T \Psi_o A^k \Psi_c E_m \quad (4.4.6)$$

$$= E_p^T \Psi_o \Psi_c H^\#(0) \Psi_o A^k \Psi_c H(0)^\# \Psi_o \Psi_c E_m \quad (4.4.7)$$

$$= E_p^T H(0) V (\Sigma^{-1} U^T \Psi_o A^k \Psi_c V \Sigma^{-1} U^T H(0) E_m) \quad (4.4.8)$$

$$= E_p^T H(0) V (\Sigma^{-1} U^T H(1) V)^k \Sigma^{-1} U H(0) E_m \quad (4.4.9)$$

$$= E_p^T U \Sigma^{(1/2)} (\Sigma^{(-1/2)} U^T H(1) V \Sigma^{(-1/2)})^k \Sigma^{(1/2)} V^T E_m \quad (4.4.10)$$

$E_p^T = [I_p, 0, 0, \dots]^T$ and $E_m^T = [1, 0, 0, \dots]^T$. A full order realization is constructed with $A = \Sigma^{-1} U^T H(1) V$, $B = \Sigma^{(1/2)} V^T E_m$, and $C = E_p^T U \Sigma^{(1/2)}$. A

realization that reduces order in a balanced sense will select only the “large” singular values of the Hankel operator in the construction. Letting $\Sigma_k = \text{diag}(\sigma_1, \dots, \sigma_k)$ representing the k^{th} largest singular values and using matrices U_k and V_k that select the first k columns of U and V , the construction becomes:

$$A = \Sigma_k^{(-1/2)} U_k^T H(1) V_k \Sigma_k^{(-1/2)}$$

$$B = \Sigma_k^{(1/2)} V_k^T E_m$$

$$C = E_p^T U_k \Sigma_k^{(1/2)}$$

4.5 Improvements to Eigensystem Realization using Minimum Model Error Estimation

While ERA/Balanced order reduction and optimal Hankel-norm model reduction schemes provide nice error bounds in the frequency domain, they do not provide any bounds or insight to what is happening in the time domain. These realization approaches are deterministic, exactly matching $2n$ impulse response samples with an n^{th} order system. An approach presented by Mook *et al* [4], [5] addresses time domain considerations. This section explains this technique and applies it in a stochastic sense. The technique coupled with a realization and truncation scheme (such as Balanced order or Optimal Hankel-norm model reduction) will produce results that model the system in the time domain with a desired error variance and provide improved error bounds in the frequency domain. The necessary background is presented first, and then followed by the

actual minimization scheme.

4.5.1 Minimization of the Objective function

Given a differential system that is modeled as:

$$\dot{x}(t) = f(x(t), t, u(t)) \quad (4.5.1)$$

with initial state $x(t_o)$ and a cost function $\phi(\cdot)$ associated with its final state $x(t_f)$. Assume a cost, $L(u(\cdot), x(\cdot), \cdot)$, is incurred for using a state driving input (note: The cost is a function of input, state and time). The integrated cost of this input will be $\int_{t_o}^{t_f} L(u(t), x(t), t)dt$. A cost function J is then constructed to sum all related costs. This cost function is dependent on the exogenous input $u(t)$ and is defined as:

$$\min_u J = \phi[x(t_f)] + \int_{t_o}^{t_f} L[x(\tau), u(\tau), \tau]d\tau$$

It was shown by Pontryagin that this system can be optimally driven from an initial state to a final state [17]. Pontryagin's optimization principle showed that by constructing the co-state $p(t)$ defined by:

$$\dot{p}(t) = -\frac{\partial f^T}{\partial x}p(t) - \frac{\partial L^T}{\partial x} \quad (4.5.2)$$

with the boundary conditions:

$$p(t_f) = -\frac{\partial \phi^T}{\partial x}|_{x(t_f), t_f}$$

$$x(t_o) \text{ specified}$$

the optimal input can be calculated to drive $x(t_o) \rightarrow x(t_f)$ such that J is minimized. The optimizing input $u(\cdot)$ satisfies

$$\frac{\partial L[x(t), u(t), t]^T}{\partial u} = -\frac{\partial f(x(t), u(t), t)^T}{\partial u} \lambda \quad (4.5.3)$$

Using Pontryagin's optimization principle as our motivation, a system with output $\hat{y}(t)$ is used to optimally model the true outputs $y(t)$. An alternative cost function must be constructed to perform an optimization that accounts for the model errors at each time sample. The cost function to be minimized is constructed as follows:

$$\min_u J = \sum_{k=1}^M (y_k - \hat{y}_k)^T R_k^{-1} (y_k - \hat{y}_k) + \int_{t_o}^{t_f} u^T(\tau) W u(\tau) d\tau \quad (4.5.4)$$

$y_k = t_k$ sample of the true free-decay

$\hat{y}_k = t_k$ output of the modeling system, where

$$\hat{y}(\cdot) = g(x(\cdot), u(\cdot), (\cdot))$$

R_k = Noise covariance matrix at time instant k

$u(t)$ = input to system, the independent variable of optimization

W = Weighting function applied to inputs

This minimization of this cost function has two goals. The first is to minimize the weighted squared difference between the model estimated output, the true

system output, and each sample instant. The weighting function R_k is the noise covariance of the true system. Normally, this covariance is considered to be constant, however, it may vary with time. Varying the noise covariance matrix is very useful when the magnitude of the noise varies. (The noise covariance variation feature will be utilized in the analysis). The second goal is to minimize the weighted square of the exogenous input $u(t)$. This weighting function may be varied as well. While there is no advantage in varying its value over time, its magnitude is important in our experiment.

These two goals are competing within the minimization process. The optimization result depends on the importance given the respective weighting factors. For example, if the input weighting factor W is kept small, then the optimization will calculate an input that will cause the system model's output to near exactly track the true output at each sample instant t_k . If the input weighting factor is large, then the optimization will calculate an optimal input that contributes very little change to the modeled system's output.

Given this background, an improved approach is now outlined (Ref [5]):

1. Optimally calculate an input $u(t)$ so that the error covariance matrix is approximately equal to the true noise covariance matrix as follows (Ref [4]):

$$R_{error}^M(0) = \frac{1}{M} \sum_{k=1}^M (y_k - \hat{y}_k)^T (y_k - \hat{y}_k) \approx R_{noise} \quad (4.5.5)$$

2. Calculate the modeled output \hat{y}_k using the optimizing input $u(t)$.

3. Calculate a realization using the modeling output \hat{y}_k instead of the true measurements y_k .
4. Calculate the error bounds of this realization.

4.5.2 Optimization Problem formulation

The calculation of the optimizing input $u(\cdot)$ will require solving differential equations with boundary values for the states and the co-states. Equation (4.5.4) will be re written as:

$$\min_u J = \sum_{i=1}^M K_i(x(t_i), t_i) + \int_{t_o}^{t_f} u^T(\tau) W u(\tau) d\tau \quad (4.5.6)$$

The optimized co-states must include jumps discontinuities to account for minimizing the cost of the error at each measurement (Ref [4] and [12]). This discontinuity results from the summation term in equation (4.5.6) and requires that the co-states be adjusted at each output sample. Thus, if at time t_j a sample is taken, the co-states are adjusted by the derivative of the summation.

$$\lambda(t_j^+) = \lambda(t_j^-) - \frac{\partial f^T}{\partial x} K_j|_{x(t_j), t_j} \quad (4.5.7)$$

For the experiment under consideration, the modeling system will be chosen to be linear and described by equations (4.2.1) and (4.2.2). Using this assumption, equations (4.5.1) through (4.5.7) take on a much simpler form.

$$\dot{\lambda} = -A^T \lambda \quad (4.5.8)$$

$$2W^T u(t) = -B^T \lambda \quad (4.5.9)$$

$$\lambda(t_j^+) = \lambda(t_j^-) - 2C^T R_k^{-1}(y(t_k) - Cx(t_k)) \quad (4.5.10)$$

Note: It can be shown that all optimizing inputs $u(\cdot)$ are in range of B^T .

Mook [6] suggested a problem formulation of the problem so that it would lend itself to a linear algebra solution. This approach takes the n internal states and the n co-states and combines the two parts into a $2n$ order system. This new system is a first order differential problem with initial and final boundary conditions. The $2n$ system will be described as:

$$\dot{z}(t) = \tilde{A}z \quad (4.5.11)$$

where: $z(t) = [x_1(t), x_2(t), \dots, x_n(t), p_1(t), p_2(t), \dots, p_n(t)]^T$

The $2n \times 2n$ matrix \tilde{A} is constructed from the original linear differential equations.

$$\tilde{A} = \begin{bmatrix} A & -\frac{1}{2}B(W^T)^{-1}B^T \\ 0 & -A^T \end{bmatrix} \quad (4.5.12)$$

The differential equation (4.5.11) satisfies boundary values at t_o and t_f . The boundary conditions for the co-states are assumed to be zero at the beginning and the end, $p(t_o) = p(t_f) = 0$. This assumption is reasonable since there is no information about the internal states \underline{x} . [Note: If the free-decay assumed to be due to an initial condition, then the initial of $\underline{x}(t_o) = B$ may be assumed.] Using the assumption on co-state boundaries, the boundary value equation is constructed:

$$\beta = B_o z(t_o) + B_f z(t_f) \quad (4.5.13)$$

where $\beta = [p_1(t_o), p_2(t_o), \dots, p_n(t_o), p_1(t_f), p_2(t_f), \dots, p_n(t_f)]^T = [\underline{0}^T, \underline{0}^T]^T$ and

$$B_o = \begin{bmatrix} 0 & I \\ 0 & 0 \end{bmatrix}$$

$$B_f = \begin{bmatrix} 0 & 0 \\ 0 & I \end{bmatrix}$$

where all submatrices are dimension $n \times n$.

Finally, the jump discontinuities for the $2n$ system are expressed as:

$$z(t_k^+) = D_{t_k} z(t_k^-) + Y_{t_k} \quad (4.5.14)$$

where y_k is the k^{th} sample of the true system and D_{t_k} and Y_{t_k} are defined as:

$$D_{t_k} = \begin{bmatrix} I & 0 \\ -2C^T R_k^{-1} C & I \end{bmatrix}$$

$$Y_{t_k} = \begin{bmatrix} 0 \\ 2C^T R_k^{-1} \end{bmatrix}$$

4.5.3 Solving the Two-point boundary value problem by Multiple Shooting

One approach to solving the two-point boundary value problem (TPBVP) is the approach of shooting, That is, guess at the form of the solution and formulate the problem so as to solve the solution.

$$y(t) = v(t) + V(t)c$$

such that the boundary condition equation (4.5.13) is satisfied:

$$B_o[v(t_o) + V(t_o)c] + B_f[v(t_f) + V(t_f)c] = \beta \quad (4.5.15)$$

where:

1. c is the vector of coefficients for the time interval.
2. $v(t)$ is a particular solution $2n$ vector. The particular solution will be assumed to have zero initial condition $v(t_o) = 0$.
3. $V(t)$ is a solution $2n \times 2n$ matrix. The solution matrix will be assumed to have zero initial condition $V(t_o) = I$.

Thus using the state space representation of equation (4.5.11), the solution has a simplified form:

$$y(t_f) = \exp(\tilde{A}(t_f - t_o))c$$

Letting $\tilde{A}_{t_f-t_o} = \exp(\tilde{A}(t_f - t_o))$ and using the initial conditions for $v(t)$ and $V(t)$ the solution of equation (4.5.15) can be expressed as:

$$c = [B_o + B_f\tilde{A}_{t_f-t_o}]^{-1}\beta \quad (4.5.16)$$

The solution to c will exist if the inverse to $[B_o + B_f\tilde{A}_{t_f-t_o}]^{-1}$ exists. Mook [6] showed that this is a necessary and sufficient condition to solve the simple shooting problem. However, if the differential equation is stiff, then the solution may end up numerically unstable [23].

The problem of stiff differential equations can be solved by breaking the time interval into subintervals where the boundary conditions between adjacent subintervals are consistent. If m subintervals are created, then there will be $m + 1$ simultaneous equations in the form of equation (4.5.16) to solve in order to get the coefficients for each subinterval. This technique is called multiple shooting.

Multiple jump discontinuities are easily incorporated into the process. Assuming measurements taken at time instants t_k with $k \in \{1, \dots, M\}$, then during any shooting time interval equation (4.5.14) becomes:

$$y(t_{k+1}^+) = D_{t_{k+1}} \tilde{A}_{t_k - t_{k-1}} y(t_k^+) + Y_{t_{k+1}}$$

where t_k, t_{k+1} are within shooting interval.

Thus with this formulation, the solution to the TPBVP becomes one of linear algebra to solve for the coefficients of each subinterval.

4.6 Model Identification using Least-Squares model fitting

Previous sections have presented approaches for realization of a system assuming that noisy samples of the impulse response are given. In this section an alternate identification scheme is proposed given the same assumptions. The difference between this algorithm and the previous algorithms is that the identification will be done entirely in a stochastic sense. This identification scheme constructs a realization that minimizes the norm between the modeled system's impulse

response and the true measurements. The advantage of a stochastic based realization will occur when the number of measurements becomes relatively high.

The realization schemes such as ERA are deterministic and exactly duplicate the first $2n$ samples of a system with a n^{th} order system. While this may be acceptable for small values of n , computationally, it becomes weak as n becomes large. Additionally, the desired error bounds become less significant as the number of modes modeled increases due to the effects of noise (See Section on Infinite Dimensional Systems). This stochastic approach will use the least-squares approach. [Note: Attempts to use similar techniques, such as instrumental variables, did not provide any improvement and were more likely to produce erroneous overdetermined systems [1]].

4.6.1 Autoregressive Models

A linear dynamic discrete system can be modeled as process:

$$A(q)y(n) = B(q)u(n) + C(q)e(n)$$

where:

1. q is the delay operator, identical to z^{-1} in the z-transform.
2. $u(n)$ is the system input and $e(n)$ is unmeasurable noise input to the system.
3. $A(q) = [I + A_1q^{-1} + A_2q^{-2} + \dots + A_{n_a}q^{-n_a}]$

$$4. B(q) = [I + B_1q^{-1} + B_2q^{-2} + \dots + B_{n_b}q^{-n_b}]$$

$$5. C(q) = [I + C_1q^{-1} + C_2q^{-2} + \dots + C_{n_c}q^{-n_c}]$$

6. (n_a, n_b, n_c) are the orders of the dynamics of the different parts of the model.

The transfer function of this system written in matrix fraction description is:

$$y(n) = A(q)^{-1}B(q)u(n) + A(q)^{-1}C(q)e(n)$$

For the LACE experiment, white noise is assumed. This causes $C(q)$ to be unity, and the system reduces to the standard ARX (autoregressive-exogenous input) format. Also assuming the system is in free decay, $u(n) = 0$, the system becomes an autoregressive model. The one step ahead predictor of $y(n)$ is easily calculated to be (Ref [20]):

$$\hat{y}(n|\theta) = \varphi^T(n)\theta$$

where θ is the matrix of coefficients in $A(q)$ and $\varphi(k)$ is a column vector of system samples:

$$\varphi(k) = [-y(k), -y(k-1), \dots, -y(k-n_a)]^T$$

$$\theta = [A_1, A_2, \dots, A_{n_a}]^T$$

The error associated with each estimate $\hat{y}(n)$ is then the innovation $e(n)$ (Ref [20]):

$$e(n) = y(n) - \varphi^T(n)\theta$$

4.6.2 Autoregressive model performance

Letting $Z^N = \{y(n)|n \in \{1, \dots, N\}\}$, the autoregressive approach will injectively map the data set Z^N to the space of linear model of desired dimension.

$$Z^N \mapsto \theta$$

The goal of the parameter estimation will be to minimize the value of a given cost. The cost function V_N associated with a system sampled N times is defined to be:

$$V_N(\theta, Z^N) = \frac{1}{N} \sum_{k=1}^N l(e(k, \theta))$$

Using the least squares criteria the function $l(\cdot)$ is:

$$l(e(n)) = \frac{1}{2} e^T(n) \Lambda^{-1} e(n)$$

Where Λ is the weighting function on the error components. The optimizing set of coefficients is calculated by linear algebra as:

$$\hat{\theta}_{ls} = \left[\frac{1}{N} \sum_{k=1}^N \varphi(k) \Lambda^{-1} \varphi^T(k) \right]^{-1} \left[\frac{1}{N} \sum_{k=1}^N \varphi(k) \Lambda^{-1} y(k) \right] \quad (4.6.1)$$

Note: That by letting $\Lambda = I$, the first matrix in equation (4.6.1) becomes $\left[\frac{1}{N} \sum_{k=1}^N \varphi(k) \varphi^T(k) \right] = R_N(0)$ the N sample correlation matrix.

The LACE experiment the cost function $V_N(\theta, Z^N)$ is modified to account for knowledge of the noise level. This is accomplished by using a weighting function β_k . The cost function now becomes:

$$V_N(\theta, Z^N) = \frac{1}{N} \sum_{k=1}^N \beta_k \frac{1}{2} e^T(k) \Lambda^{-1} e(k)$$

and the optimizing least squares estimate becomes:

$$\hat{\theta}_{ls} = \left[\frac{1}{N} \sum_{k=1}^N \beta_k \varphi(k) \Lambda^{-1} \varphi^T(k) \right]^{-1} \left[\frac{1}{N} \sum_{k=1}^N \beta_k \varphi(k) \Lambda^{-1} y(k) \right] \quad (4.6.2)$$

This identification algorithm is an optimization over a set of models of order n_a . The model $\hat{\theta}_{ls}$ is then an element of the set of linear n_a models ($\theta_{ls} \in D_{n_a} \subset R_{n_a}$ for SISO systems). This optimization is guaranteed to converge to the true model θ_o as $N \rightarrow \infty$ provided two assumptions hold.

1. $e(n)$ is independent white noise.
2. $\theta_o \in D_{n_a}$ That is, the true model is indeed an element of the set of models that the optimization is done over.

Assumption (1) is reasonable, given the nature of the experiments samples (See chapter 1). Assumption (2) however is not guaranteed. The dynamics under interest are generated from a sampled frequency limited infinite dimension system. Thus, while a finite order model may model the true system relatively closely, it cannot be assumed that $\theta_o \in D_{n_a}$ when n_a is finite. Additionally, considering the potential nonlinear contributions, the case form assumption (2) becomes even weaker.

The approach chosen for this experiment is to use a sufficiently large value of n_a to model the sampled dynamics to within a desired error. Ljung [19] showed that $\hat{\theta}_{ls}$ will converge to the best possible solution in the model set D_{n_a} as the number of samples gets large. This is equivalent to minimizing the $l_2[0, N]$ norm of the errors. As the order gets large the two things occur.

1. The matrix $\left[\frac{1}{N} \sum_{k=1}^N \beta_k \varphi(k) \varphi^T(k) \right]$ will become poorly conditioned.
2. The highest orders of the system will primarily model the noise and non-linear behavior.

Since the goal is parametric identification, the least detectable higher order modes must be isolated from the strongly detectable modes. This is accomplished by converting the autoregressive model into a impulse response model and utilizing the balanced order or optimal Hankel norm order truncation schemes. The procedure is as follows:

Step 1: Calculate $\hat{\theta}_{l_s}$ of an order such that $V_N(\hat{\theta}_{l_s}, Z^N)$ is sufficiently small.

Step 2: Calculate transfer function $G(q) = A(q)^{-1}B(q)$ where $B(q)$ is chosen to create an impulse response model.

Step 3: Truncate system to dominant modes using balanced order reduction (or Optimal-Hankel Norm reduction).

4.7 Sampling Rate consideration

Computationally, longer data sets will provide better identification results. However, oversampling data does not provide any advantages. This becomes clear when analyzing the resulting parameter identification over the unit circle. An algorithm can only guarantee parametric identification performance up to a distance ϵ from the true parameters. As the data ensemble becomes large, a good

identification scheme's parameter results will converge to the true values, or at least sufficiently close. This is expressed as:

$$\|\theta_o - \hat{\theta}\| < \epsilon$$

$$\lim_{N \rightarrow \infty} \epsilon \rightarrow 0$$

Each parameter then is guaranteed to be close to its true value. Unfortunately, as modes are oversampled, the pole placement on the unit disc converges near the origin. When this occurs, there are two effects:

1. Modal frequency identification errors f_{error} become larger for a given ϵ and sampling rate ω_s . That is $f_{error} \approx \omega_s \epsilon$. While $\omega_s \rightarrow \text{Large}$, the identification convergence ($\epsilon_s \rightarrow \text{smaller}$) will not necessarily keep up.
2. Multiple modes are all converging to the origin, causing the ball B_ϵ of radius ϵ associated with each mode to overlap. (See Figure 4.2).

4 It can then be concluded that a judicious sample rate selection will separate the most observable modes from each other and decrease the error in estimated frequency. If many modes are present, filtering and frequency selection can be used to best isolate and identify the modes. In conclusion, the length of the data ensemble is limited by period of observation and by sample rate selection.

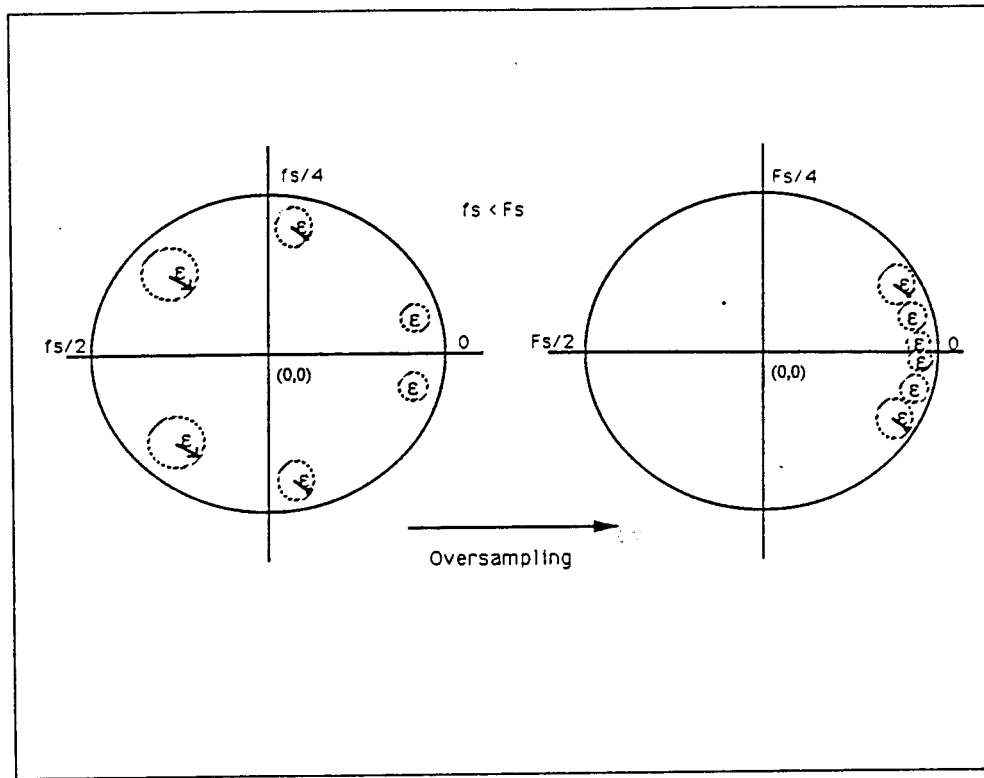


Figure 4.2: Convergence of modes on unit disc due to oversampling

4.8 Example of Identification Technique performance using LACE

PDE model response

An example of the performance of the various techniques is now demonstrated, in chapter 4 performance on actual data is discussed with all supporting rational.

The data used was generated from an impulse response of the linear PDE model of chapter 2. An internal damping factor of .01 was used (Note: This is less than 1 percent damping at frequencies below 5 Hz.). An assumed observation window of approximately 3 minutes chosen with a sampling rate of 5 Hz. The peak-to-peak excitation was set to approximately 10 mm/sec. White noise

with a covariance of 1 mm/sec was added to the impulse response. Additionally, bursts of noise with covariances of 2 mm/sec and 3 mm/sec respectively were added. The noise covariance information is assumed to be known a priori in the identification. Using this data, identification schemes were produced. The true modal frequencies were solved with $\alpha = 0$ as in chapter 2. In Figure 4.3 the Fourier transform shows that not all modes are detectable through the noise floor. This is due to the high noise level and the relative displacement of the boom tip for the modal frequencies (See chapter 2).

In Table 4.1 the results of the various identification schemes are compared. The ERA approaches used only 50 samples in the construction, more convergence could be expected by using more. Autoregressive technique used all the data.

true freq	ERA	ERA/MME	AR model truncation
0.0191	-	-	-
0.1298	0.1305	0.1305	0.1259
0.2581	-	-	-
0.3238	0.3275	0.3275	0.3174
0.7567	0.7679	0.7637	0.7642
0.8217	-	-	-
0.8639	0.8702	0.8669	0.8637
0.9428	-	-	-
1.7061	-	-	-
1.7223	-	-	-

Table 4.1: Modal Identification of noisy PDE impulse response

In Table 4.2 the L_∞ error bounds for the ERA approach and the stochastic

ERA/MME approach are shown. In Figures 4.4 and 4.5 the convergence of the singular values and the frequency responses of the approaches are shown. It is clear that the MME step will generate a nuclear hankel operator. The covariance chosen in the MME step was 2.3, which is approximately equal to the true average noise covariance.

ERA	ERA/MME
440.5	40.3

Table 4.2: L_∞ bound on model truncation

Note: This example exhibits the dependence on sampling rate. All techniques performed adequately for identifying the higher modes. However the lowest modes identification could be improved. A second iteration done with a decreased sampling rate will provide better identification of these modes.

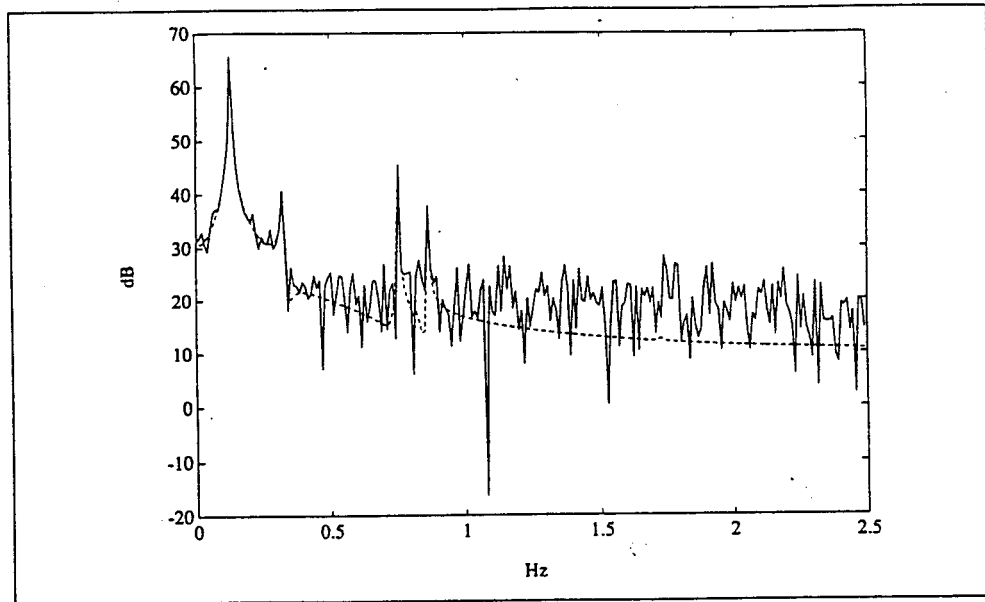


Figure 4.3: Spectrum Sampled Data overlaid with Noise-free Spectrum

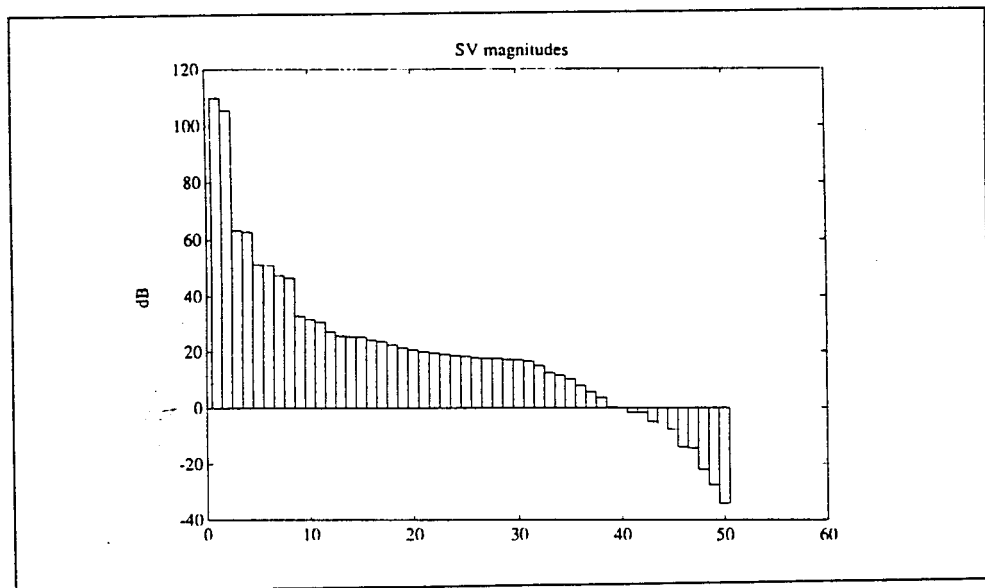


Figure 4.4: Singular values: ERA

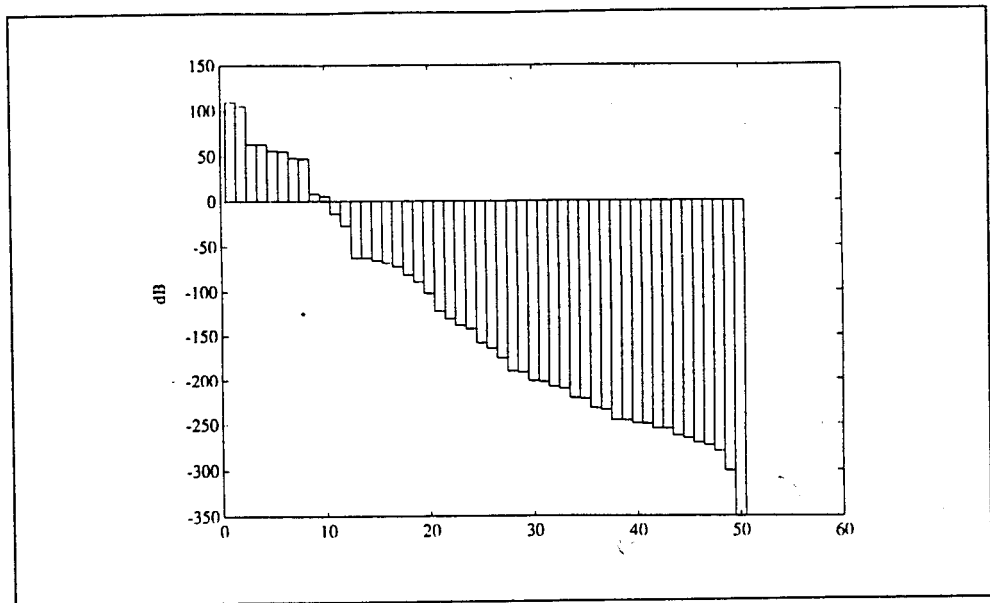


Figure 4.5: Singular values: MME

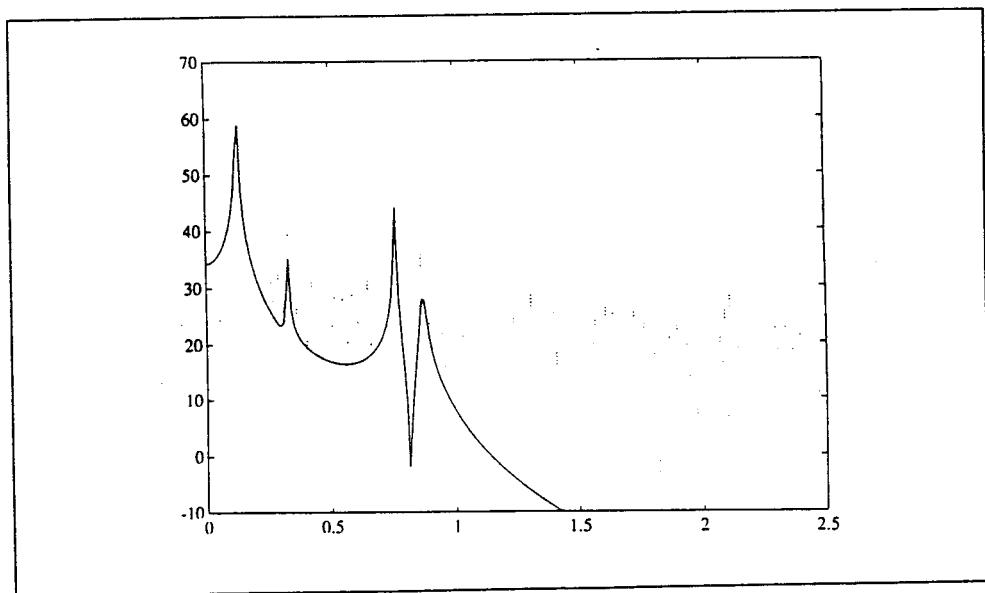


Figure 4.6: Frequency Response: ERA

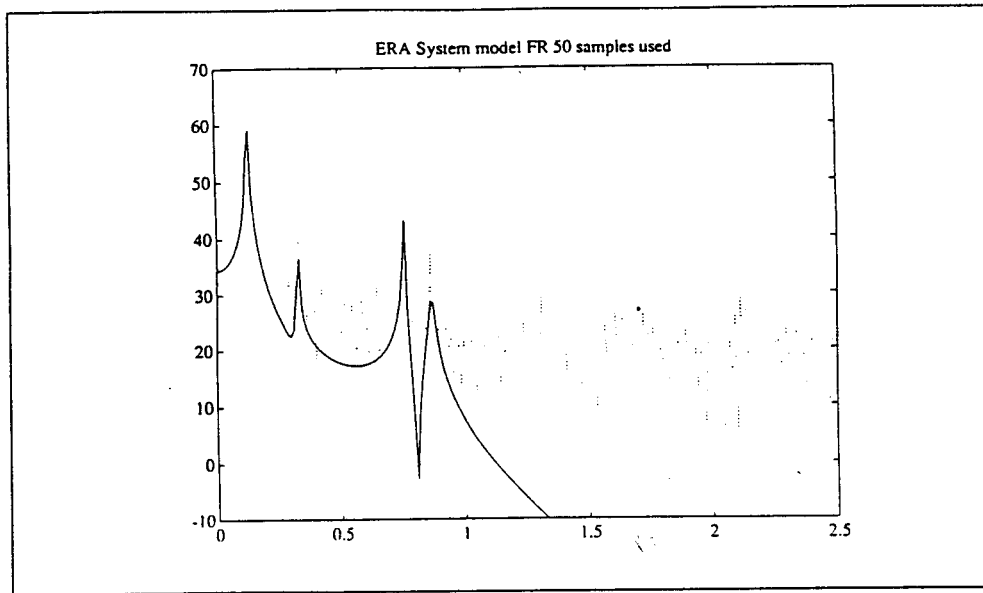


Figure 4.7: Frequency Response: ERA/MME

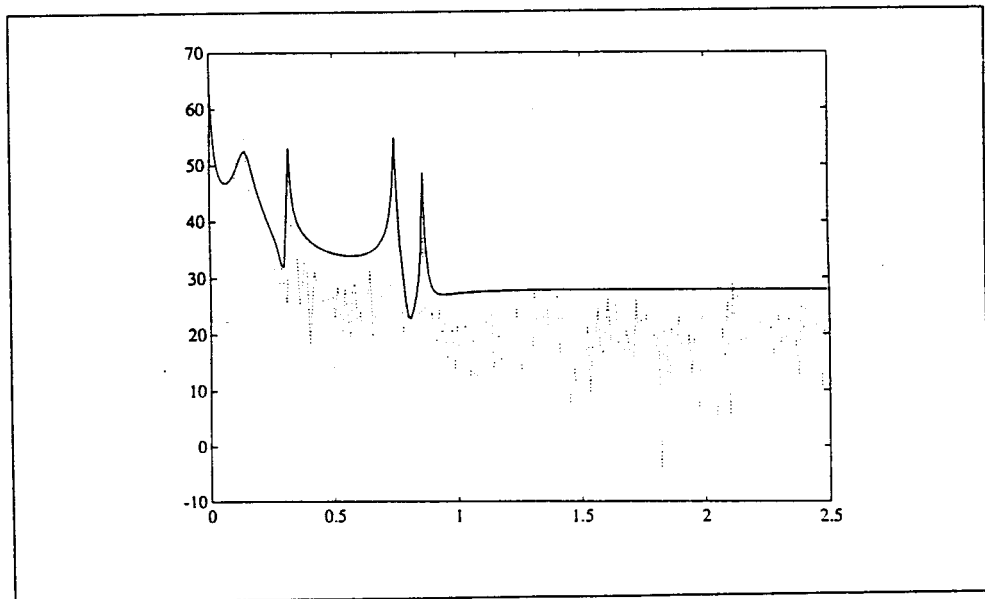


Figure 4.8: Frequency Response: AR

CHAPTER Five

Analysis of Experiment with LACE spacecraft

In early January 1990 the laser Doppler measurement experiment was performed. The test data was collected at Lincoln Laboratories and the data was then transferred back to the Naval Research Laboratories for analysis. The test coordinated the deployment and retraction of the lead boom with the observable window for laser illumination. Four observations were measured during the test period. Of these tests, only two windows observed the Doppler returns while the spacecraft experienced free-decay vibration. Currently, these two sample periods are the sole periods used in the structural identification process.

The first observation period is shown in Fig 5.1. This observation window captures the dynamic motion of the lead boom while the boom is being retracted and immediately following the end of retraction. The second half of this observation will be used in analysis. The complete period is informative in that it shows that the dynamic events can be detected reasonably well. At approximately 90 seconds into the observation, the dynamic motion due to the retraction of the boom ends. From that moment on, the detected motion of the boom is due to only the rigid body and vibration modes. Later the rigid

body motion is removed by calculating the predicted motion and subtracting this motion from the observed motion.

The second observation period is shown in Fig 5.2. This observation window was taken approximately 10 seconds after the retraction was completed. Since there is some delay in the measurement collection, the higher modes will have decayed more in this window. Fortunately, this observation window is much longer. The increased number of samples makes all the calculations more robust to the presence of noise. Additionally, the longer time period will allow a more meaningful analysis can be done when decimating in time. As mentioned in the previous chapter, decimating in time will help separate the lower frequency modes within the unit disc.

Hopefully, in the future the opportunity for more experiments will occur. As shown later in this chapter, the evaluation of these two limited observation windows provide very promising results.

5.1 Dynamic Body compensation

In addition to the vibrational motion, there is the rigid body motion of the spacecraft is due to the change in the ground observer's aspect angle. This angular change is shown in Figure 5.3. The apparent change has two effects on the observed Doppler shifted laser return.

1. The rigid body motion will be detected. Referring to Figure 2.6 of actual measured data, this mode roughly approximates a mode with a period 100 to 200 seconds or .01 Hz to .005 Hz. Thus the frequency separation between this apparent rigid body motion and the lowest vibrational mode of .019 Hz is very small. In order to detect the lowest mode, this apparent motion must be eliminated.
2. The observed damping factors of the detected modes will be affected by the position of the spacecraft in the sky. If the observation window is before the spacecraft comes overhead, the calculated damping factors will be smaller. If the modal frequency is small, the calculated damping factor could indeed become negative. Likewise, if the observation window is after the spacecraft goes overhead, the calculated damping factor will become larger than the true value. Figure 5.3 demonstrates this effect by showing the projected pitch velocity vectors onto the line-of-sight vector. In the figure, the velocity vector is always in the pitch direction with respect to the spacecraft and is kept at a constant level. Thus, the projection of the

velocity vector onto the LOS vector increases before passing overhead and decreases after passing overhead.

The effects of this apparent motion needs to be adjusted for. This is accomplished by calculating orbital position with respect to the observation site and calculating the apparent motion. The calculated rigid body motion was simply subtracted from the observed motion. Then the change in aspect angle was corrected for by dividing by the cosine of the angle between the LOS vector and the pitch plane.

5.2 Identification Analysis

The in-phase and quadrature data measured at Lincoln Laboratory was analyzed in order to calculate the relative motion of the spacecraft. The Fourier transform of the data was filtered such that the relative difference between the return of the lead retro-reflector and the bus retro-reflector would track the dynamic motion of the spacecraft.

The test data has Doppler shift measurements collected at a 62 Hz sample rate. This rate is significantly higher than the modes of interest. To filter out some of the noise present, groups of 5 samples are taken and the median value of the population is selected. This technique reduces the sample rate to 12.4 Hz, which is more than adequate for analysis. Reducing the sampling rate further will be done with filtering and decimation in time. Using a larger population and selecting the median will provide more noise rejection than averaging. This

is due to the small population used in the analysis. Averaging populations of 5 or 10 samples, is susceptible to noise components, thus the median is the most effective. Another technique is to choose the most likely Doppler shift. However, the population size is still too small for this.

5.2.1 Identification Results

Using this data, an initial analysis was performed. All the data was initially filtered to eliminate high noise components. The cutoff frequency was chosen to be .75 Hz. This number allows for decimation in time and provides margin for the higher modes. The data sets were then decimated in time into distinct data sets. Each of these data sets were then analyzed and statistically compared. (Note: The minimum model error results generated optimal data such the variance between the actual and simulated data was approximately 2.4 mm/sec. This corresponds to one bin in the discrete Fourier transform of the Doppler shifted laser return.) Table 5.1 lists information about each observation windows. Tables 5.2 through 5.5 details the results of this study. Figures 5.4 and 5.5 plot the detected frequencies and damping factors for all the data sets of both observation windows.

The results of this analysis are quite impressive. Given such short observation windows, the algorithms detected modes which correlate well with predictions. Of the first four vibration modes, three were detected on day 91010. The lowest mode is only detectable if the rigid body motion is removed from the data. One

of the eight data sets for day 91010 did not detect the lowest mode. Thus, an asterisk is used in Tables 5.4 and 5.5 associated with the lowest mode to designate that only 7 of the data sets was used in the statistics.

On day 91008, only two of the four were detected. The day 91008 observation window was only 25 seconds long and this window was too short to collect enough data on the lowest mode (modal period is ≈ 50 seconds).

Note, there is one moderately damped mode $\approx .52$ Hz which is detected on both days that the neither the PDE or FEM model predicted. This mode is probably not due to the boom elements because the damping is too high. Additionally, this vibration does not correlate with any yaw or roll mode predicted by analysis. While the explanation for this mode is yet unknown it is believed to be due to either unmodeled behavior within the boom canisters or vibrations that are due to the cantilevered retro-reflector plate. Since the retro-reflector center of mass is offset from the boom axis. A local vibration may exist at the boom tip due solely to the retro-reflector plate. If this is the case, the vibration would be due to a local elastic behavior in the boom. Such elastic behavior would tend to be nonlinear and will have higher damping.

The nonlinear vibration assumption is supported by the size of the damping factor for the .52 Hz mode. Its damping factor was between 5 and 11 percent. This level is significantly higher than the other modes. This difference may be attributed to the nonlinear behavior in either the boom canister or at the cantilevered retro-reflector plate.

The identified modes were within .005 to .01 Hz of the predicted modes depending on the identification technique compared. While this is impressive, the identification of the damping factors had a larger variance. Of the predicted modes that were identified, Tables 5.3 and 5.5 show that two of the three modes had damping of approximately one to two percent. This agrees well with experiments done on the ground. The damping factor for the lowest mode of .019 Hz, had a large variance associated with it. This variance is due to the fact that the period of observation was very short in comparison to the period of the mode. In the future, longer observation windows will provide enough information to get better damping calculations.

Finally, it should be noted that the autoregressive identification scheme did not perform as well as the ERA or ERA/MME techniques. This is because the observation windows were too short. As the windows get shorter, the autoregressive technique becomes an approximation to the ERA approach with only a modest amount of averaging. In the future, as longer data sets are sampled the autoregressive approach should perform better.

window	length sec.	no. samples
Day91008	24.5	310
Day91010	49.0	616

Table 5.1: Length of Data samples for Observation window

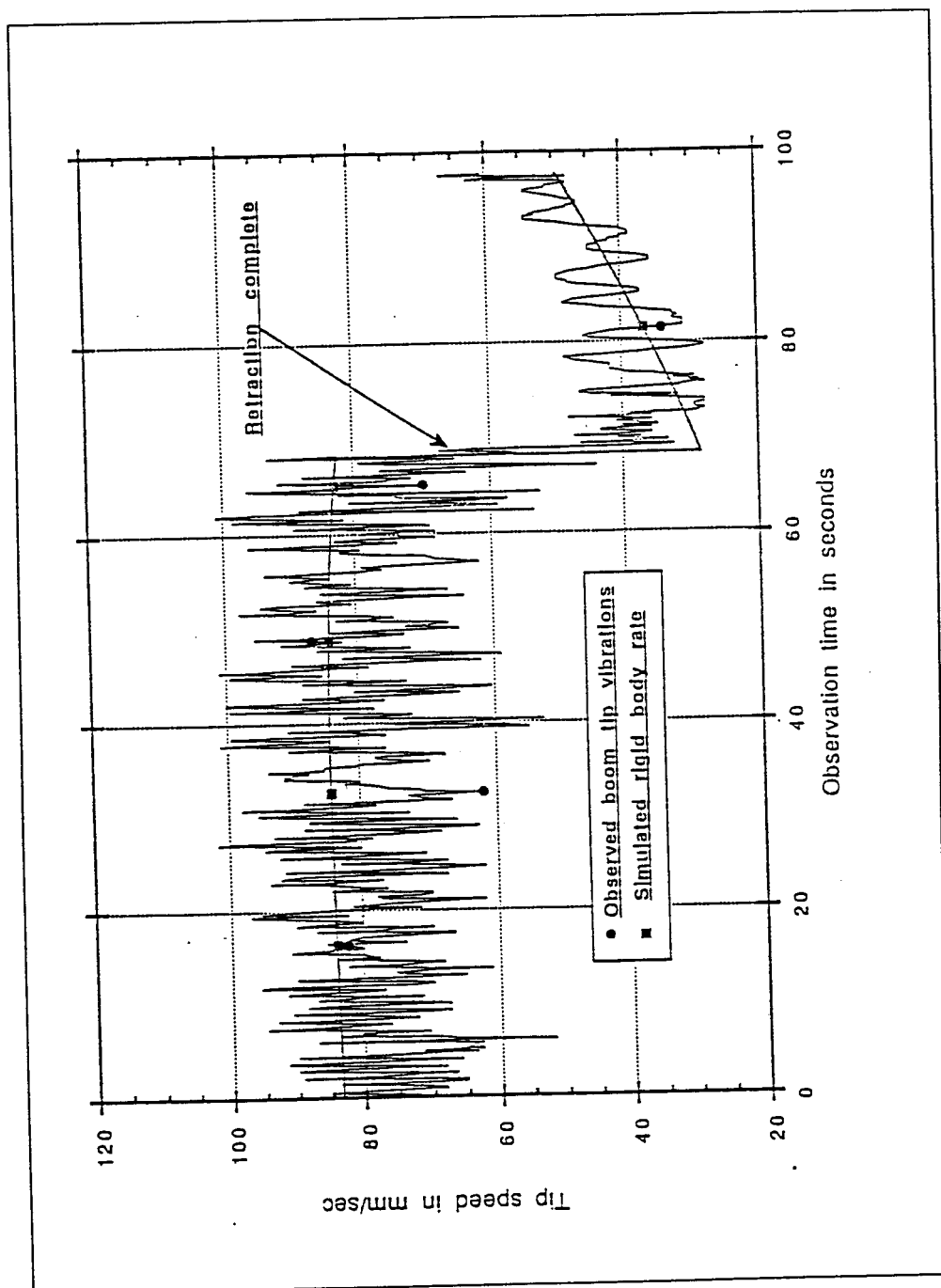


Figure 5.1: Measured Relative velocity Day91008

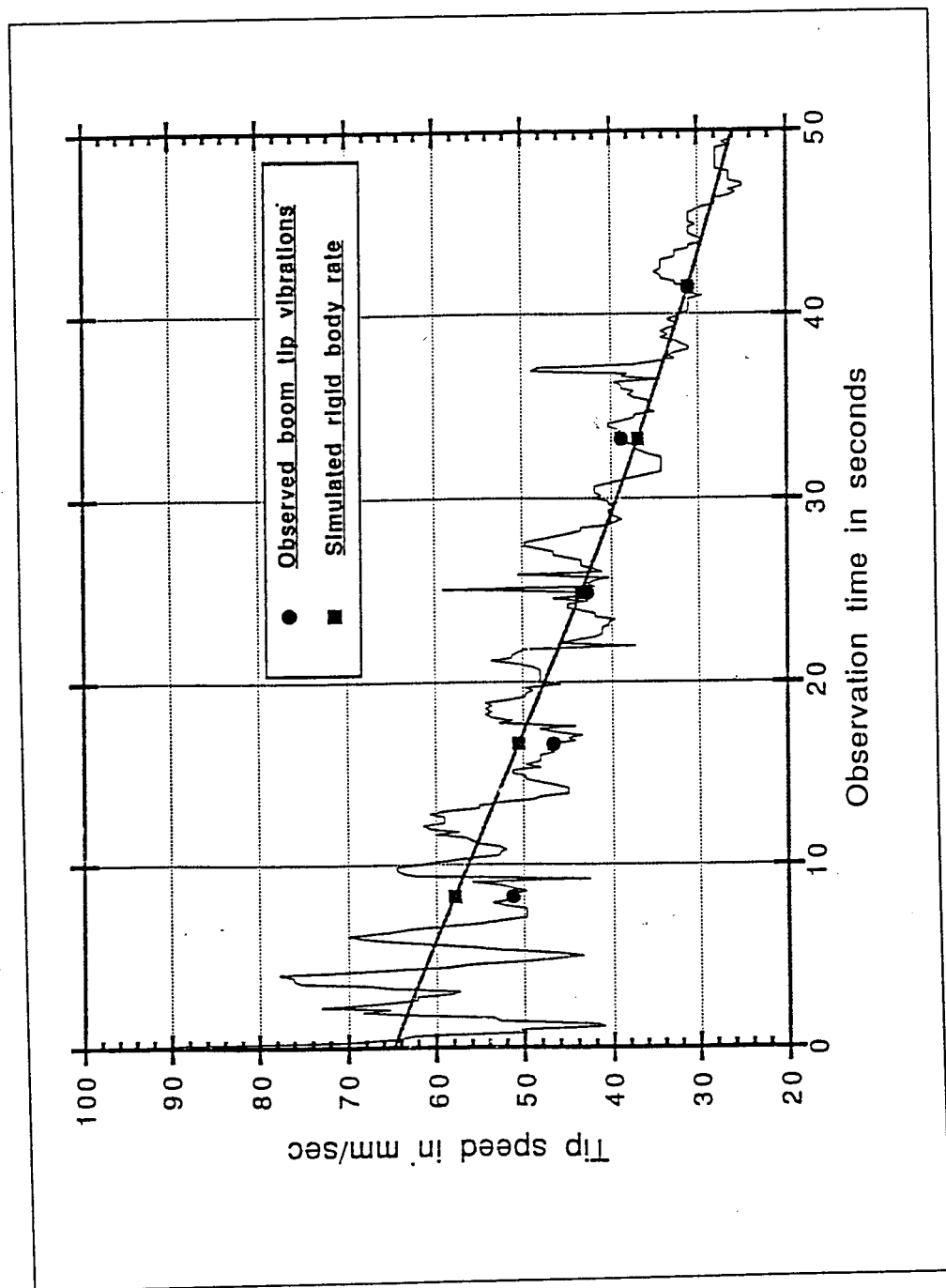


Figure 5.2: Measured Relative velocity Day91010

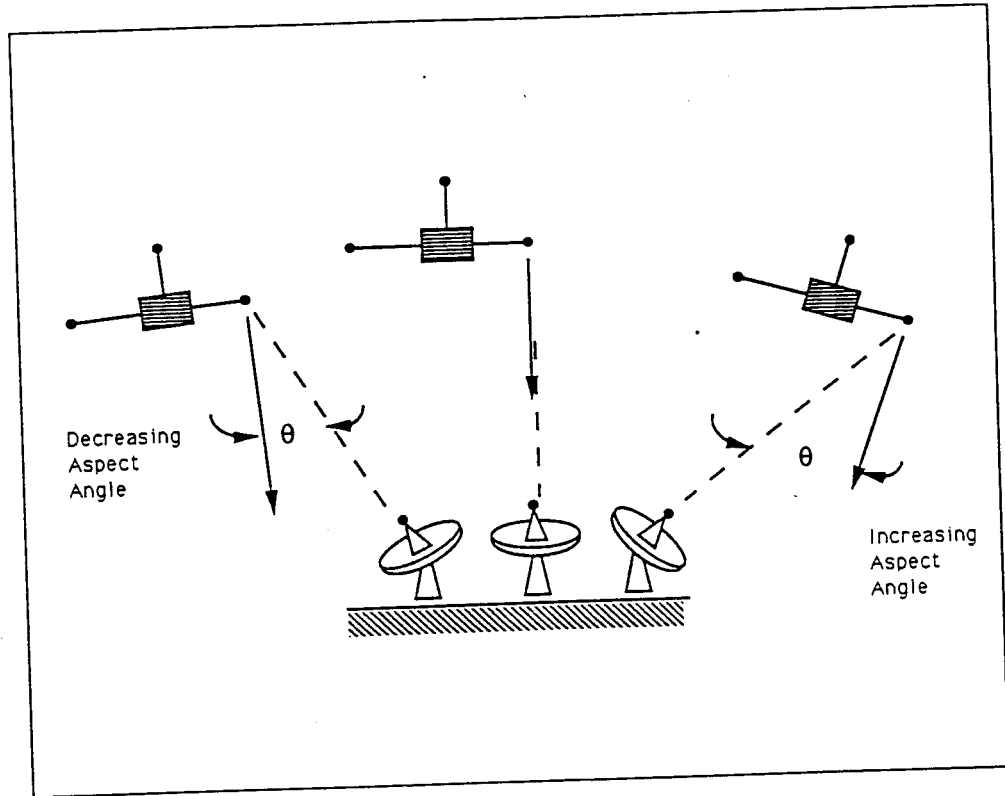


Figure 5.3: Effect of changing aspect angle on observed motion magnitude

Model Mode Hz.	ERA Hz.	std. dev. Hz.	ERA/MME Hz.	std. dev. Hz.	AR/model reduction Hz.
0.1298	0.1225	0.0005	0.1226	0.0005	0.1226
0.3238	0.3245	0.0003	0.3248	0.0006	0.3243
	0.5219	0.0025	0.5201	0.0030	0.5220

Table 5.2: Day91008 Identification Results: Modal Frequencies

Model Mode	ERA %	std. dev.	ERA/MME %	std. dev.	AR/model reduction %
0.1298	-0.1244	0.2489	-0.3518	0.3027	-0.0470
0.3238	1.4477	0.0410	1.1137	0.0473	1.1583
	4.8917	0.2984	4.5929	0.2631	4.2525

Table 5.3: Day91008 Identification Results: Damping Factors

Model Mode Hz.	ERA Hz.	std. dev. Hz.	ERA/MME Hz.	std. dev. Hz.	AR/model reduction Hz.
0.0191	0.0208*	0.0033*	0.0210 *	0.0020*	
0.1298	0.1244	0.0010	0.1245	0.0011	0.1226
0.3238	0.3312	0.0009	0.3320	0.0008	0.3243
	0.5115	0.0061	0.5120	0.0064	0.5220

Table 5.4: Day91010 Identification Results: Modal Frequencies

Model Mode	ERA %	std. dev.	ERA/MME %	std. dev.	AR/model reduction %
0.0191	1.8385*	1.8277*	1.3937 *	2.2607*	
0.1298	2.3233	0.5182	2.1029	0.3007	-0.0470
0.3238	2.1114	0.2312	2.0058	0.2971	1.1583
	10.4537	1.2157	10.7973	1.0233	4.2525

Table 5.5: Day91010 Identification Results: Damping Factors

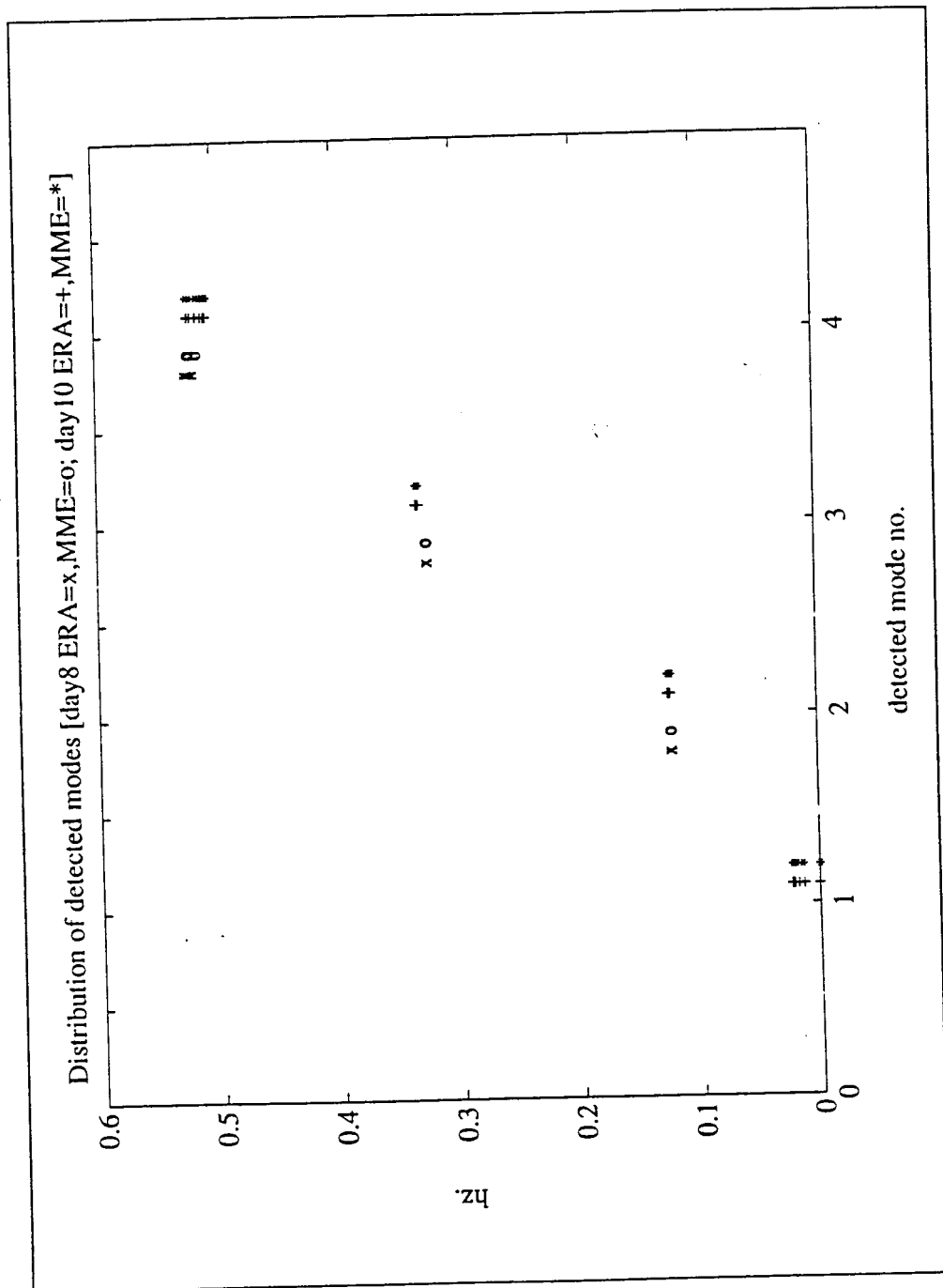


Figure 5.4: Detected Modal Frequencies for days 91008 and 91010

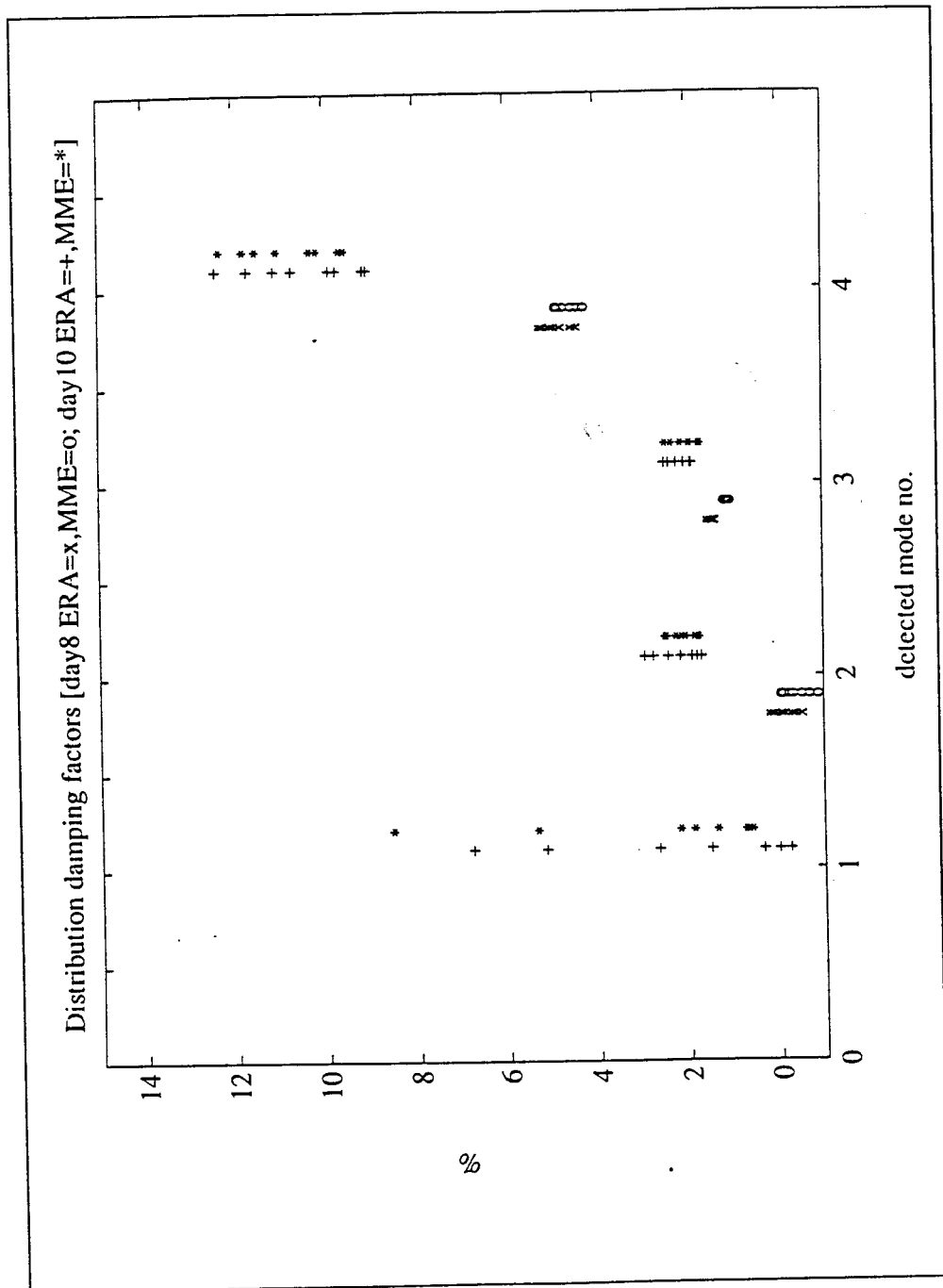


Figure 5.5: Detected Modal Damping Factors for days 91008 and 91010

5.2.2 The Linearity Assumption

The identification algorithms are based on a linear model assumption. While it can be assumed the minimum model estimation optimal input compensates for small nonlinear components, the extension to nonlinear cases is weak. Thus, the assumption of “near” linear behavior is important. A qualitative study of this is done by integrating the observed response, and then calculating the peak displacement on the spacecraft body.

The detected motion was filtered to isolate each modal component. This filtered signal was integrated to calculate peak boom tip displacement. The peak tip displacement was then divided by the modal frequency displacement ratios in Table 3.2. These approximate peak system displacements are shown in Tables 5.6 and 5.7. This table shows that the peak system displacements should be small and the linear assumption is valid. Additionally, considering the forcing function used (the deployment and retraction of the boom), the vibrations should be linear. (Note: No information on system displacement at .52 Hz exists).

mode hz	peak boom tip Displacement (mm)	Displacement Ratio	peak system Displacement (mm)
.1298	0.9	0.0063	≈ 150
.3238	1.7	0.0565	≈ 31
.5200	0.9		

Table 5.6: Peak System Vibration Displacements: Day91008

mode hz	peak boom tip Displacement (mm)	Displacement Ratio	peak system Displacement (mm)
.0190	.9	0.0242	≈ 36
.1298	1.0	0.0063	≈ 164
.3238	1.8	0.0565	≈ 32
.5200	.5		

Table 5.7: Peak System Vibration Displacements: Day91010

5.3 Convergence of the Hankel operator

As mentioned in the previous chapter, the identification algorithm assume a linear impulse response is provided. Given such a response and assuming nuclearity (see previous chapter), the Hankel operator constructed from the impulse response will have a bounded nuclear norm, Hankel and Frobenius norms. However, the condition of added noise may nullify these conditions. Thus, a test of these norms on the raw data for both tests was performed. A data sample rate of 3.1 Hz was used for each filtered data set on day 91010 and a data sample rate of 6.2 Hz was used for day 91008. Figures 5.6 through 5.17 plot the analysis results for each data set. It is clear that these norms do not appear to be converging. However, it must be noted that both Day91008 and Day91010 have limited sample periods and the conclusions drawn are based on limited information.

1. Figures 5.6 and 5.12 show the nuclear norm for progressively larger Hankel matrix operators.

2. Figures 5.7 and 5.13 show the Cauchy sequence of nuclear norms for progressively larger Hankel matrix operators. The sequence equals $\|\Gamma_{n+1}\|_N - \|\Gamma_n\|_N$.
3. Figures 5.8 and 5.14 show the Frobenius norm for progressively larger Hankel matrix operators.
4. Figures 5.9 and 5.15 show an upper bound on the Cauchy sequence of Frobenius norms. The upper bound on the sequence is $\|\Gamma_{n+1}\|_F - \|\Gamma_n\|_F$ (Triangle Inequality).
5. Figures 5.10 and 5.16 show the Hankel norm for progressively larger Hankel matrix operators.
6. Figures 5.11 and 5.17 show an upper bound on the Cauchy sequence of Hankel norms. The upper bound on the sequence is $\|\Gamma_{n+1}\|_H - \|\Gamma_n\|_H$ (Triangle Inequality).

These plots show that in spite of the noise elimination provided by taking the mean value over time slots and filtering, the constructed Hankel operator is not converging to a sufficiently small bound within the time period measured. This could be due to either the continued presence of noise or nonlinear behavior of the system. The latter of these two sources is more difficult to deal with, however as discussed in the previous section the linear assumption should be reasonable.

In figures 5.18 through 5.29 the same analysis was done on the minimum model error data (see previous chapter for MME description). As discussed in the previous chapter, this data is constructed optimally from a linear model such that the exogenous input is minimized. In this case the exogenous input can be considered to be nonlinear components entering into the system. These plots show that the nuclear and Frobenius norms are beginning to converge. By allowing the target covariance used in the optimization to increase, the norms will converge even faster. The target covariance used was 2.4 mm/sec as in the previous section.

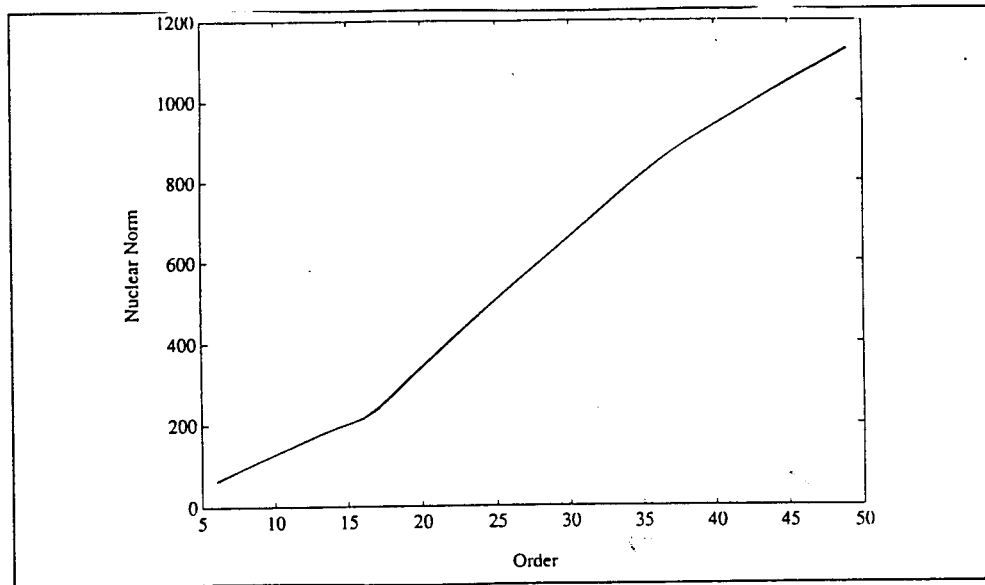


Figure 5.6: Nuclear Norm Truncated Hankel Operator Day91008

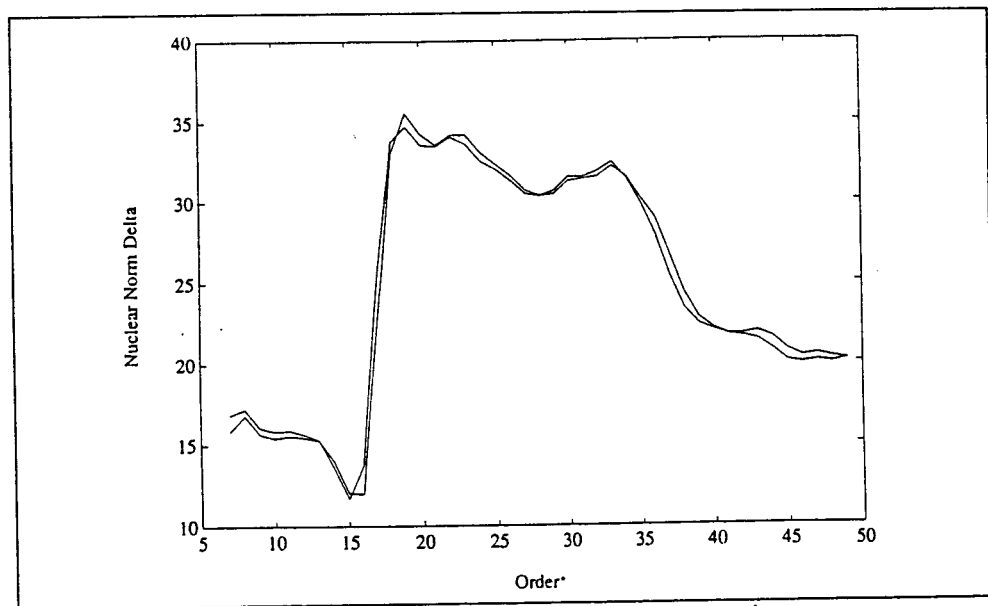


Figure 5.7: Cauchy Sequence of Nuclear Norms for Truncated Hankel Operator Day91008

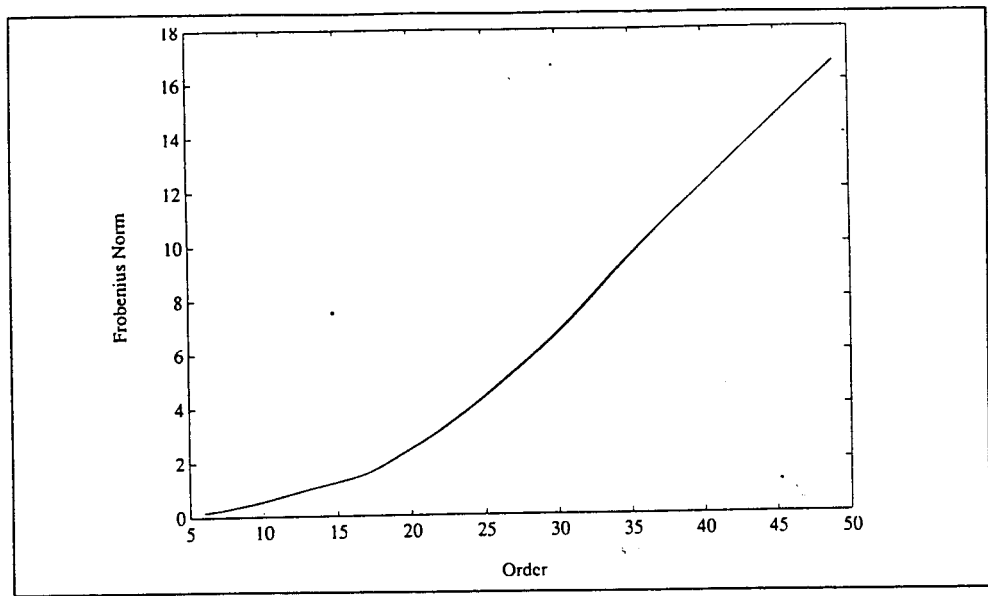


Figure 5.8: Frobenius Norm Truncated Hankel Operator Day91008

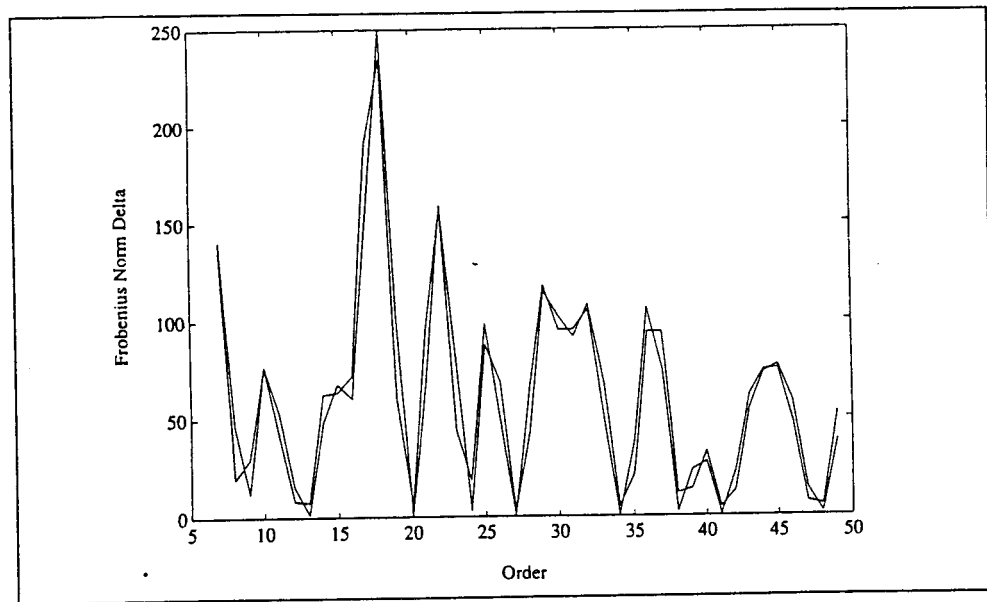


Figure 5.9: Upper Bound of Cauchy Sequence for Frobenius Norm of Truncated Hankel Operator Day91008

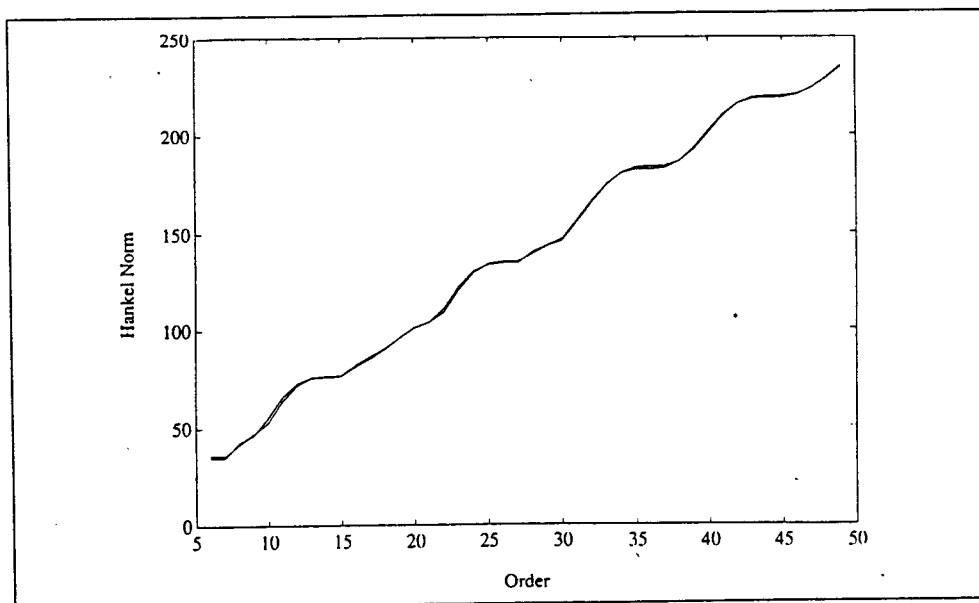


Figure 5.10: Hankel Norm Truncated Hankel Operator Day91008

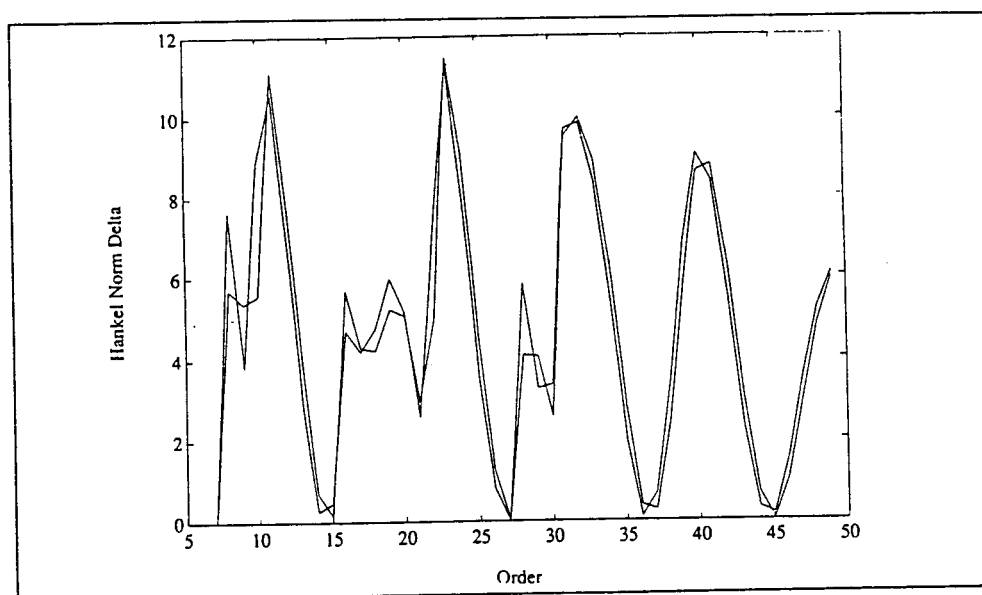


Figure 5.11: Upper Bound of Cauchy Sequence for Hankel Norm of Truncated Hankel Operator Day91008

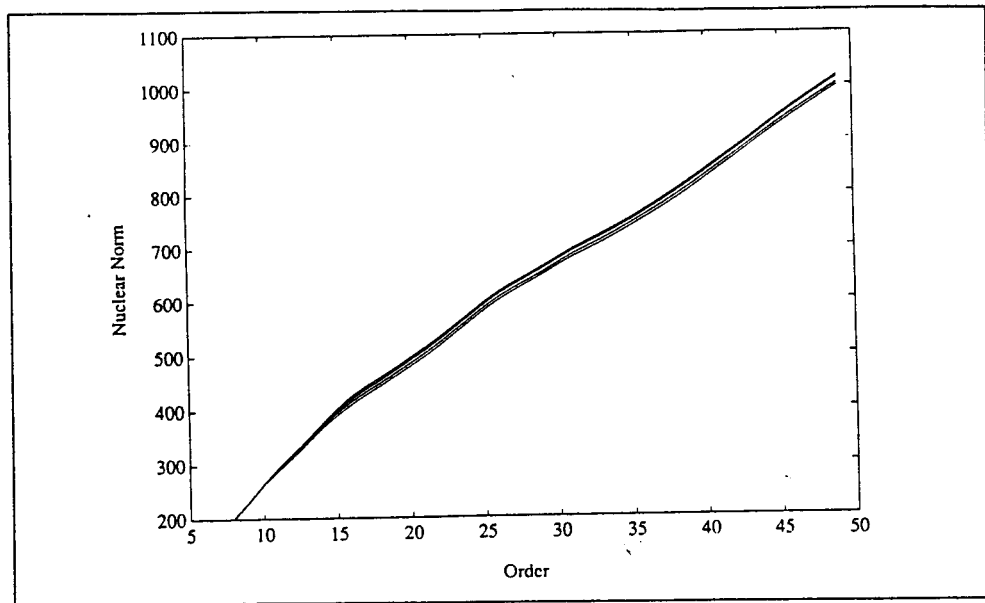


Figure 5.12: Nuclear Norm Truncated Hankel Operator Day91010

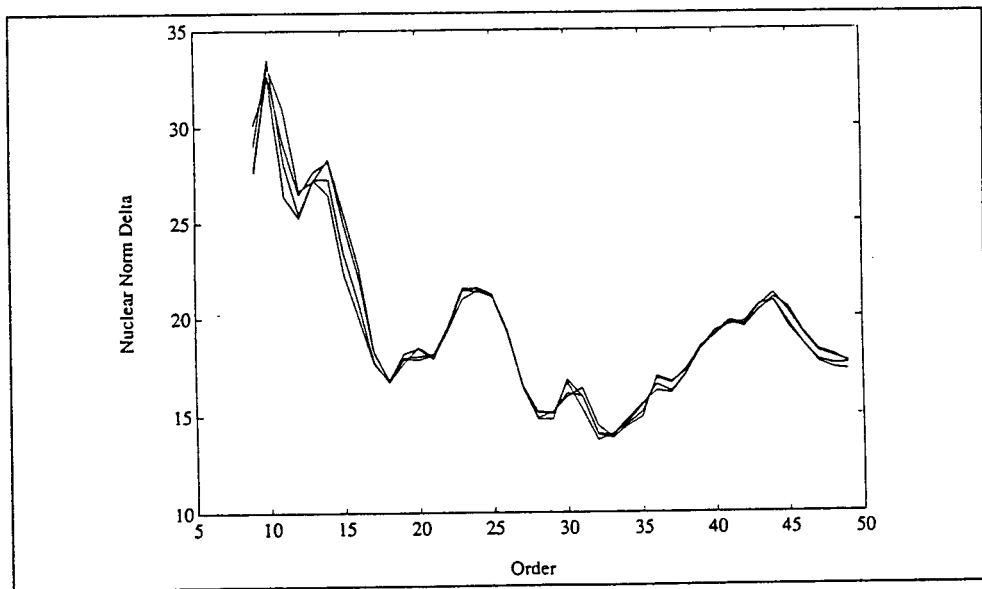


Figure 5.13: Cauchy Sequence of Nuclear Norms for Truncated Hankel Operator Day91010

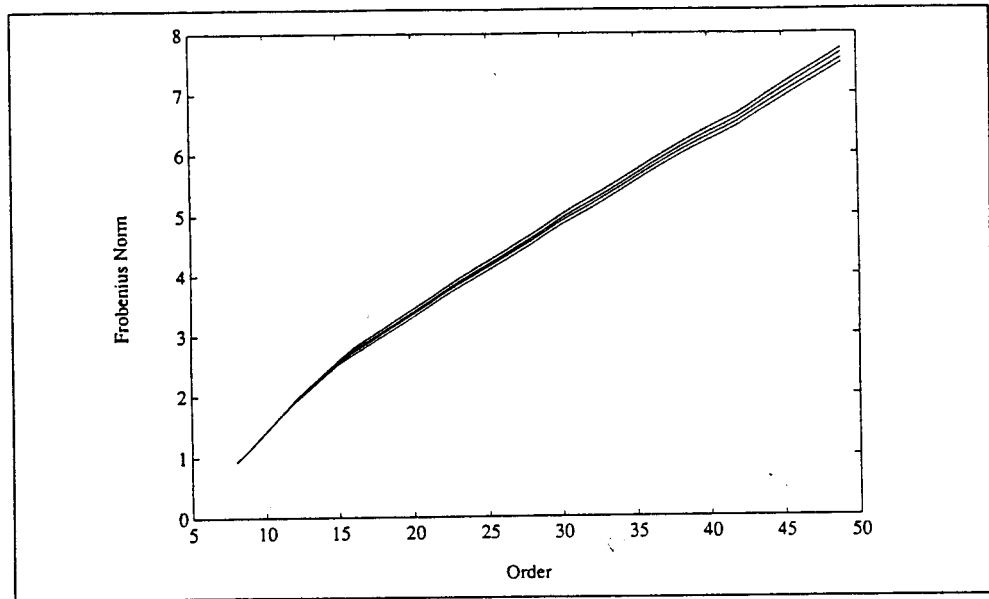


Figure 5.14: Frobenius Norm Truncated Hankel Operator Day91010

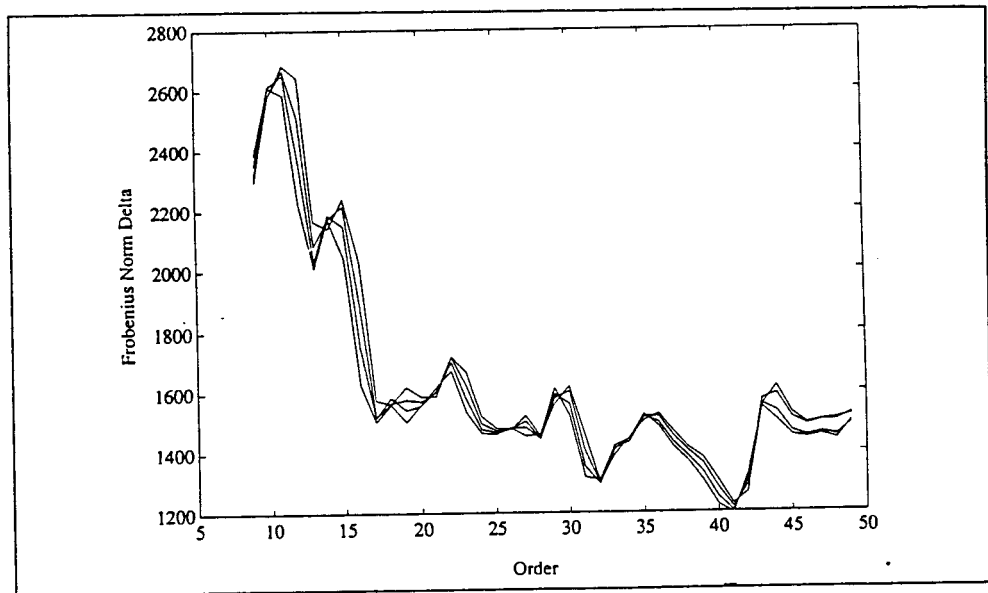


Figure 5.15: Upper Bound of Cauchy Sequence for Frobenius Norm of Truncated Hankel Operator Day91010

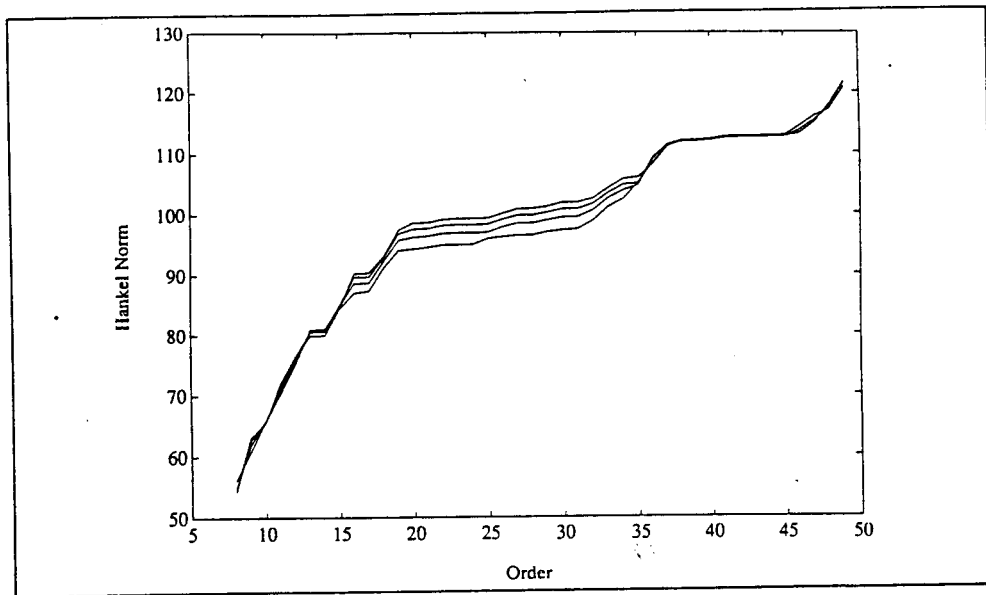


Figure 5.16: Hankel Norm Truncated Hankel Operator Day91010

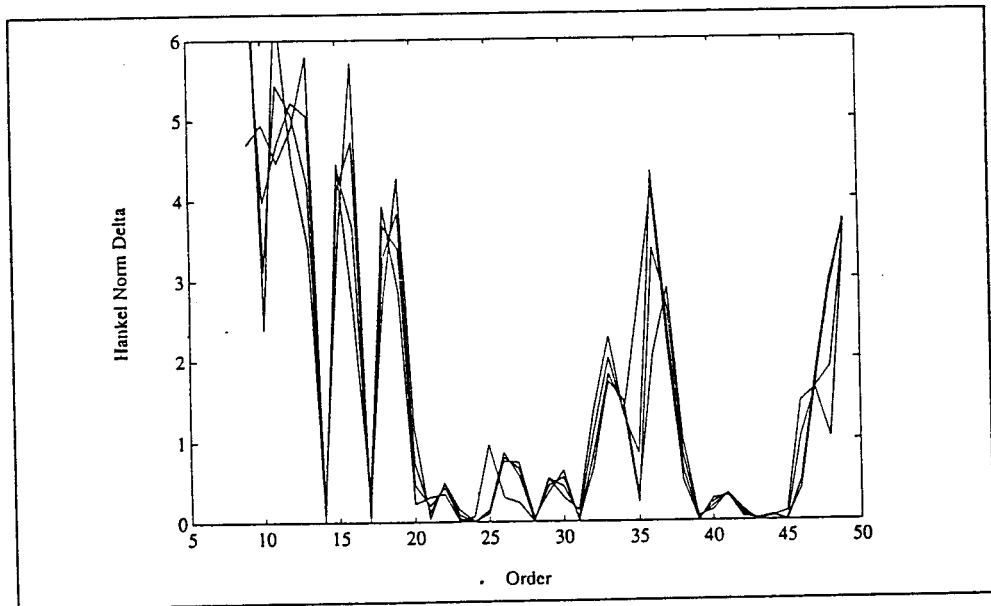


Figure 5.17: Upper Bound of Cauchy Sequence for Hankel Norm of Truncated Hankel Operator Day91010

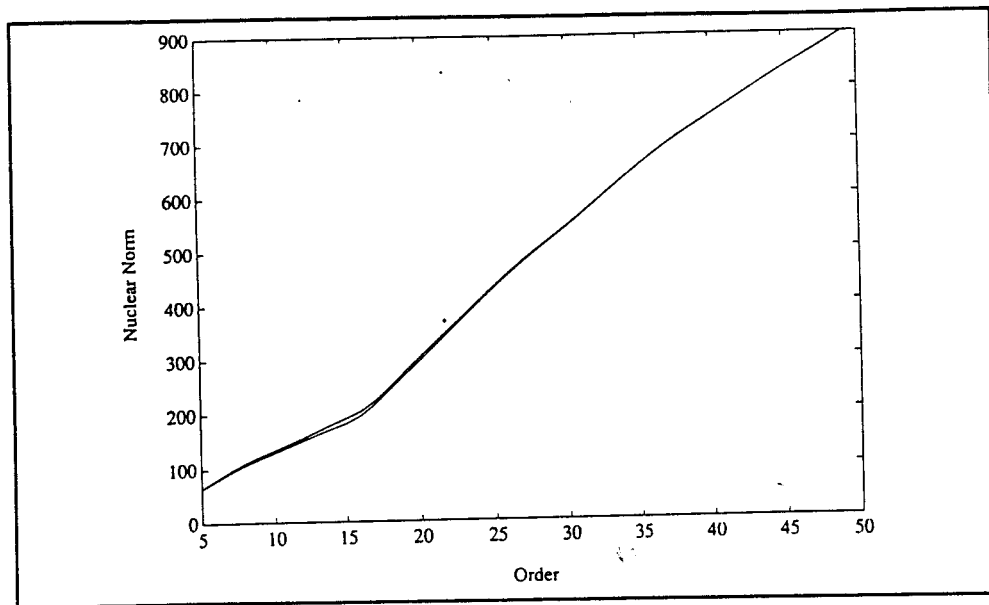


Figure 5.18: Nuclear Norm Truncated MME Hankel Operator Day91008

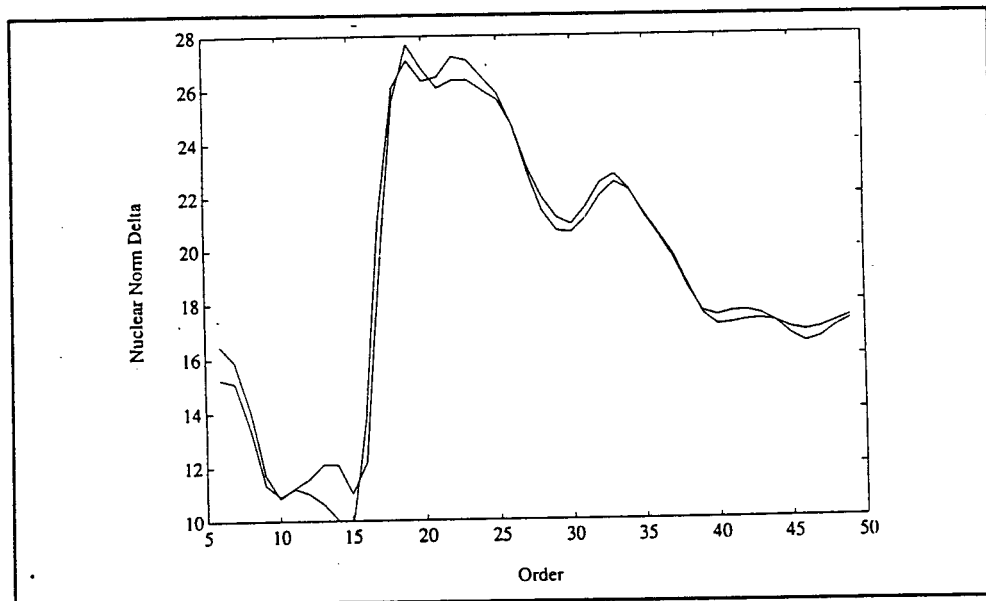


Figure 5.19: Cauchy Sequence of Nuclear Norms for Truncated MME Hankel Operator Day91008

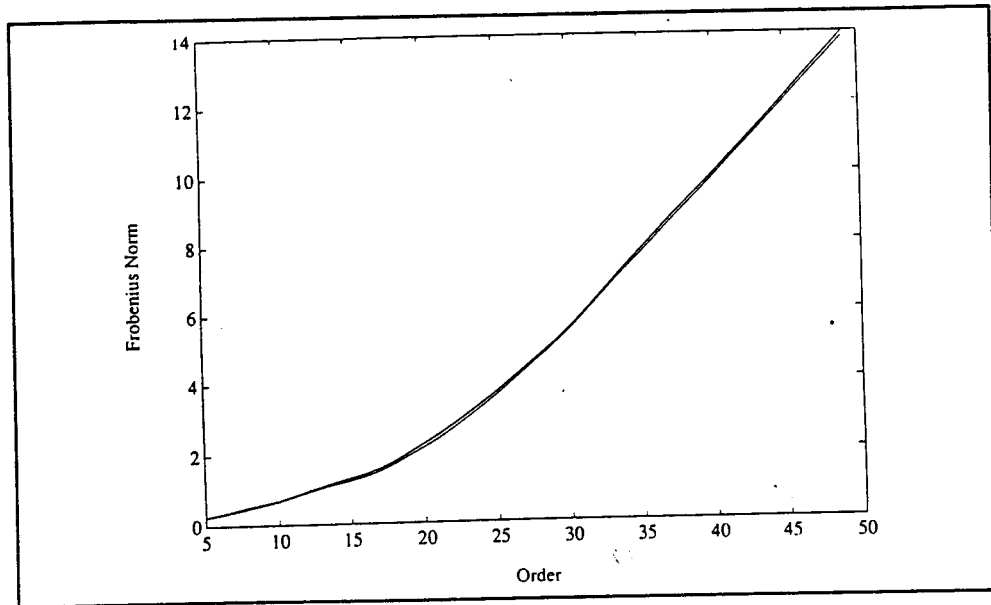


Figure 5.20: Frobenius Norm Truncated MME Hankel Operator Day91008

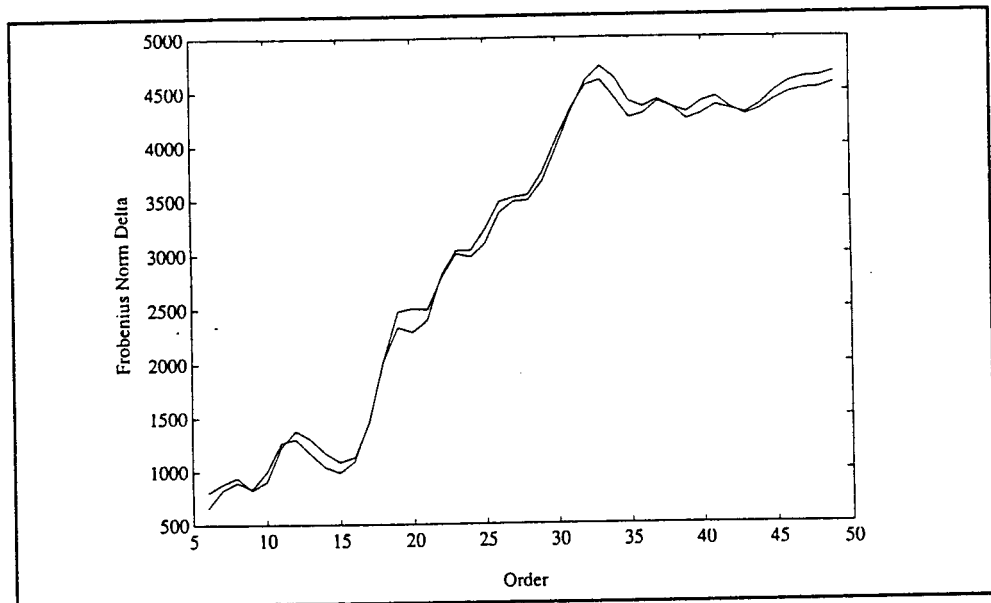


Figure 5.21: Upper Bound of Cauchy Sequence for Frobenius Norm of Truncated MME Hankel Operator Day91008

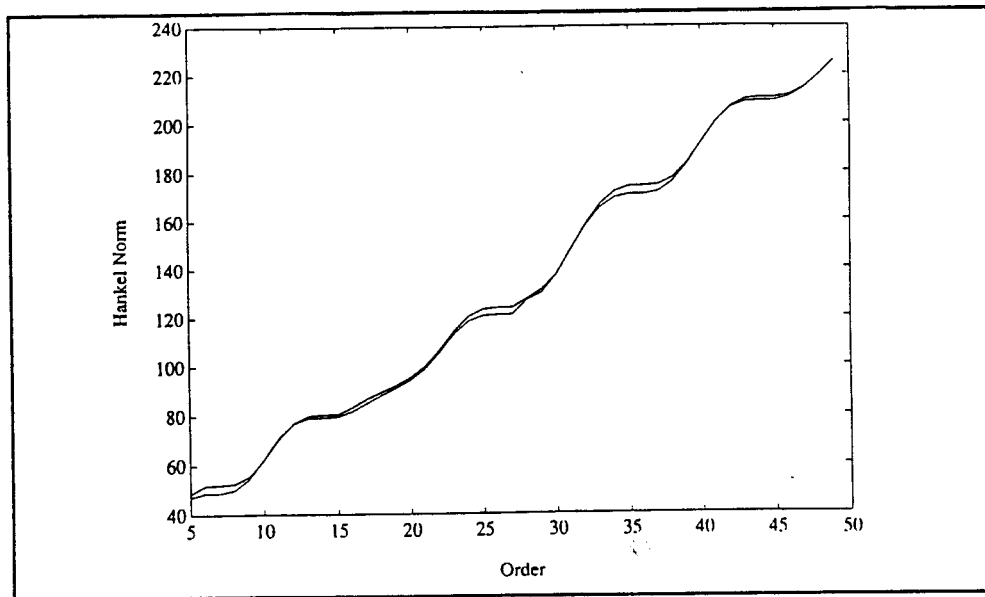


Figure 5.22: Hankel Norm Truncated MME Hankel Operator Day91008

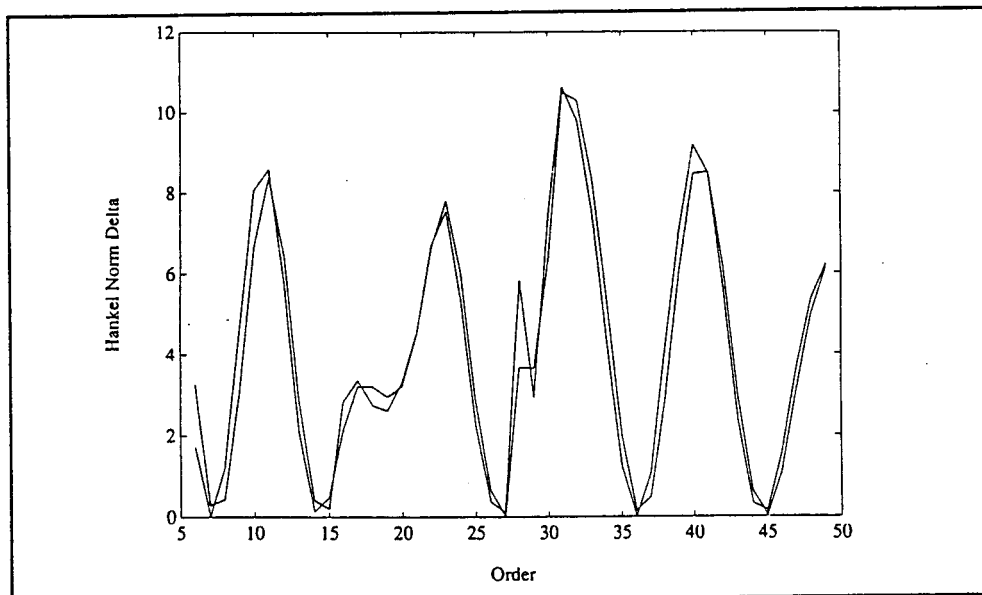


Figure 5.23: Upper Bound of Cauchy Sequence for Hankel Norm of Truncated MME Hankel Operator Day91008

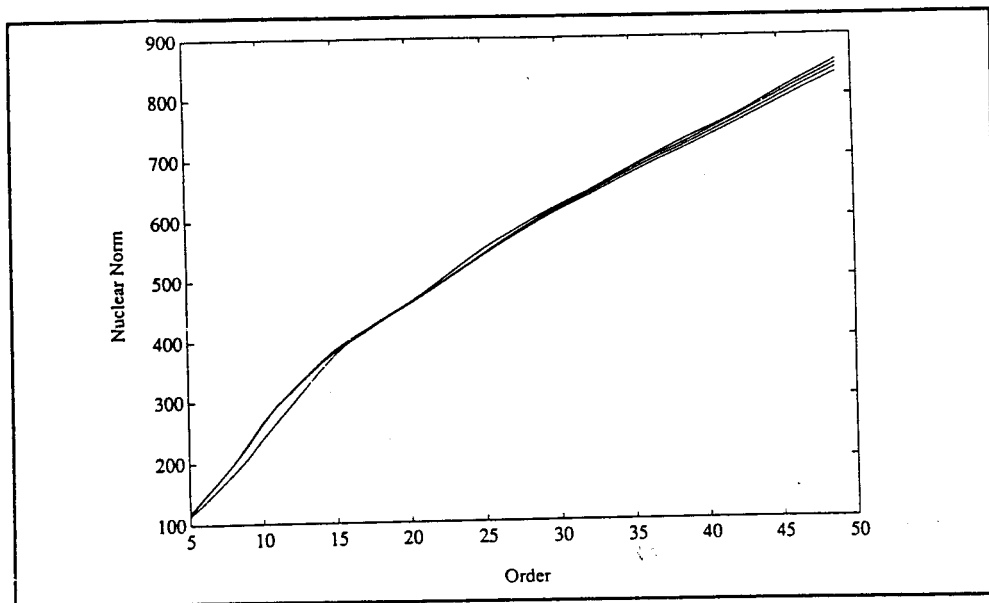


Figure 5.24: Nuclear Norm Truncated MME Hankel Operator Day91010

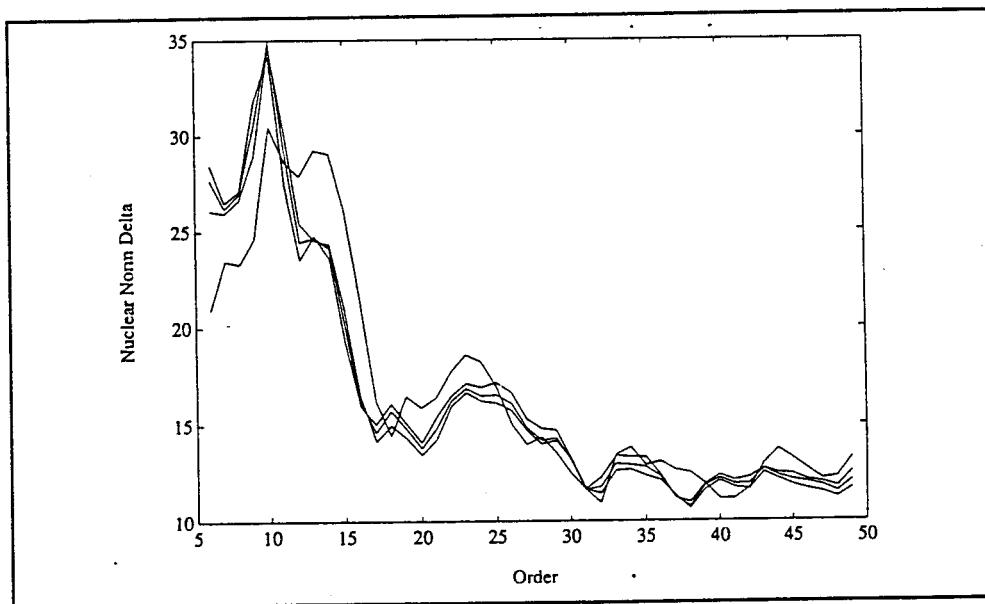


Figure 5.25: Cauchy Sequence of Nuclear Norms for Truncated MME Hankel Operator Day91010

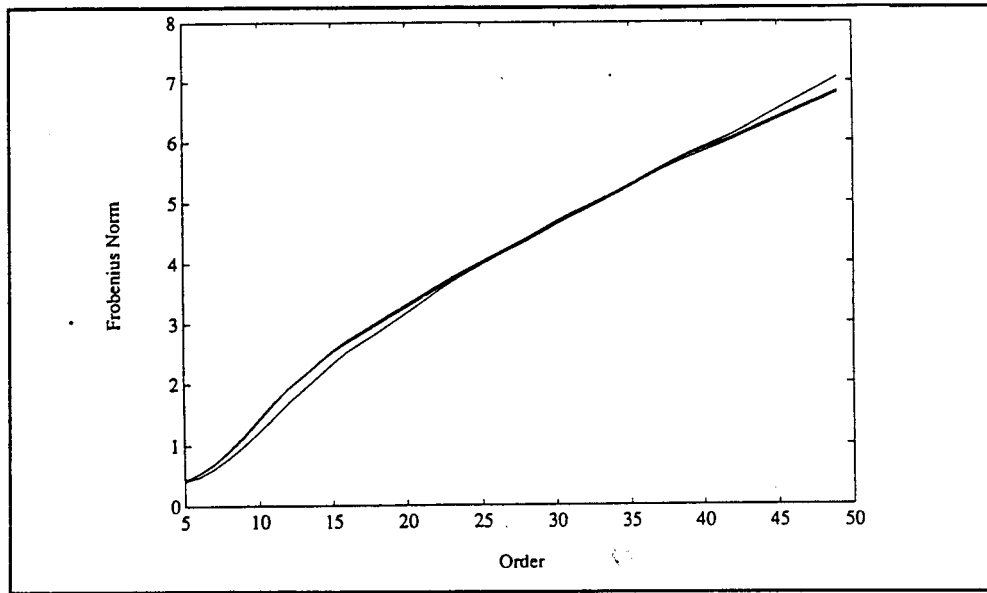


Figure 5.26: Frobenius Norm Truncated MME Hankel Operator Day91010

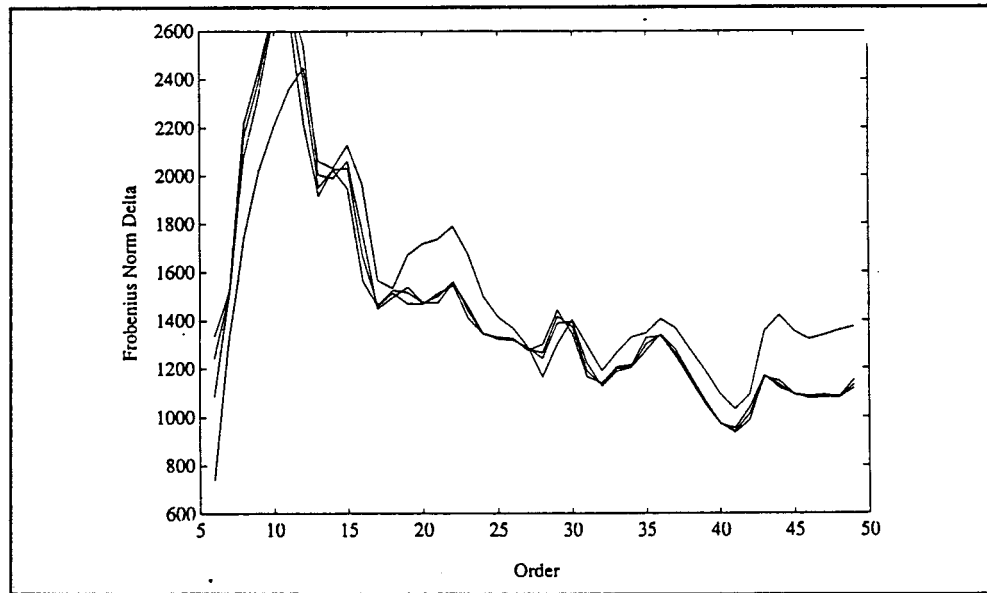


Figure 5.27: Upper Bound of Cauchy Sequence for Frobenius Norm of Truncated MME Hankel Operator Day91010

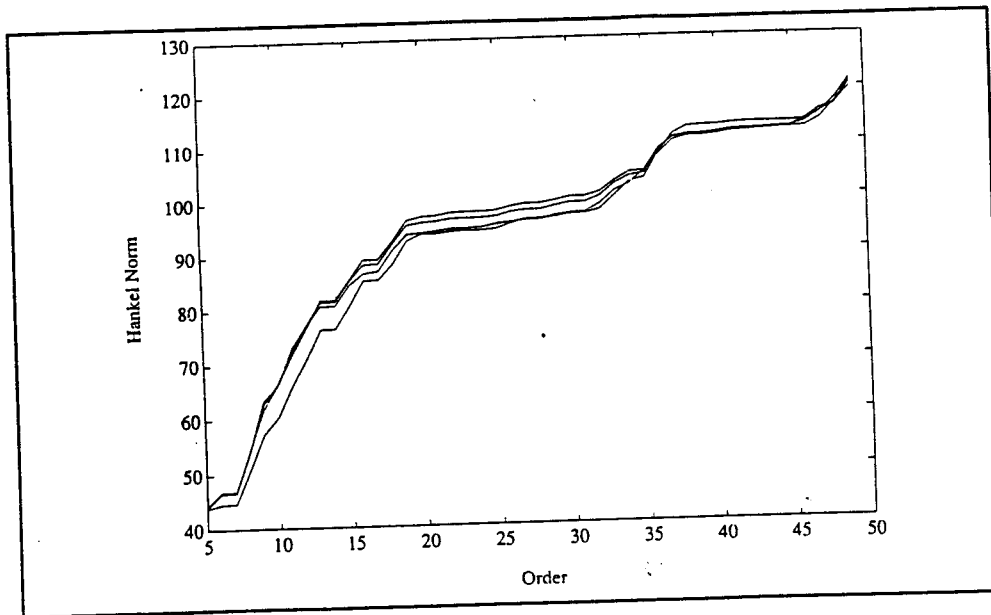


Figure 5.28: Hankel Norm Truncated MME Hankel Operator Day91010

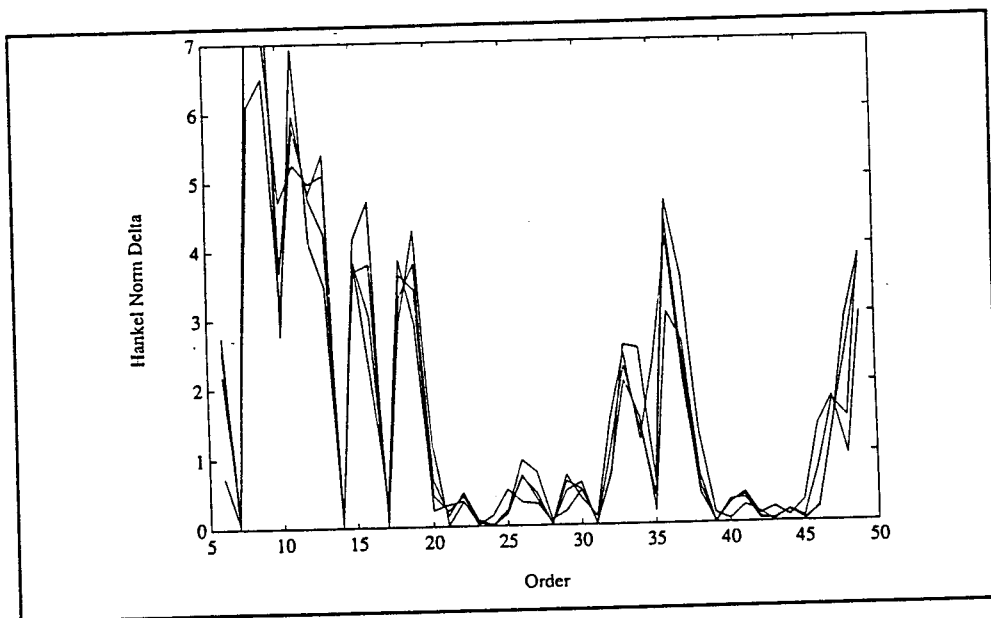


Figure 5.29: Upper Bound of Cauchy Sequence for Hankel Norm of Truncated MME Hankel Operator Day91010

5.4 Conclusions

Considering the brevity of the observation windows, the experiment was extremely successful. The experiment accomplished the following goals:

1. Structural modes were verified independently using the actual spacecraft in its true environment. Three of the first four modes were detected. These results are impressive compared to previous experiments, specifically, the 1985 Solar Array Flight Experiment (SAFE). The SAFE experiment, which was a two day experiment done on board the space shuttle, tested the modal properties of a deployed truss with an attached solar panel. The SAFE experiment only detected three modes. Comparing the overall experimental cost, this experiment done on the LACE spacecraft was an exceptional success.
2. Algorithmic approaches were tested with an actual experiment. Algorithms provided robust identification. The identified modes were tightly grouped and agreed with predicted modes. A variety of identification techniques were compared on simulated data. The Hankel operator technique performed better than any other approach, given the type of signal and the short length of observation.
3. A new laser application was verified. This experiment showed that laser tracking could be accomplished and provide data on which analysis could

be performed. This approach offers alternative experimental approaches to structural identification for low orbit satellites.

4. A system engineering approach was applied to a complex problem, whose technological solution spanned many disciplines. A requirement analysis review showed the need for large space systems. Given this requirement, the structural identification is a necessary component of on-station health monitoring and real time control algorithms.

This last point is very important. The problem of spacecraft dynamics is generated by increased demands from power considerations and the increased size of space structures. This experiment was designed to show that low cost low-complexity on-board hardware combined with algorithm analysis can satisfy the identification process and aid in the progression toward real-time identification and control.

BIBLIOGRAPHY

- [1] T. Soderstrom and P. Stoica. *Instrumental Variable Methods for System Identification*. Springer-Verlag, New York, N.Y., 1985.
- [2] B. L. Ho, R. E. Kalman. Effective Construction of Linear State-Variable Models from Input/ Output Data. *Proceedings of the 3rd Annual Allerton Conference on Circuit and System Theory*, pages 449–459, 1966.
- [3] Ruth Curtain. Sufficient Conditions for Infinite-Rank Hankel Operators to be Nuclear. *IMA Journal of Mathematical Control and Information*, 26:171–182, 1985.
- [4] D. J. Mook, J. L. Junkins. Minimum Model Error Estimation for Poorly Modeled Dynamic Systems. *AIAA Journal of Guidance, Control, and Dynamics*, 11(4):365–375, May-June 1988.
- [5] D. J. Mook, J. S. Lew. A Combined ERA/MME Algorithm for Robust System Realization/Identification. *Proceedings of the 29th Structures, Structural Dynamics and Materials Conference, Williamsburg, Virginia*, April 1988.

- [6] D. J. Mook, J. S. Lew. Multiple Shooting Algorithms For Jump-Discontinuous Problems in Optimal Control and Estimation. *To be Published*, 1991.
- [7] S. A. de Vries. Frequency domain analysis of models of flexible beams. Master's thesis, University of Groninge, 1988.
- [8] D. Enns. *Model reduction for Control System Design*. PhD thesis, Stanford University, 1984.
- [9] Bruce Francis. *A Course in H infinity Control Theory*. Springer-Verlag, New York, N.Y., 1987.
- [10] G. L. Blankenship. *Applications of Homogenization Theory to the Control of Flexible Structures*. Springer-Verlag, New York, NY, 1988.
- [11] Glover, K. All-optimal Hankel-norm approximations of Linear multivariable systems and their L_∞ error bounds. *International Journal of Control*, 39:1115–1193, 1984.
- [12] H. P. Geering. Continuous- Time Control Theory for Cost Functionals Including Discrete State Penalty Terms. *IEEE Transactions on Automatic Control*, 21:866–869, July 1976.
- [13] J. N. Juang, R. S. Pappa. An Eigensystem Realization Algorithm (ERA) for Modal Parameter Identification and Model Reduction. *AIAA Journal of Guidance, Control, and Dynamics*, 8(5):620–627, Sept.-Oct. 1985.

- [14] K. Glover, R. Curtain, and J. Partington. Realisation and Approximation of Linear Infinite-Dimensional systems with Error Bounds. *SIAM Journal of Control and Optimization*, 26(4):863–898, July 1988.
- [15] K. I. Schultz. Analysis of narrowband IR LACE measurements acquired during GMT days 195 and 200. MIT Lincoln Laboratory Memo, August 1990.
- [16] Thomas Kailath. *Linear Systems*. Prentice-Hall, Englewood Cliffs, N.J., 1981.
- [17] D. E. Kirk. *Optimal Control Theory*. Prentice-Hall, Englewood Cliffs, N.J., 1970.
- [18] L. W. Taylor. PDEMOD- Computer Software for Partial Differential Equation Modeling of Flexible Spacecraft. 2nd USAF/NASA Workshop: System Identification and Health Monitoring of Precision Space Structures, March 1990.
- [19] Lennart Ljung. Convergence analysis of parametric identification methods. *IEEE Transactions of Automatic Control*, 23:770–783, 1978.
- [20] Lennart Ljung. *System Identification: Theory for the User*. Prentice-Hall, Englewood Cliffs, N.J., 1988.

- [21] M. G. Safonov, R. Y. Chiang. A Schur Method for Balanced-Truncation Model Reduction. *IEEE Transactions of Automatic Control*, 34(7):729–733, July 1989.
- [22] M. G. Safonov, R. Y. Chiang, D. J. N. Limebeer. Hankel Model Reduction without Balancing - A Descriptor Approach. *Proceedings of the 28th Conference on Decision and Control*, pages 112–117, December 1987.
- [23] M. R. Osborne. On Shooting Methods for Boundary Value Problems. *Journal of Mathematical Analysis and Applications*, 27:417–433, 1969.
- [24] J. M. Maciejowski. *Multivariable Feedback Design*. Addison-Wesley, Reading, MA., 1989.
- [25] Moore, B. C. Principal Component Analysis in Linear Systems: Controllability, Observability, and Model Reduction. *IEEE Transactions on Automatic Control*, 26(1):17–32, Feb. 1981.
- [26] J. Weidmann. *Linear Operators in Hilbert Space*. Springer Verlag, Berlin, 1980.